Summer 2018

Theoretical studies of photoinduced dynamics and topological states in materials with strong electron-lattice couplings

Linghua Zhu
New Jersey Institute of Technology

Recommended Citation

Zhu, Linghua, "Theoretical studies of photoinduced dynamics and topological states in materials with strong electron-lattice couplings" (2018). *Dissertations*. 1386.
https://digitalcommons.njit.edu/dissertations/1386

ABSTRACT

THEORETICAL STUDIES OF PHOTOINDUCED DYNAMICS AND TOPOLOGICAL STATES IN MATERIALS WITH STRONG ELECTRON-LATTICE COUPLINGS

by
Linghua Zhu

First, we study the nonequilibrium dynamics of photoinduced phase transitions in charge ordered (CO) systems with a strong electron-lattice interaction and analyze the interplay between electrons, periodic lattice distortions, and a phonon thermal reservoir. Simulations based on a tight-binding Hamiltonian and Boltzmann equations reveal partially decoupled oscillations of the electronic order parameter and the periodic lattice distortion during CO melting, which becomes more energy efficient with lower photon energy. The cooling rate of the electron system correlates with the CO gap dynamics, responsible for an order of magnitude decrease of the cooling rate upon the gap reopening. The work also find that the time-dependent frequency of coherent oscillation reflects the dynamics of the energy landscape, such as transition between single-well and double-well, which sensitively depends on the photon energy and the pump fluence. The results demonstrate the intricate nonequilibrium dynamics in CO materials.

Second, a model for two-dimensional electronic, photonic, and mechanical metamaterial systems is presented, which has flat one-dimensional zero-mode energy bands and stable localized states of a topological origin confined within twin boundaries, antiphase boundaries, and at open edges. Topological origins of these flat bands are analyzed for an electronic system as a specific example, using a two-dimensional extension of the Su-Schrieffer-Heeger Hamiltonian with alternating shift of the chains. It is demonstrated that the slow group velocities of the localized flat band states are sensitively controlled by the distance between the boundaries and

the propagation can be guided through designed paths of these boundaries. We also discuss how to realize this model in metamaterials.

Third, the study of topological mechanical metamaterials system made of 1D or 2D arrays of spinners, as an experimental realization of electron models in the second part. Compared with experimental data for 1D case and makes prediction for 2D case of ribbon with open edges. And also show how they slow group velocity of localized edge modes depend on the width of the ribbon.

THEORETICAL STUDIES OF PHOTOINDUCED DYNAMICS AND TOPOLOGICAL STATES IN MATERIALS WITH STRONG ELECTRON-LATTICE COUPLINGS

by
Linghua Zhu

A Dissertation
Submitted to the Faculty of
New Jersey Institute of Technology and Rutgers University, Newark, NJ
in Partial Fulfillment of the Requirements for the Degree of
Doctor of Philosophy in Applied Physics

Department of Physics

August 2018

APPROVAL PAGE

THEORETICAL STUDIES OF PHOTOINDUCED DYNAMICS AND TOPOLOGICAL STATES IN MATERIALS WITH STRONG ELECTRON-LATTICE COUPLINGS

Linghua Zhu

Dr. Keun Hyuk Ahn, Dissertation Advisor — Date
Associate Professor of Physics, NJIT

Dr. Trevor A. Tyson, Committee Member — Date
Distinguished Professor of Physics, NJIT

Dr. Andrei Sirenko, Committee Member — Date
Professor of Physics, NJIT

Dr. Daniel Murnick, Committee Member — Date
Professor of Physics, Rutgers-Newark

Dr. Dong Kyun Ko, Committee Member — Date
Assistant Professor of Electrical and Computer Engineering, NJIT

BIOGRAPHICAL SKETCH

Author:	Linghua Zhu
Degree:	Doctor of Philosophy
Date:	August 2018

Undergraduate and Graduate Education:

- Doctor of Philosophy in Physics,
  New Jersey Institute of Technology, Newark, NJ, 2018
- Bachelor of Science in Physics,
  University of Science and Technology of China, Hefei, China, 2012

Major:	Applied Physics

Presentations and Publications:

Linghua Zhu, Tsezar F. Seman, Michel van Veenendaal and Keun Hyuk Ahn, "Photoinduced nonequilibrium dynamics in charge ordered materials," *Journal of Applied Physics, 123, 115112, 2018. doi: 10.1063/1.5018045*

Linghua Zhu, Emil Prodan and Keun Hyuk Ahn, "Flat Energy Bands within Antiphase and Twin Boundaries and at Open Edges in Topological Materials," *arXiv:1807.10778 (Submitted)*

Linghua Zhu, "Electronic Properties of Structural Twin and Anti-phase Boundaries in Model Topological Insulator," *Oral presentation*, American Physical Society March Meeting, Los Angeles, California, 2018.

Linghua Zhu, "Simulations of Photo-induced Non-Equilibrium Dynamics in Charge Ordered Materials," *Oral presentation*, Mid Atlantic American Physical Society Meeting, Newark, New Jersey, 2017.

Linghua Zhu, "Simulations of Photo-induced Non-Equilibrium Dynamics in Charge Density Wave Materials," *Oral presentation*, American Physical Society March Meeting, New Orleans, Lousiana, 2017.

Linghua Zhu, "Research Using IST ARCS-Managed High Performance Computing, Big Data, and Database Resources," *Oral presentation*, Second Annual Researchers Symposium, NJIT, Newark, New Jersey, 2017.

Linghua Zhu, *Poster presentation*, Dana Knox Student Research Showcase (NJIT), Newark, New Jersey, 2017.

Linghua Zhu, *Poster presentation*, Dana Knox Student Research Showcase (NJIT), Newark, New Jersey, 2016.

Information is physical, information is profitable.

ACKNOWLEDGMENT

First and foremost I would like to express my special appreciation and thanks to my advisor, Professor Ken Ahn. It has been an honor to be his Ph.D student. Dr. Ken Ahn has very wide knowledge and accurate physical intuition. He has been supportive since the first days I began working on the computational condensed matter physics. He had often pointed out the incompleteness of my works and helped me to improve my understandings on each problem. He has taught me, how good computational physics is done. I appreciate all his contributions of time, ideas, and funding for my Ph.D study. I would like to thank him for the continuous support of my Ph.D research, for his patience, motivation, and immense knowledge. His guidance helped me in all the time of research and writing of this thesis. I could not have imagined having a better advisor and mentor for my Ph.D study. Not only the academic research, I also learned the rigorous research attitude from him. I am thankful for the excellent example he has provided as a successful physicist and professor. Initially, I joined Professor Ahn's group wishing to learn how to do the research, but finally earned much more than that. Not only knowledge and advice, but also life-long attitude to work, life-changing experience, and precious study memory.

Besides my advisor, I would like to thank the rest of my dissertation committee: Professors Dr. Trevor A. Tyson, Dr. Andrei Sirenko, Dr. Dong Kyun Ko and Dr. Daniel Murnick, for their insightful comments and encouragement, and also for the hard questions which challenged me to widen my research from various perspectives.

My sincere thanks also goes to my collaborators Dr. Michel van Veenendaal, Dr. Tsezar F. Seman, and Dr. Emil Prodan, who provided me the opportunities to do the collaboration work. Without their precious support and work it would have not been possible to conduct this research. Specially, I cannot forget the great help from Dr. Tsezar F. Seman, who helped me to improve my skills on coding.

My time at NJIT was made enjoyable in large part due to the many friends, Zhaoqian Su, Farbod Mahmoudinobar and groups that became a part of my life. I am grateful for time spent with my classmates and friends. Thanks for your worm support and good wishes during my research work.

Last, but not the least, I would like to thank my family for all their love and encouragement. For my father Shuan Zhu, mother Sumei Yan raised me with a love of science and supported me in all my pursuits. And most of all for my loving, supportive, encouraging, and patient boyfriend Mu Lin whose faithful support during the final stages of my Ph.D. is so appreciated. Thank you.

TABLE OF CONTENTS

Chapter **Page**

1 INTRODUCTION 1

2 PHOTOINDUCED NONEQUILIBRIUM DYNAMICS IN CHARGE ORDERED MATERIALS 10

  2.1 Introduction 10

  2.2 Review of Complex Oxides with Charge and Orbital Order 11

  2.3 Review of Pump-probe Experiment on Complex Oxides 12

  2.4 Model 13

    2.4.1 Hamiltonian 13

    2.4.2 Lattice Dynamics 17

    2.4.3 Electron Dynamics 18

    2.4.4 Approximations Used 19

  2.5 Results 20

    2.5.1 Equilibrium States and Excitations by Optical Pump 20

    2.5.2 Nonequilibrium Dynamics Induced by Photons with $E_{\text{photon}} \gg \Delta_{\text{gap}}$ 22

    2.5.3 Nonequilibrium Dynamics Induced by Photons with $E_{\text{photon}} = \Delta_{\text{gap}}$ 29

    2.5.4 Dynamics of Energy Landscape and Coherent Oscillation Frequency 31

    2.5.5 Nonthermal Electron Distribution and Electron Energy Relaxation 38

  2.6 Comparison with Experiments 40

  2.7 Summary 41

  2.8 Supplementary Material 43

3 ELECTRONIC PROPERTIES OF STRUCTURAL TEXTURES IN MODEL TOPOLOGICAL INSULATOR WITH TOPOLOGY-STRUCTURE COUPLING 44

  3.1 Introduction 44

  3.2 Model 45

    3.2.1 Model 2D structure 45

TABLE OF CONTENTS
(Continued)

Chapter **Page**

- 3.2.2 Electron Hamiltonian, Chirality, and Band Structure for Uniform States 46
- 3.2.3 Winding Number ν and Topology 49
- 3.2.4 Lattice Energy for Relaxed Structural Textures 50
- 3.3 Results 51
  - 3.3.1 Antiphase boundaries along 135° 52
  - 3.3.2 Antiphase Boundaries Along 90° and 0° 52
  - 3.3.3 Twin Boundaried Along 135° 57
  - 3.3.4 Texture of Mixed Twin and Antiphase Boundaries 60
- 3.4 Summary 65

4 FLAT FREQUENCY BANDS AT OPEN EDGES OF TWO DIMENSIONAL SPINNER SYSTEMS 66
- 4.1 2D Spinner system and effective Hamiltonian 66
- 4.2 1D SSH Spinner System with Open Edges 70
- 4.3 Experimental Model 2D Ribbon Spinner System with 135° Open Edge 80

5 SUMMARY 87

6 CODE DEVELOPED FOR NUMERICAL CALCULATIONS 90
- 6.1 C++ Code for the Simulations of Photoinduced Nonequilibrium Dynamics in Charge Order Materials 90
- 6.2 Fortran Code for Calculation of Electronic States in Model Topological Insulators 107
- 6.3 Fortran Code for Calculation of Flat Frequency Bands at Open Edges of 2D Spinner Systems 112

BIBLIOGRAPHY 120

LIST OF TABLES

Table **Page**

3.1 Winding Number ν for Figure. 3.2 49

3.2 Winding Number ν that Applied to 90° Boundaries in Figure. 3.7 56

3.3 Winding Number ν for Figure. 3.8 57

4.1 Winding Number $\nu(135^\circ)$ and $\nu(0^\circ)$ Depend on β_g, β_y, β_r, β_b. 70

4.2 Winding Number $\nu(135^\circ)$ and $\nu(0^\circ)$ Depend on β_g, β_y, β_r, β_b. 71

4.3 Frequency (Hz) for 1D Spinner System with Eight Unit Cells 75

LIST OF FIGURES

Figure **Page**

1.1 $\mathrm{MnO_2}$ layer in $\mathrm{Pr_{0.5}Ca_{0.5}MnO_3}$. Adapted and modified from Ref. [12]. . 2

1.2 Schematic drawings showing CDW due to the Peierls instability. [63] Dashed line, represents the uniform charge density for equally spaced 1D chain shown in open circles. Solid line represents CDW as a result of distorted 1D chain shown in solid circles. Adapted and modified from Ref. [63]. 2

1.3 Crystal structure of the 1T and the 2H layered transition-metal dichalcogenides. Adapted and modified from Ref. [63]. 3

1.4 CDW transition in $1T - TaS_2$, $2H - TaSe_2$, and $1T - TiSe_2$. Adapted and modified from Ref. [63]. 3

1.5 Representative results of temperature dependence of resistivity ρ in zero field (solid line) and 5 T (dashed line). T_{CO} represents the CO transition temperature. Adapted and modified from Ref. [44]. 4

1.6 Example of superlattice peaks in (b) and (d) signal CO phase. Electron diffraction patterns showing CO transition for $Nd_{0.65}Ca_{0.35}MnO_3$ taken at 250 K (a), (c) and 170 K (b), (d). Adapted and modified from Ref. [44]. 5

1.7 Measured evolution of the normalized X-ray intensity for three super lattice reflections. Adapted and modified from Ref. [12]. 6

1.8 Example of mechanical metamaterials, made of array of spinners [9, 58]. Adapted and modified from Ref. [58]. 7

1.9 Example of sonic metamaterials. Sound waves propagate between triangular rods. Adapted and modified from Ref. [46] 8

1.10 Example of ultracold fermions. Ultracold fermion gas used to periodically modulated the optical lattice. Adapted and modified from Ref. [34] . 8

2.1 The model system of an MO_2 square lattice with periodic boundary conditions. The size of the solid circles schematically represents the variation of electron density on M ions in CO state. Arrows show the displacements of the O ions, represented by u. Adapted from Ref. [77]. 14

2.2 (a) Example of DOS per site for electrons D_e versus energy ε. The band gap is 58.9 meV. (b) DOS per site for phonons D_p versus phonon energy ω. Adapted from Ref. [77]. 16

LIST OF FIGURES
(Continued)

Figure **Page**

2.3 (Color online) The red line shows the equilibrium distortion u_{eq} of the B ions versus temperature T. The critical temperature is about $T_{\mathrm{c}} \approx$ 217 K. The blue dots represent the renormalized frequency Ω_{ren} for the oscillation of u at $T > T_c$. The blue line represents the fit to the mean field theory predictions near T_c. 21

2.4 Examples for the evolution of the distribution function f versus energy ε for $E_{\mathrm{photon}} \gg \Delta_{\mathrm{gap}}$. (a) The red line shows the distribution function right after the optical pump, $t = 0$; the solid orange line represents the distribution function at $t = 0.15$ ps. The Fermi-Dirac distribution at the corresponding effective temperature $T_{\mathrm{eff}} = 904$ K, defined by Eq. (2.18), at $t = 0.15$ ps is shown in a dashed orange line. (b) The solid blue line represents the electron distribution at $t = 18$ ps during the gap reopening. The Fermi-Dirac distribution with the corresponding effective temperature $T_{\mathrm{eff}} = 177$ K at $t = 18$ ps is shown in a dashed blue line. Adapted from Ref. [77]. 24

2.5 Nonequilibrium dynamics for $E_{\mathrm{photon}} \gg \Delta_{\mathrm{gap}}$ and $F = 4.38$ meV/site $>$ F_c, the critical fluence for photoinduced insulator-metal transition. The time scales up to 2 ps and between 2 ps and 50 ps are chosen differently to reveal features more clearly. (a) $T_{\mathrm{eff}} - T_i$, the difference between the effective temperature of the electron system defined by Eq. (2.18) and the initial temperature before the pump, (b) the square of periodic lattice distortion $\bar{u}^2$, the square of electronic order parameter $\delta\bar{n}^2$, and the square of equilibrium distortion $\bar{u}^2_{\mathrm{eq}}$ at $T_{\mathrm{eff}}(t)$, normalized to their values before the optical pump, (c) $\bar{d} = \bar{u}^2 - \delta\bar{n}^2$, which parameterizes the decoupling between the CO and the periodic lattice distortion, (d) Δf, the average deviation of the electron distribution function $f(\varepsilon)$ from the Fermi-Dirac distribution function $f_{\mathrm{FD}}(\varepsilon, T_{\mathrm{eff}})$, defined by Eq. (2.22), (e) $\Delta N_{\mathrm{upper}}$ defined by Eqs. (2.23) and (2.24), that is, the number of excess electrons per site in the upper band with respect to the equilibrium state before the optical pump. The horizontal arrow indicates the number of electrons excited by the optical pump. For clarity, $\bar{d}$ and Δf between 2 ps and 50 ps are multiplied by constant factors indicated in the figure. Adapted from Ref. [77]. 25

LIST OF FIGURES
(Continued)

Figure **Page**

2.6 Comparison between the energies required for the thermodynamic and photoinduced insulator-metal transitions. The purple [orange] line represents the thermodynamic melting energy $\Delta E_{\text{tot}}(T_i)$ $[\Delta E_{\text{e}+u}(T_i)]$ with [without] incoherent phonons, that is, the energy needed to thermodynamically heat the system including [excluding] incoherent phonons from T_i to T_c. The blue and red dots in the main panel represent the critical fluence $F_c(T_i)$ for the photoinduced insulator-metal transition by the pump beams with $E_{\text{photon}} \gg \Delta_{\text{gap}}$ and $E_{\text{photon}} = \Delta_{\text{gap}}$, respectively. The inset shows F_c versus E_{photon} at a fixed initial temperature $T_i = 135$ K. Adapted from Ref. [77]. 30

2.7 Nonequilibrium dynamics for $E_{\text{photon}} = \Delta_{\text{gap}}$. (a) The difference between the effective electron temperature T_{eff} and the initial temperature T_i before the pump. (b) ΔN_{upper}, the number of excess electrons in the upper band with respect to the equilibrium state before the pump. (c), (d), and (e): Normalized squares of the periodic lattice distortion and electronic order parameter, $\bar{u}^2$ and $\delta\bar{n}^2$, defined in Eq. (2.19) versus time t. The fluence of the pump beams are (c) $F = 0.97$ meV/site, (d) 1.83 meV/site, and (e) 5.65 meV/site, all above the critical fluence $F_c = 0.91$ meV/site. For (e), we use $W = 0.06$ eV as the width of the Gaussian peak in Eq. (2.17). Adapted from Ref. [77]. 32

2.8 Energy landscape dynamics initiated by the optical pump with $E_{\text{photon}} = 2$ eV $\gg \Delta_{\text{gap}}$ and $F = 4.38$ meV/site for (a) and (c), and with $E_{\text{photon}} = \Delta_{\text{gap}}$ and $F = 0.97$ meV/site for (b) and (d). In (a) and (b), the dotted black lines represent the harmonic energy near the equilibrium distortion before the optical pump. In (c) and (d), the orange and green lines represent $u(t)$ and equal-energy lines respectively, with the axis ranges of -5 ps $< t < 25$ ps and -0.06 Å $< u < 0.06$ Å. Adapted from Ref. [77]. 34

2.9 (Color online) Energy landscape dynamics initiated by the optical pump with $E_{\text{photon}} = \Delta_{\text{gap}}$ for (a) the fluence $F = 0.96$ meV/site, above F_{c}, and for (b) $F = 0.32$ meV/site, below F_{c}. Corresponding plots in U-u-t space are shown in (c) and (d). See the caption for Figure 2.8. Adapted and modified from Ref. [77] 36

LIST OF FIGURES
(Continued)

Figure **Page**

2.10 (a) Angular frequency of coherent oscillation Ω versus time t, (b) the first angular frequency Ω_{1st} from the first half-oscillation versus the fluence of the optical pump F for $E_{\mathrm{photon}} = \Delta_{\mathrm{gap}}$ and $E_{\mathrm{photon}} = 2$ eV $\gg \Delta_{\mathrm{gap}}$. Lines connecting symbols are guides for eyes. The horizontal dashed black lines represents the bare angular frequency $\Omega_{\mathrm{bare}} = \sqrt{K/m}$ without electron-lattice coupling and the equilibrium angular frequency Ω_{eq} before the optical pump. The vertical dashed red and blue lines in (b) indicate the critical fluence F_c for $E_{\mathrm{photon}} = \Delta_{\mathrm{gap}}$ and 2 eV, respectively. Adapted from Ref. [77]. 37

2.11 (a) Schematic diagram showing electron transfer from the lower to the upper band through two typical electron-electron scattering processes (blue and green arrows) right after the optical pump with $E_{\mathrm{photon}} \gg \Delta_{\mathrm{gap}}$. The black and the red lines represent the actual electron distribution and the corresponding Fermi-Dirac distribution, respectively. (b) Schematic diagram showing the effects of the gap reopening on f_ε. The gray line shows the actual distribution one time step Δt earlier. The black and the red lines represent the actual and the Fermi-Dirac distributions. Adapted from Ref. [77]. 39

3.1 (a) 2D square lattice; (b) Vertical rectangle with x-distortion; (c) Horizontal rectangle with y-distortion. 45

3.2 The model system of an AB_2 square lattice with periodic boundary conditions. Arrows show the displacements, represented by d_x and d_y in different directions. $1+e$ and $1-e$ represent the distance between neighbor A and B sites, in vertical and horizontal direction, respectively. The displacement parameters, d_x and d_y represent the displacement of A ion in unit cell at $0 \cdot \vec{a}_1 + 0 \cdot \vec{a}_2$. 46

3.3 The phase diagram for the system.Red regions are the insulator phase, blue regions are the metal phase. dark green line is the semi-metal phase. 48

3.4 Atomic scale distortion modes for a square lattice. [7] Signs of d_x and d_y are the same with the signs of $\tilde{s}_x$ & $\tilde{s}_y$. Sign of e coincides with sign of e_3. 50

3.5 APB along 135°. Red line shows the APB, and blue circles show the unit cell. 53

3.6 Band structure for APB along 135° with the relaxed distortion. 54

3.7 When APB parallel y-axis, circle show the way how to choose unit cell. 55

LIST OF FIGURES
(Continued)

Figure **Page**

3.8 When APB parallel x-axis, circle show the way how to choose unit cell. 55

3.9 (a) Band structure for APB at 90° in Figure 3.7; (b) Band structure for APB at 0° in Figure 3.8 56

3.10 TB along 135°, and beside the TB, $\tilde{s}_x$, $\tilde{s}_y$ have the same sign. 58

3.11 TB along 135°, and beside the TB, $\tilde{s}_x$, $\tilde{s}_y$ have the opposite sign. 59

3.12 (a) Band structure for TB along 135° which separates domains with $\tilde{s}_x$, $\tilde{s}_y$ of the same sign, (b) Band structure for TB along 135°, which separates domians with $\tilde{s}_x$, $\tilde{s}_y$ of opposite signs. 60

3.13 (a) Schematic drawing of structural texture with both APB and TB. Blue regions have $e_3 > 0$ and $\tilde{s}_x < 0$, red region have $e_3 < 0$ and $\tilde{s}_y < 0$, and green region have $e_3 > 0$ and $\tilde{s}_x > 0$. Thick black lines indicate the boundaries where zero-energy states are expected from topological analysis. (b) Local DOS at $E = 0$. 61

3.14 (color online) (a), (b), (c) Band structures for the lattices with APB shown in (d), (e) and (f), respectively. APB zero-mode bands are present in (a) and (b), but are absent in (c). Highly dispersive bands inside the gap in (c) are not of topological origin. (d), (e), (f) Lattices with APB in 135° direction for (d) and 0° direction for (e) and (f). In (f), the colors represent the integrated electron density for the states within $\varepsilon_m = \pm 0.1$. (g) Average group velocity c_g versus the number of bonds δ in the horizontal direction between 135° direction APB. Adapted from Ref. [76] 62

3.15 (color online) (a) Schematic sketch showing a pair of zig-zag APB with $e < 0$ and $d_y = 0$ for 64×64 atoms with periodic boundary conditions. From left to right, the phase of d_x changes from positive to negative back to positive for the three domains; (b) Actual distortion and integrated electron density of zero mode states for the lower half of (a); (c) Plot of energy for eigenstates, ε_m, versus the index m for the states in the order of increasing energy. Adapted from Ref. [76] 63

4.1 (a) The four-armed spinners; (b) A pattern made by the four-armed spinners; (c) Spinners interacting with green pairs; (d) Spinners interacting with blue pairs; (e) Spinners interacting with red pairs. Magnets' south and north poles are aligned, so that all nearest neighbor interactions are attractive. For example, A spinner's all four magnets have north poles pointing outward, whole B spinner's magnets have south poles pointing outward. 67

LIST OF FIGURES
(Continued)

Figure **Page**

4.2 A pattern made by the four-armed spinners, with magnets of four different strengths, represented by red, blue, green, and yellow colors. Similar with Figure 4.1, replace one of green magnets by yellow magnet. . . . 68

4.3 The 1D spinner system with the open edge. Grey line demonstrated unit cells. 72

4.4 The 1D spinner system with the two fixed side spinners. Grey line demonstrated unit cells. 72

4.5 The frequency for the spinner system with period boundary condition and with open edges. 74

4.6 The values of eigenvector component for the edge modes at each site. . 76

4.7 The absolute value of eigenvector component for the edge modes at each site. 77

4.8 Preliminary experimental data for the frequency for the spinner system with eight unit cells and open edges. This data has been obtained by Prof. Camelia Prodan, David Apigo, and Kai Qian at New Jersey Institute of Technology. 78

4.9 The experimental movement for edge mode of the spinner system with open edge. his data has been obtained by Prof. Camelia Prodan, David Apigo, and Kai Qian at New Jersey Institute of Technology. 79

4.10 Four-armed spinner ribbon system along 135° with the open edges. . . . 81

4.11 With different unit cells (4,8, and 12), the relation between f^2 and k_2/a. 82

4.12 With different unit cells (4,8, and 12), the relation between f and k_2/a. 83

4.13 Map of Integrated mode strengths for the edge bands for a spinner ribbon with 16 unit cell width. The red and blue colors represent A and B sites, respectively. 85

4.14 The group velocity of edge modes versus the width of the spinner ribbon. Results for 4, 8, 12, 16, and 20 unit cell wide ribbons are shown here. 86

CHAPTER 1

INTRODUCTION

Electron-lattice coupling is one of the most important topics in condensed matter physics. In this dissertation, we theoretically and computationally study two phenomena, in which the electron-lattice interaction plays an important role. After that, we study a related phenomenon in a mechanical system, in which variation in interaction between spinners results in structure-topology coupling.

First, we study the photoinduced nonequilibrium dynamics in charge ordered materials. Recently, photoinduced insulator-metal transitions in charge ordered (CO) or charge density wave (CDW) materials have attracted a lot of attention. [12] Strongly correlated electron systems often exhibit very strong interactions between structural and electronic degrees of freedom that lead to complex and interesting phase diagrams; for example, which involve transition between charge order (CO) phase and metallic phase [33]. Charge order means the periodic ordering of charge state of ions in solids, for example, in $\mathrm{Pr_{0.5}Ca_{0.5}MnO_3}$ as shown in Figure 1.1 [12] observed. A classic example of CDW is the Peierls instability, explained in Figure 1.2 [63]. More recent examples of CDW materials are layered transition-metal dichalcogenides shown in Figure 1.3 [63], in which CDW and associated increase of unit cells are shown in Figure 1.4 [63]. The CO or CDW transition usually involves order of magnitude increase of resistively, as shown in Figure 1.5 [44] for perovskite manganites. Powerful experimental probe for CDW and CO phases is the electron diffraction, in which the appearance of superlattice peak signals the CO and CDW transition, as shown in Figure 1.6 [44]. Recently, it is observed that ultra-short (order of femtosecond) optical pulse can induce a partial or complete melting of CO state as shown in Figure. 1.7 [42, 43, 53].

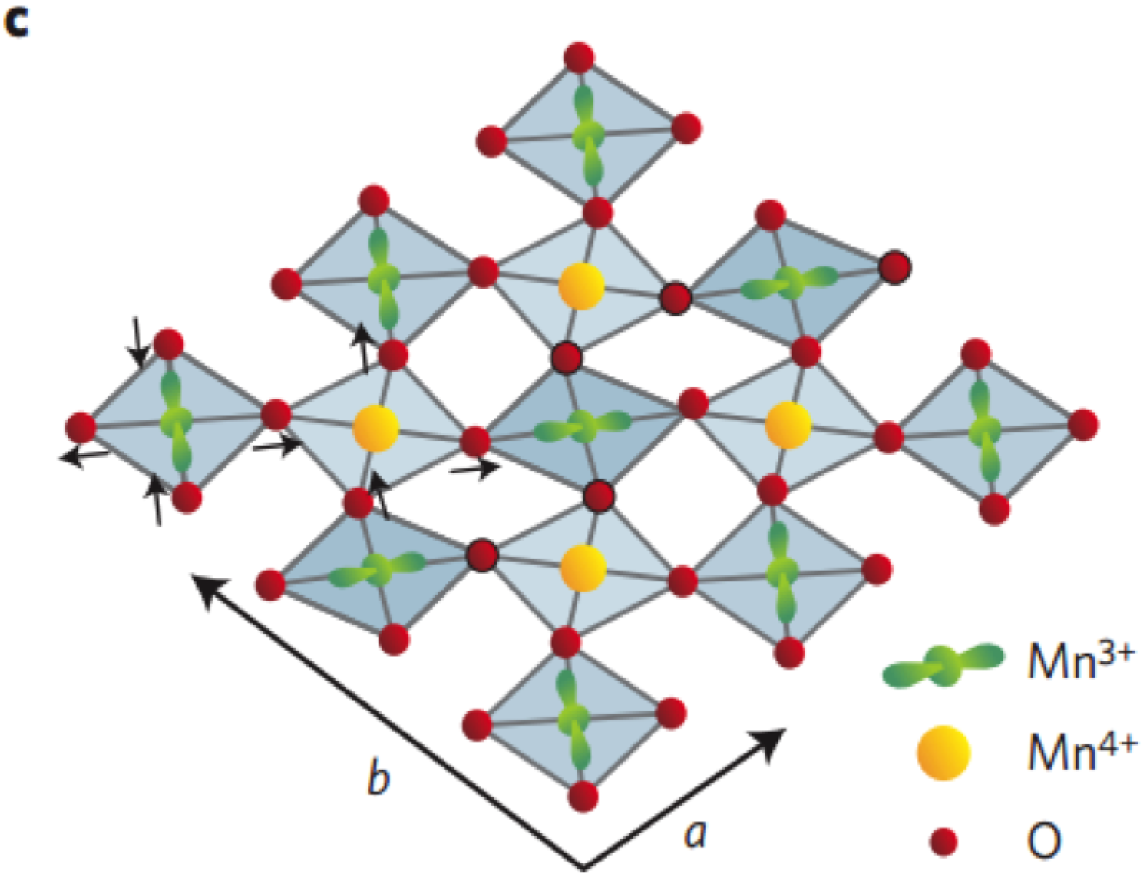

Figure 1.1 MnO_2 layer in $Pr_{0.5}Ca_{0.5}MnO_3$. Adapted and modified from Ref. [12].

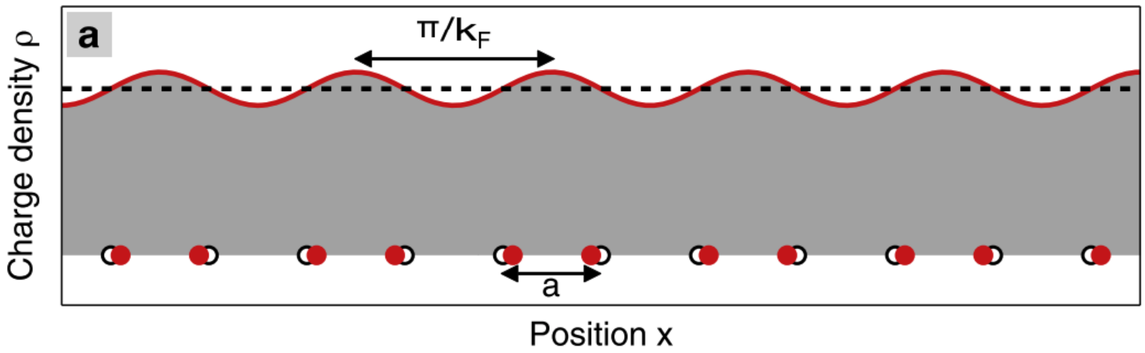

Figure 1.2 Schematic drawings showing CDW due to the Peierls instability. [63] Dashed line, represents the uniform charge density for equally spaced 1D chain shown in open circles. Solid line represents CDW as a result of distorted 1D chain shown in solid circles. Adapted and modified from Ref. [63].

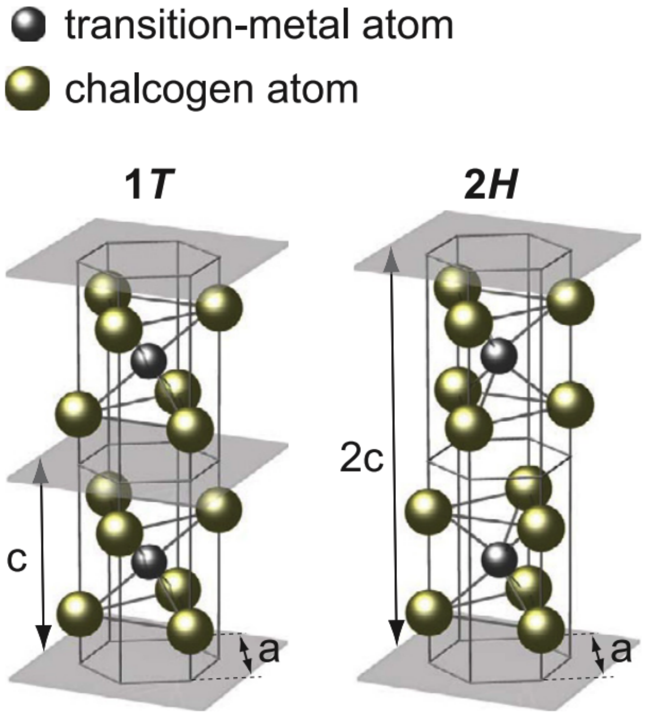

Figure 1.3 Crystal structure of the 1T and the 2H layered transition-metal dichalcogenides. Adapted and modified from Ref. [63].

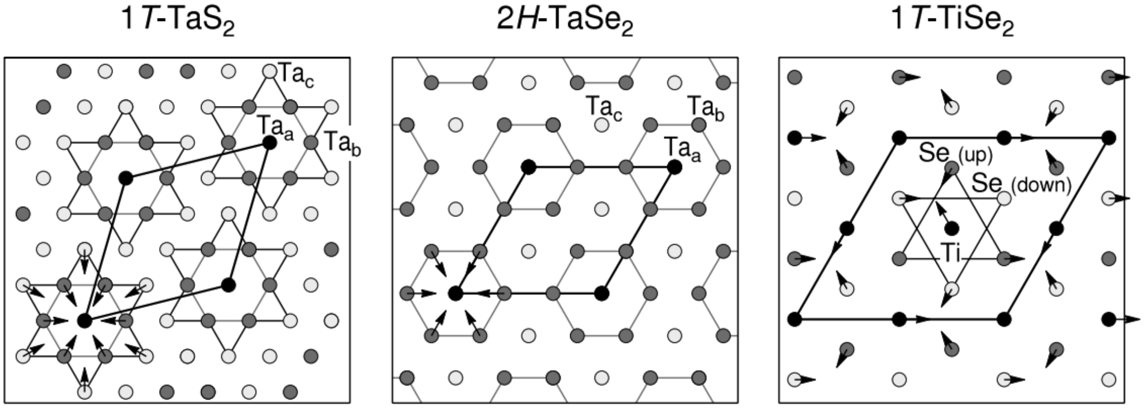

Figure 1.4 CDW transition in $1T-TaS_2$, $2H-TaSe_2$, and $1T-TiSe_2$. Adapted and modified from Ref. [63].

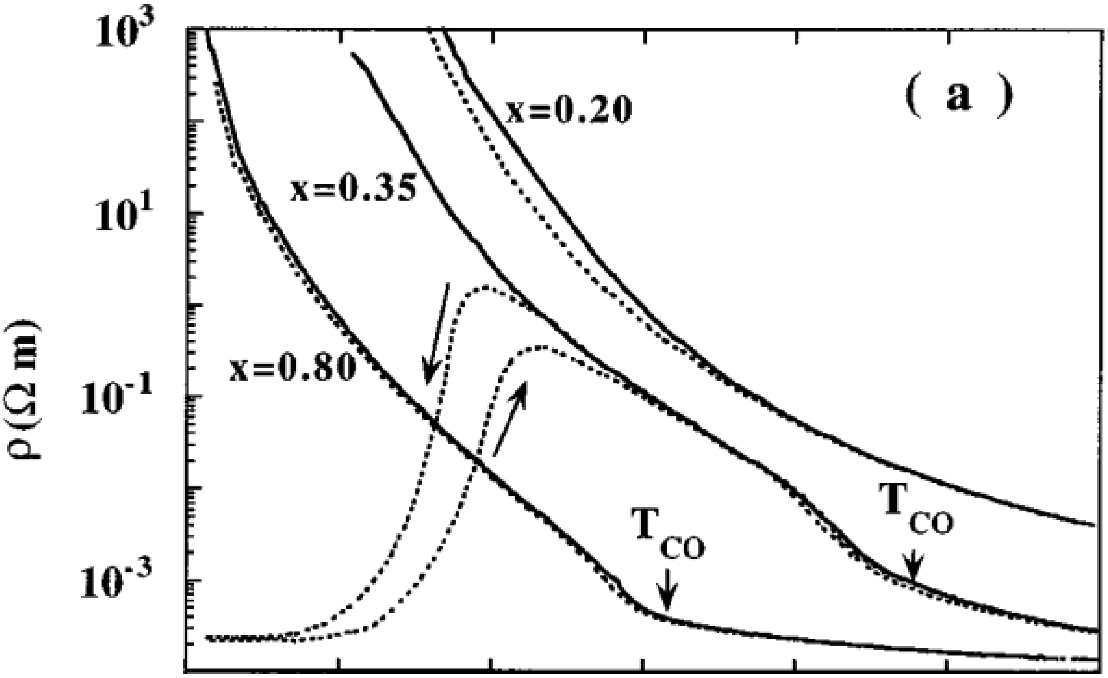

Figure 1.5 Representative results of temperature dependence of resistivity ρ in zero field (solid line) and 5 T (dashed line). T_{CO} represents the CO transition temperature. Adapted and modified from Ref. [44].

The goal of our theoretical study is to understand the interplay between electron and lattice during non-equilibrium photo-induced phase transitions of CDW materials through simulations for a simple model. It has been proposed that the dynamics of the phase transformation can be described using a single time-dependent order parameter that depends exclusively on the electronic excitation. However, atomic-scale, coupled dynamics of electrons and lattice has not been well understood [74]. We will particularly focus on such transitions in charge density materials or charge-orbital-ordered materials, because many experiments have been done on these materials lately. We will simulate the dynamics in time and compare with experimental observations, which will give us insights on how the electron-lattice interaction manifests itself in non-equilibrium situation.

Second, we studied the electronic properties of structural textures in model topological insulator with topology-lattice coupling. Topology has become a very

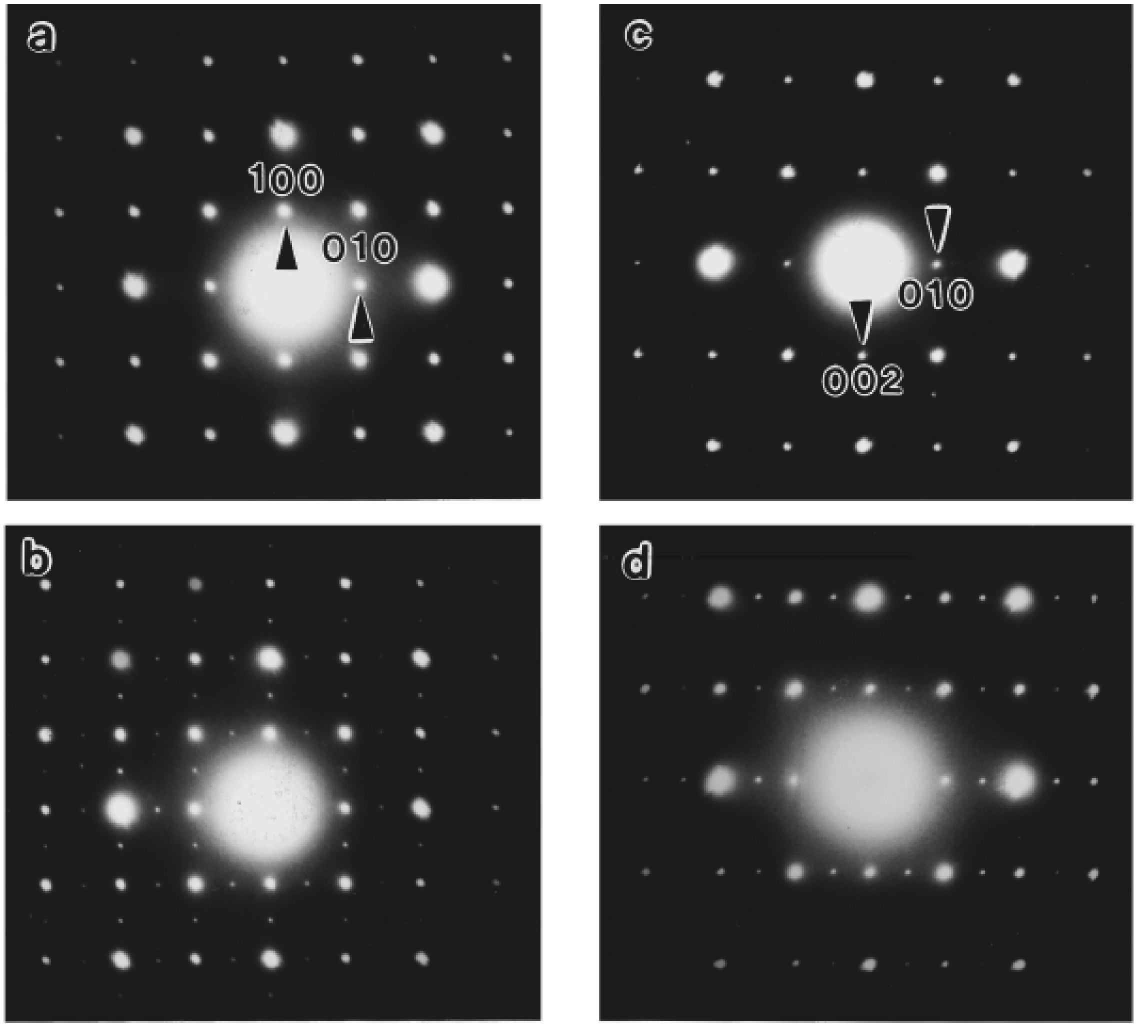

Figure 1.6 Example of superlattice peaks in (b) and (d) signal CO phase. Electron diffraction patterns showing CO transition for $Nd_{0.65}Ca_{0.35}MnO_3$ taken at 250 K (a), (c) and 170 K (b), (d). Adapted and modified from Ref. [44].

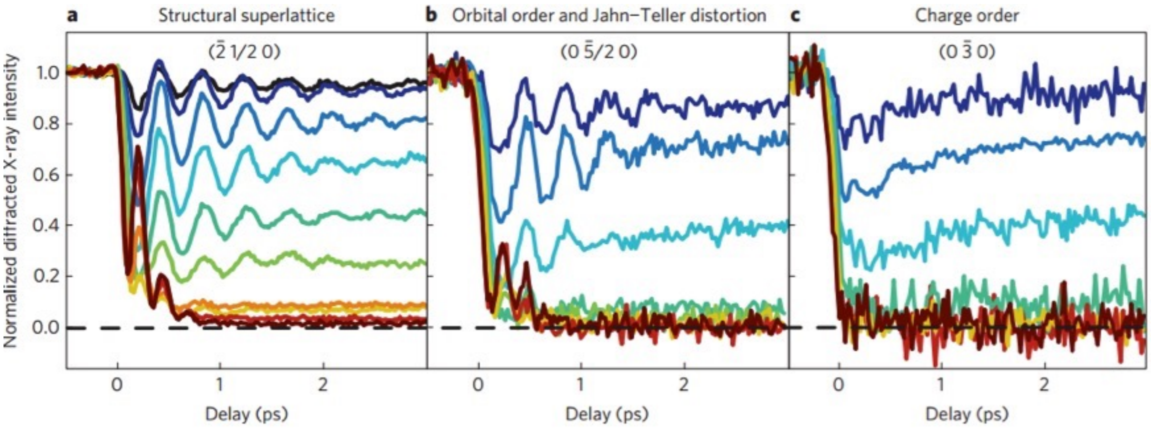

Figure 1.7 Measured evolution of the normalized X-ray intensity for three super lattice reflections. Adapted and modified from Ref. [12].

important concept in condensed matter physics, not just in electronic materials, but also phononic, mechanical, and even biological materials. Research on topological materials has been rapidly evolving over the past decade [39], two-dimensional [41]. Topological nature of certain electron systems depend on lattice distortions through the electron-lattice coupling. A good example is the one-dimensional Su-Schrieffer-Heeger(SSH) model. For this model, based on a topological reason, at the open edges or the antiphase boundaries could host zero energy states [31, 10].

Third, we extend our study to mechanical meta materials. A great attention has been focused on topological matematerials, lately. Examples include phonic, sonic and mechanical metamaterials, as shown in Figure 1.8 [58] and 1.10 [46]. Since widely different systems could share phenomena of the same topological origin, the tight binding electronic Hamiltonian for the Haldane model of graphene [28] has been translated to equations describing topological phenomena in photonic, sonic, and mechanical metamaterials, as well as ultracold fermions [46, 58, 34, 69, 55], for example. Therefore, we develop a model mechanical system of spinners interacting via magnets, which can simulate the electronic model above. We compare our results for 1D system with preliminary experimental data, and make predictions for 2D system

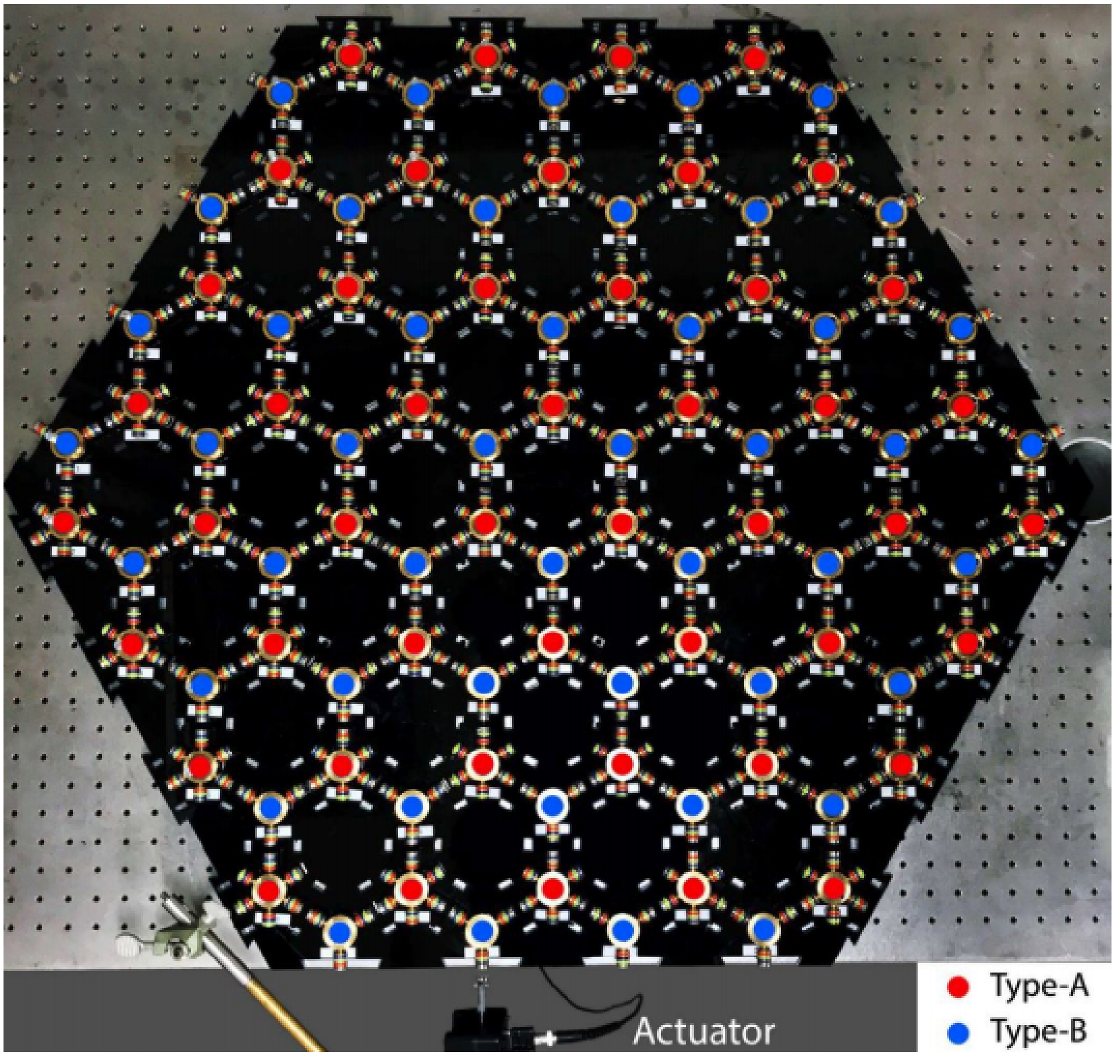

Figure 1.8 Example of mechanical metamaterials, made of array of spinners [9, 58]. Adapted and modified from Ref. [58].

with open edges and topological edge modes that can be tested by future experiments.

In this dissertation, we study a two-dimensional model system with strong electron-lattice coupling. We find this particular model has a non-trivial topological electronic property that depends on the lattice distortion. We investigate topologically protected zero energy states within structural textures, such as antiphase boundaries and twin boundaries. We also proposed an experiment that can realize our theoretical results in mechanic meta-materials.

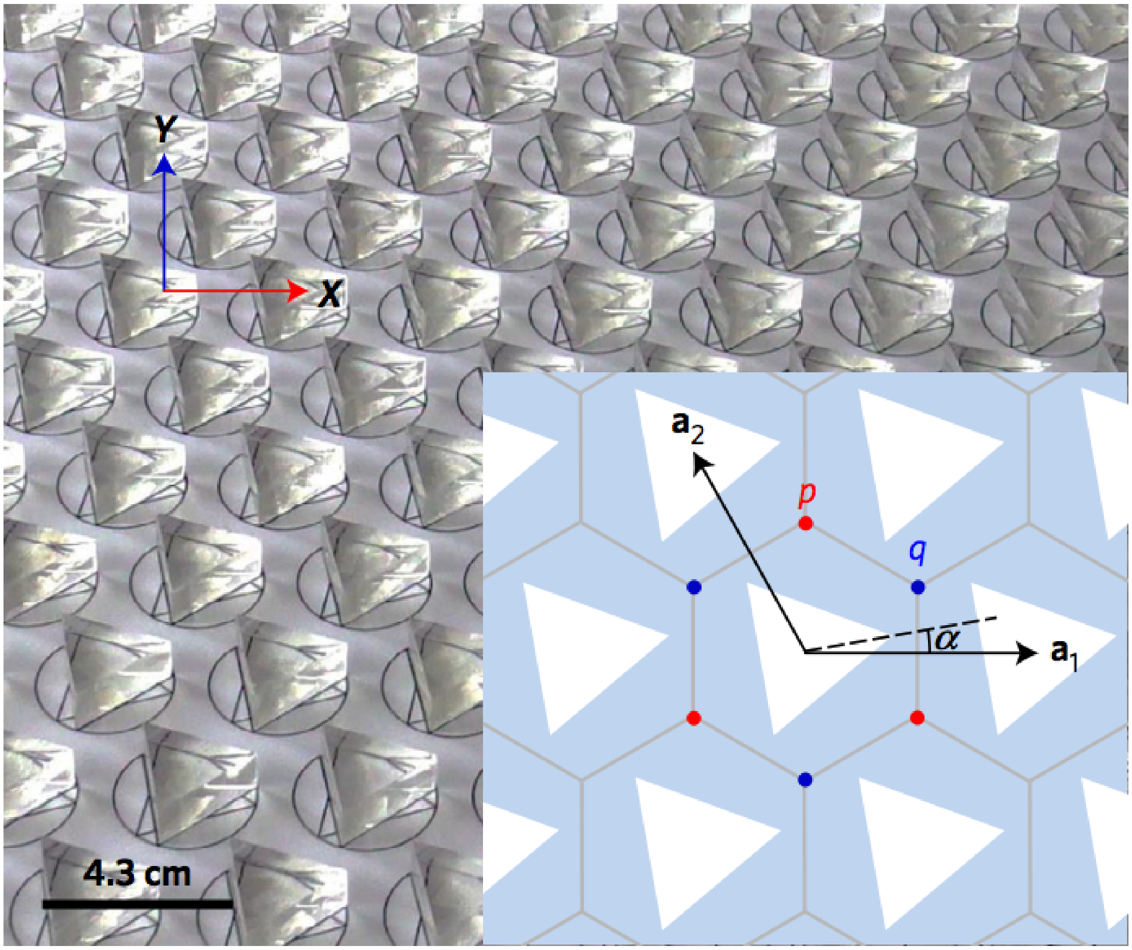

Figure 1.9 Example of sonic metamaterials. Sound waves propagate between triangular rods. Adapted and modified from Ref. [46]

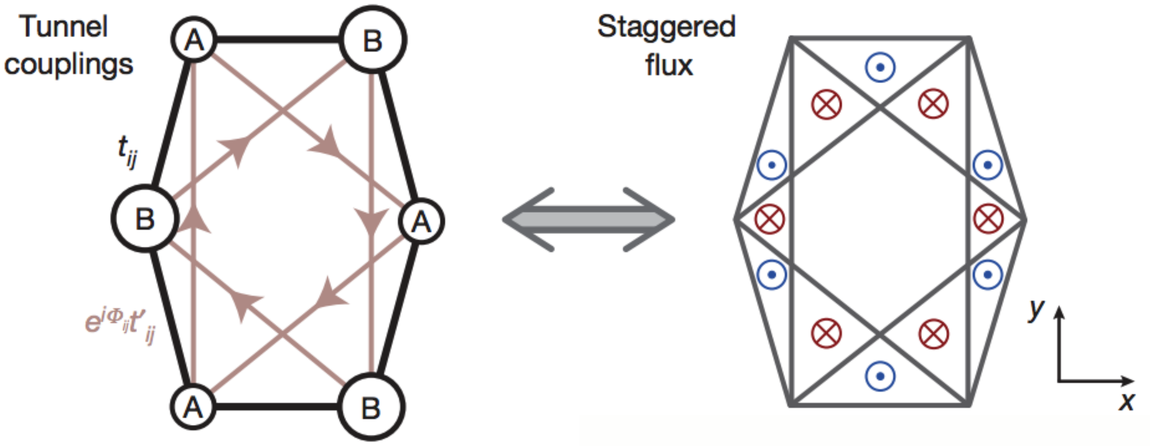

Figure 1.10 Example of ultracold fermions. Ultracold fermion gas used to periodically modulated the optical lattice. Adapted and modified from Ref. [34]

In broad context, the importance of our work lies in the proposal of new ways to control of material properties through structures, either through photo-induced insulator-metal transition or creating domain walls or open edges. Such controls would lead new device applications, which could be technologically important.

CHAPTER 2

PHOTOINDUCED NONEQUILIBRIUM DYNAMICS IN CHARGE ORDERED MATERIALS

The work in this chapter was done in collaboration with Dr. Michel van Veenendaal and Dr. Tsezar F. Seman from Advanced Photon Source at Argonne National Laboratory and Department of Physics at Northern Illinois University, and Prof. Keun Hyuk Ahn from Department of Physics at New Jersey Institute of Technology.

2.1 Introduction

Advances in computing and communication technology demand ultrafast switching devices. Recently, photoinduced insulator-metal transitions in charge ordered (CO) or charge density wave (CDW) materials have been considered as a mechanism for future ultrafast switching devices. [62, 18, 72] In addition, studies of photoinduced nonequilibrium dynamics have revealed properties and phases of materials inaccessible through equilibrium thermodynamic processes. [74, 36] One class of materials of particular interest are transition metal oxides of perovskite or Ruddlesden-Popper structure, which include manganites, cuprates, and nickelates. [48, 57, 47, 17, 23, 73] The layers of $M\mathrm{O}_2$, where M and O represent a transition metal element and oxygen respectively, play a dominant role in electronic properties of these materials. For example, time-resolved experiments on $\mathrm{Pr}_{0.5}\mathrm{Ca}_{0.5}\mathrm{MnO}_3$ in a CO phase using ultrashort optical pump and x-ray probe at or off resonance have revealed decoupled nonequilibrium dynamics of electrons and periodic lattice distortion during photoinduced melting of the CO phase. [12]

In spite of the recent experimental progress, theoretical and computational studies of nonequilibrium dynamics in CO and related CDW materials have been restricted to phenomenological Ginzburg-Landau approaches, [12] calculations of carrier-doping effects using density functional theory, [64] and models based on dynamics of the electronic density of states (DOS). [67]

In this thesis work, we present simulations of the photoinduced CO insulator-metal transitions in a model MO_2 system, using a tight-binding Hamiltonian and a coupling between the electrons on M ions and distortion of O ions. The dynamics of the periodic lattice distortion is treated classically. The electron dynamics follows the Boltzmann equations, as done in References. [25, 26, 59, 21, 1, 67]. The CO phase is recovered through the coupling between the electron system and a phonon thermal reservoir. Detailed time-domain studies of photoinduced melting of CO, particularly dynamics of the energy landscape, are presented. The results reveal nonequilibrium dynamics of the electronic order parameter and the periodic lattice distortion under various conditions of the photon energy and the pump fluence. In addition to the CO in transition metal oxides, the results are compared with experiments on CDW materials of other structures, because both phenomena involve coupled electron density modulation and lattice distortions.

The work is organized as follows. Section 3.2 presents the model system and equations governing the dynamics of the model system. Results of our simulations are shown in Section 3.3 and compared with experimental results in Section 2.6. A summary is provided in Section 3.4.

2.2 Review of Complex Oxides with Charge and Orbital Order

Competing interactions result in diverse exciting phase is charge and orbital ordered phase. The mixed valance character of transition metal ions often allow these ions have average electron numbers between integer values. For example, perovskite manganites of $\mathrm{RE}_{1-\mathrm{x}}\mathrm{AK}_{\mathrm{x}}\mathrm{MnO}_3$ have the average Mn ionic state of $3 + x$. If all Mn ions have this average ionic state, then the perovskite manganites could have metallic phase. However, the electron-electron interaction a electron-lattice interaction may favor localized electron states, which gives rise to two distinct ionic states for Mn, or transition metal ions. When this occurs, to minimize energy of the system, these distinct charge states tend to order in certain ways, which is called charge ordering (CO). When there exist multiple possibilities of orbital states, orbital state could be also ordered, which is called orbital ordering (OO). Examples of materials with CO/OO phases are high-T_c superconductor cuprates [13], colossal magnetoresistive [20, 66, 70, 19], verwey transitional magnetite (Fe_3O_4) [68], and rare earth perovskite vanvadunce oxide $\mathrm{ReVO_3}$ [51, 50]. Often CO/OO accompanies magnetic ordering, because transition metal ions have magnetic moments which interacts through superexcharge a double exchange interaction CO/OO is coupled to magnetic order, and CO/OO patterns sometimes decide magnetic ordering pattern [20, 66, 70, 19]. Various theoretical approaches often include the Hubbard on-site Coulomb interaction, the Hund's interactions with core spins, the Jahn-Teller electron-lattice interaction, and super exchange interactions [54].

2.3 Review of Pump-probe Experiment on Complex Oxides

With multiple degrees of freedom, spin, charge, orbital, and phonons, coupling strongly each other, transition metal oxides provides great challenges to theorists and experimentalists [75]. In spite of arrays of probes of different length scales, from atomic scale to mesoscopic scale, experimental data for equilibrium or near-equilibrium states may not be useful to test competing theories. Nonequilibrium probes, such as various time-resolved ultrafast pump-probe experiments, provide much more detailed information on the coupling between different degrees of freedom, which could test competing theories. Furthermore, as the speed of devices became even faster, understanding the ultrafast noneqquilibrium dynamics has became crucial for the development of such devices. In particular, ultrafast photo-induced transition between CO/CDW insulating phases and metallic phases, the focus in this chapter, could be utilized for making ultrafast switching devices. Such photoinduced phase transitions have been observed in VO_2 [15, 38, 56, 32, 45, 11, 37, 14, 60, 16], in $La_{1.8-x}EuSr_xCuO_4$ ($x = 0.125$) [24], and $Pr_{0.7}Ca_{0.3}MnO_3$ [61], just to name a few. In this these, we focus on manganites as a specific exchange, but the results of our simulation are relevant to photo-induced CO/CDW to metal transitions in other transition metal oxides as well.

2.4 Model

2.4.1 Hamiltonian

We consider a model system of a $N \times N$ $M\mathrm{O}_2$ square lattice with periodic boundary conditions, shown in Figure. 2.1. To capture the essential mechanism of CO transition in a model, we consider one spinless isotropic electron orbital per M ion. The electron creation operator on the M site at $\mathbf{n} = (n_x, n_y)$ is represented by $c^\dagger_{\mathbf{n}}$. In this model, the CO instability arises as a result of Fermi surface nesting and electron-lattice coupling. Therefore, we include the displacements of the O ions at $\mathbf{n} + \mathbf{e}_a/2$ along the a-direction represented by $u^a_{\mathbf{n}}$ in the model, where $a = x, y$. One electron is present per two M sites in the system, which would result in the checkerboard CO state and the lattice distortions shown in Figure. 2.1. The periodic distortion of the O ions is parameterized by a classical variable u, as indicated in Figure. 2.1. Motion of the M ions is not considered because the O ions move symmetrically with respect to the M ions. The periodic distortion of the O ions is parameterized by a classical variable u, defined by

$$\begin{aligned} u^x_{\mathbf{n}} &= (-1)^{n_x+n_y} u, & (2.1) \\ u^y_{\mathbf{n}} &= (-1)^{n_x+n_y} u. & (2.2) \end{aligned}$$

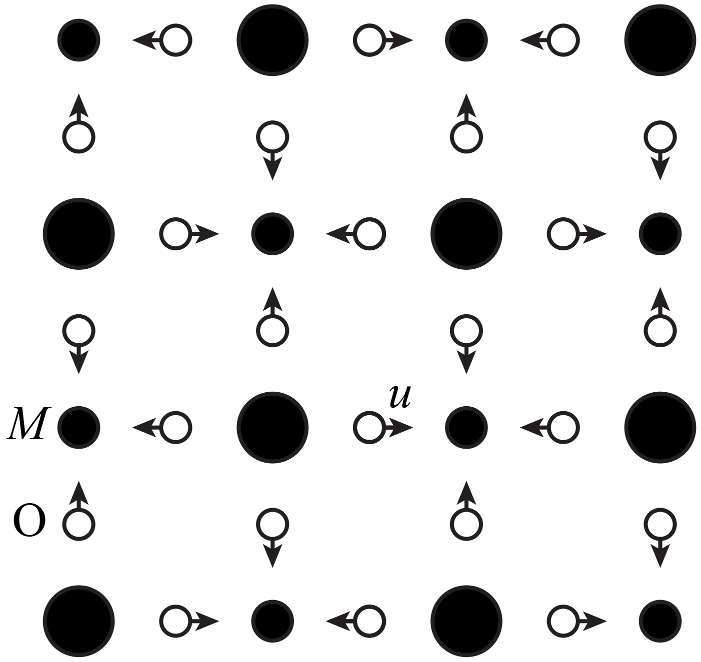

Figure 2.1 The model system of an $M\mathrm{O}_2$ square lattice with periodic boundary conditions. The size of the solid circles schematically represents the variation of electron density on M ions in CO state. Arrows show the displacements of the O ions, represented by u. Adapted from Ref. [77].

The Hamiltonian for electrons has two terms. The first term represents the electron hopping between the nearest neighbor M sites, given by

$$H_{\text{hop}} = -t_h \sum_{\mathbf{n}} \left(c^\dagger_{\mathbf{n}} c_{\mathbf{n}+\mathbf{e}_x} + c^\dagger_{\mathbf{n}} c_{\mathbf{n}+\mathbf{e}_y} + \text{H.c.} \right), \tag{2.3}$$

where t_h is the electron hopping constant. The second term represents the coupling between the electron at M site and the distortion of the surrounding negatively-charged O ions, given by

$$H_{\text{el-latt}} = -\lambda \sum_{\mathbf{n}} \frac{u^x_{\mathbf{n}} - u^x_{\mathbf{n}-\mathbf{e}_x} + u^y_{\mathbf{n}} - u^y_{\mathbf{n}-\mathbf{e}_y}}{4} c^\dagger_{\mathbf{n}} c_{\mathbf{n}}, \tag{2.4}$$

where λ is the electron-lattice coupling constant. The potential and the kinetic energies of the O ions are treated classically, and represented by the Hamiltonian term

$$H_{\text{latt}} = \sum_{\mathbf{n}} \left[\frac{K}{2} \left(u_{\mathbf{n}}^{x\,2} + u_{\mathbf{n}}^{y\,2} \right) + \frac{m}{2} \left(v_{\mathbf{n}}^{x2} + v_{\mathbf{n}}^{y2} \right) \right], \tag{2.5}$$

where K is the force constant associated with the O ion displacements, m is the mass of the O ion, and $v_{\mathbf{n}}^{a} = du_{\mathbf{n}}^{a}/dt$ $(a = x, y)$ is the velocity.

The total Hamiltonian is the sum of the above terms,

$$H_{\text{tot}} = H_{\text{hop}} + H_{\text{el-latt}} + H_{\text{latt}}, \tag{2.6}$$

which results in the electron energy levels,

$$\varepsilon_{l\mathbf{k}} = (-1)^{l} \sqrt{4t_h^2 (\cos k_x + \cos k_y)^2 + \lambda^2 u^2}, \tag{2.7}$$

with the band index $l = 0, 1$ and $\mathbf{k} = (k_x, k_y)$ in the first Brillouin zone $\Omega_{1\text{BZ}} = \{\mathbf{k} |\, |k_x| + |k_y| \leq \pi\}$. The distribution function for the state $|l\mathbf{k}\rangle$ is represented by $f_{l\mathbf{k}}$. A gap $\Delta_{\text{gap}} = 2\lambda\, |u|$ occurs at the boundary of $\Omega_{1\text{BZ}}$. The metallic state with $u = 0$ has a Peierls instability with the Fermi surface nesting vector $\mathbf{Q} = (\pi, \pi)$. Therefore, the CO insulating phase develops, as $|u|$ becomes finite. An example of the electron DOS per site $D_e(\varepsilon)$ in the CDW phase is shown in Figure. 2.2(a). [1]

The order parameter for the CO state is defined as the $\mathbf{Q} = (\pi, \pi)$ component of the charge density modulation at the M ion sites that is,

$$\delta n = \frac{1}{N^2} \sum_{\mathbf{n}} e^{i\mathbf{Q}\cdot\mathbf{n}} \langle c_{\mathbf{n}}^{\dagger} c_{\mathbf{n}} \rangle. \tag{2.8}$$

We choose the size of our system $N = 512$. The hopping constant $t_h = 0.5$ eV, the electron-lattice coupling constant $\lambda = 0.936$ eV Å^{-1}, and the force constant $K = 0.85$ eV Å^{-2} are chosen similar to the values used for perovskite manganites. [5, 6] The mass of the oxygen ion is $m = 1.66$ meV ps^2 Å^{-2}. While the dynamics of a

---

[1] In our simulations, the size of the energy bin is about 1.7 meV, which would result in large fluctuations in the electron DOS due to finite size effects. Therefore, for clarity, we apply a Gaussian smoothing to the electron DOS plotted here

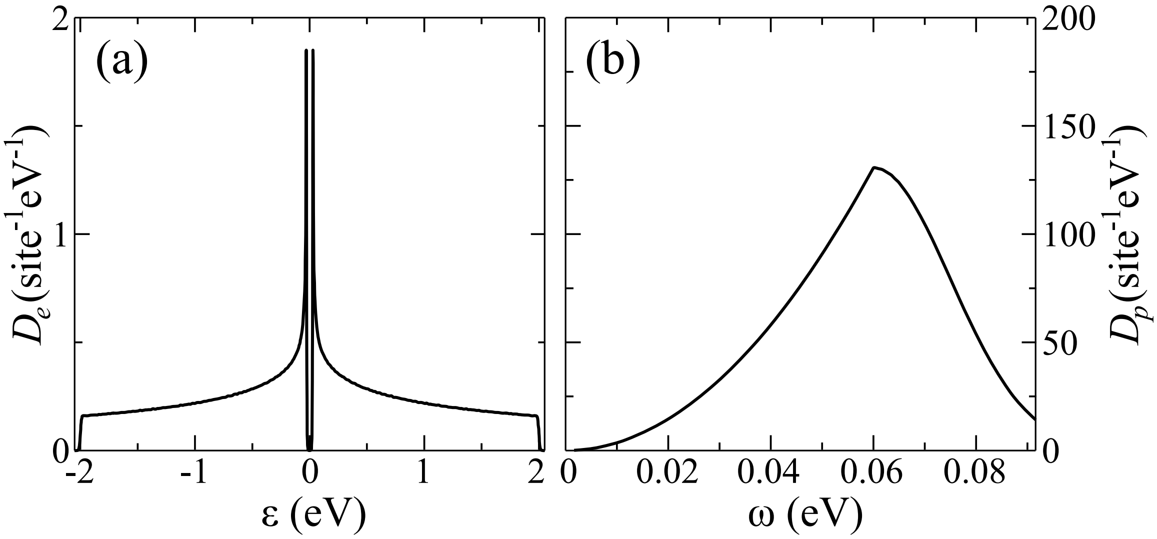

Figure 2.2 (a) Example of DOS per site for electrons D_e versus energy ε. The band gap is 58.9 meV. (b) DOS per site for phonons D_p versus phonon energy ω. Adapted from Ref. [77].

particular phonon mode directly coupled to the CO is coherent and parameterized by u, the rest of phonon system is assumed to be incoherent and play the role of a thermal reservoir to the electron system excited by the optical pump, because the phonon system has a much greater specific heat than the electron system.

The phonon system has a much greater specific heat than the electron system and plays the role of a thermal reservoir to the electron system excited by the optical pump. We describe the state of the incoherent phonon system by the Bose-Einstein distribution function b_ω with the temperature fixed at the initial temperature T_i as done in Reference. [25, 26]. To simulate such a role, we include the phonon system in the model and consider the scattering between electrons and phonons. The phonon DOS per site $D_p(\omega)$ is obtained by modifying the Debye model. Below the Debye energy ω_D, $D_p(\omega)$ is proportional to ω^2. Above ω_D, a Gaussian function is assumed with the peak at ω_D matched to $D_p(\omega)$ of the Debye model,

$$D_p(\omega) = \begin{cases} \zeta\omega^2 & \text{for } 0 \le \omega \le \omega_D, \\ \zeta\omega_D^2 e^{-(\omega-\omega_D)^2/\eta^2} & \text{for } \omega > \omega_D, \end{cases} \tag{2.9}$$

where ζ and η are fitting parameters. We choose $\omega_D = 60 \quad \text{meV}$, $\zeta = 3.63 \times 10^{-5}$ meV^{-3}, and $\eta = 15$ meV. The total number of phonon modes per site is chosen as 5 to match to the number of longitudinal phonon modes per transition metal ion in perovskite transition metal oxides. The DOS for phonons for the simulations is shown in Figure. 2.2(b). The state of the phonon system is described by the Bose-Einstein distribution function b_ω,

$$b_\omega = \frac{1}{e^{\omega/k_B T_i} - 1}, \tag{2.10}$$

with the temperature fixed at the initial temperature T_i.

Then, we describe how the dynamics of the model system is simulated, after the electron system is excited by the optical pump. Electron-lattice interactions specified by Eq. (2.4) result in intricately coupled nonequilibrium electron-lattice dynamics, which is the focus of the current study. At each time step of the computation, lattice and electron dynamics are considered and various quantities are calculated as follows.

2.4.2 Lattice Dynamics

In the model, the coherent lattice distortion parameterized by u is treated classically and follows Newtonian dynamics. The corresponding potential energy per site is given by

$$U(u) = \frac{1}{N^2} \sum_{l\mathbf{k}} \varepsilon_{l\mathbf{k}}(u) f_{l\mathbf{k}} + Ku^2. \tag{2.11}$$

The Lagrangian per site $\mathcal{L} = mv^2 - U(u)$ with $v = du/dt$ and the damping lead to the equation for the dynamics of the distortion u,

$$2m\frac{d^2u}{dt^2} = -2Ku - \frac{1}{N^2} \sum_{l\mathbf{k}} \frac{\partial \varepsilon_{l\mathbf{k}}(u)}{\partial u} f_{l\mathbf{k}} - \gamma \frac{du}{dt}, \tag{2.12}$$

where a value of damping constant $\gamma = 9$ meV ps Å^{-2} is chosen, so that the decay rate of the oscillation is similar to experiments. [12]

The lattice and electron dynamics are coupled through the potential energy $U(u)$ in Equations (2.11) and (2.12). The lattice dynamics depends on the electronic state, because the potential energy $U(u)$ depends on $f_{l\mathbf{k}}$. The electron dynamics depends on the lattice dynamics, because the electron energy levels $\varepsilon_{l\mathbf{k}}(u)$, the electron DOS $D_e(\varepsilon, u)$, and the size of the gap $\Delta_{\text{gap}} = 2\lambda|u|$ depend on the lattice distortion u and affect electron-electron and electron-phonon scattering. The Lagrangian per site, $\mathcal{L} = Mv^2 - U(u)$, and the damping lead to the equation for the dynamics of the distortion u,

2.4.3 Electron Dynamics

Dynamics of electrons in the model is governed by the Boltzmann equations that describe electron-electron and electron-phonon scattering. For the Boltzmann equations, the electron distribution function $f_{l\mathbf{k}}$ with band and momentum indices, used for the lattice dynamics, is converted into an electron distribution function f_ε with an energy index. The transformation between $f_{l\mathbf{k}}$ and f_ε is carried out according to

$$D_e(\varepsilon) f_\varepsilon = \frac{1}{N^2} \sum_{l\mathbf{k}} f_{l\mathbf{k}} \delta(\varepsilon_{l\mathbf{k}} - \varepsilon) \tag{2.13}$$

As done in References. [21, 59, 25, 26, 1], the momentum conservation is integrated out under the approximation of isotropic Debye phonons and electrons with isotropic parabolic dispersion relation. This gives rise to the following equations

$$\frac{df_\varepsilon}{dt} = \left(\frac{df_\varepsilon}{dt}\right)_{\text{ee}} + \left(\frac{df_\varepsilon}{dt}\right)_{\text{ep}}, \tag{2.14}$$

where

$$\begin{aligned}\left(\frac{df_\varepsilon}{dt}\right)_{\text{ee}} = \; & \frac{K_{\text{ee}}}{2} \int \big[- f_\varepsilon f_{\varepsilon'} (1 - f_{\varepsilon''})(1 - f_{\varepsilon+\varepsilon'-\varepsilon''}) \\ & +(1 - f_\varepsilon)(1 - f_{\varepsilon'}) f_{\varepsilon''} f_{\varepsilon+\varepsilon'-\varepsilon''} \big] \\ & \times D_e(\varepsilon') D_e(\varepsilon'') D_e(\varepsilon + \varepsilon' - \varepsilon'') d\varepsilon' d\varepsilon'' \end{aligned} \tag{2.15}$$

represents the electron-electron scattering, and

$$\begin{aligned}\left(\frac{df_\varepsilon}{dt}\right)_{\text{ep}} &= K_{\text{ep}}\int \big\{ \big[f_{\varepsilon+\omega}(1-f_\varepsilon)(b_\omega+1) \\ &\quad - f_\varepsilon(1-f_{\varepsilon+\omega})b_\omega \big] D_p(\omega)D_e(\varepsilon+\omega) \\ &\quad + \big[f_{\varepsilon-\omega}(1-f_\varepsilon)b_\omega - f_\varepsilon(1-f_{\varepsilon-\omega})(b_\omega+1)\big] \\ &\quad \times D_p(\omega)D_e(\varepsilon-\omega)\big\}\, d\omega \qquad (2.16)\end{aligned}$$

represents the electron-phonon scattering, in terms of electron and phonon distribution functions, f_ε and b_ω, and corresponding DOS, $D_e(\varepsilon)$ and $D_p(\omega)$. The number of energy bins is chosen as $N_e = 2400$, which results in an energy bin size of about 1.7 meV. The constants for the electron-electron and the electron-phonon scattering are $K_{\text{ee}} = 1953$ eV ps^{-1} and $K_{\text{ep}} = 0.2325$ eV ps^{-1}, chosen with the same order of magnitude as the values used in References. [21, 1].

2.4.4 Approximations Used

We list some of the approximations chosen for the model and discuss why they are reasonable. In the simulations, the electron DOS plays a dominant role in dynamics. Electron hopping amplitudes beyond the nearest neighbors are not only small, but also have a negligible effect on the electron DOS, which justifies the approximation of including only the nearest neighbor hopping. An approximation has been also made for the effect of the optical pump. The main focus of the simulations is the dynamics *after* the optical pump, not *during* the optical pump. Further, the typical width of the optical pulse, ~10 fs, is much shorter than the period of coherent oscillation, ~500 fs. Therefore, the dynamics during the optical pump is irrelevant for the simulation and we approximate the effect of the optical pump as an instantaneous electronic excitation, [1, 21] as described in Section 3.3 A.

Finally, all phonon modes, except one primary coherent distortion mode parameterized by u, have no memory of the phonons emitted or absorbed by electrons, and are treated as a thermal reservoir at a fixed temperature. The effect of dynamic incoherent phonon distribution is expected to be small, because the phonons have a much greater specific heat than the electrons. Excitations of other coherent phonon modes coupled to the primary coherent phonon mode could be incorporated in the model by including anharmonic coupling between various coherent phonon modes, as postulated for perovskite manganites. [12]

With these reasonable approximations, we capture essential features of CO and its photoinduced dynamics in a simple model, and obtain results which could spur future experiments. The model also provides a computational framework, upon which more realistic models could be built.

2.5 Results

2.5.1 Equilibrium States and Excitations by Optical Pump

Before presenting the results for the nonequilibrium dynamics, we discuss the equilibrium properties of the system and the effects of the optical pump. To ensure consistency, the dynamics simulation itself is used to obtain the equilibrium states $f_\varepsilon^{\mathrm{eq}}$ and u_{eq}, which show a second order phase transition with a critical temperature of $T_c \approx 217$ K and $u_{\mathrm{eq}}(T \approx 0) = 0.035$ Å. With the periodic distortion u treated classically and its quantum fluctuations neglected, the equilibrium properties of the model are similar to the predictions made by mean field theories. [27] To ensure consistency with the simulations on nonequilibrium states, the dynamics simulation itself is used to obtain the equilibrium states. Starting from various initial states, simulations are run until the distortion u and the distribution function f_ε reach the equilibrium u_{eq} and $f_\varepsilon^{\mathrm{eq}}$. By fitting $f_\varepsilon^{\mathrm{eq}}$ to the Fermi-Dirac distribution, the temperature T is obtained. The red line in Figure. 2.3 shows u_{eq} versus T, which indicates a second order phase transition with a critical temperature of $T_c \approx 217$ K. The ratio between the CDW gap at $T \approx 0$ K, $\Delta_{\mathrm{gap}}(T \approx 0 \text{ K}) = 65.5$ meV, and

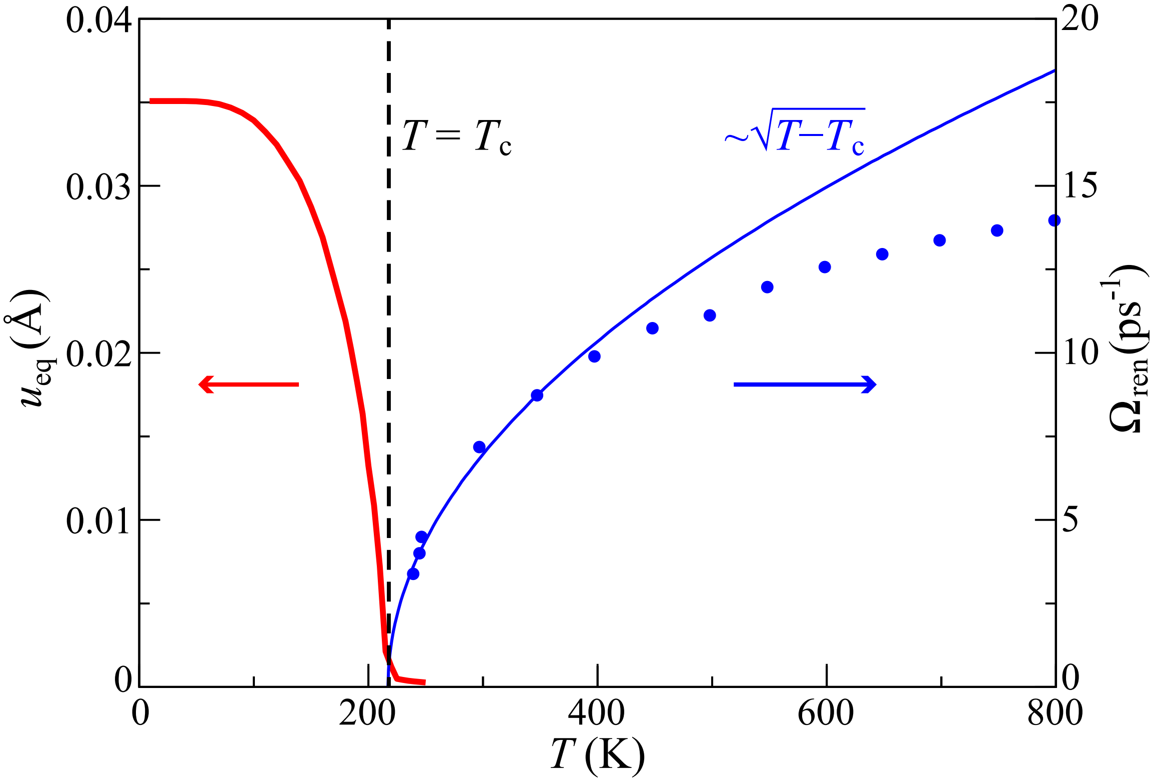

Figure 2.3 (Color online) The red line shows the equilibrium distortion $u_{\rm eq}$ of the B ions versus temperature T. The critical temperature is about $T_{\rm c} \approx 217$ K. The blue dots represent the renormalized frequency $\Omega_{\rm ren}$ for the oscillation of u at $T > T_c$. The blue line represents the fit to the mean field theory predictions near T_c.

$k_B T_c = 18.7$ meV is 3.50, consistent with the mean field value of 3.52 (Reference. [27]). Of relevance for the nonequilibrium dynamics is the Kohn anomaly, [27, 71] a softening of the phonon mode responsible for the CDW when approaching T_c from above. The renormalized angular frequencies $\Omega_{\rm ren}$ are obtained by introducing a small perturbation u from equilibrium. [2] The results (blue dots in Figure. 2.3) are consistent with the mean field square-root temperature dependence, $\sqrt{T - T_c}$, for $T \gtrsim T_c$ (blue line in Figure. 2.3).

As mentioned in Section 3.2 D, the effect of the optical pump is considered as an instantaneous electron excitation. Therefore, the distribution function for the upper and lower bands at $t = 0$, right after the optical pump, is altered from the equilibrium

---

[2] The size of the perturbation in u is chosen as 0.005 Å.

distribution $f_\varepsilon^{\mathrm{eq}}$ by a Gaussian function,

$$f_\varepsilon(t=0) = f_\varepsilon^{\mathrm{eq}} \pm \delta f \exp\left[-\frac{(2\varepsilon \mp E_{\mathrm{photon}})^2}{8W^2}\right], \tag{2.17}$$

where E_{photon} is the median photon energy in the optical pump, and δf is the maximum change in the distribution function. The fluence per site F of the optical pump is calculated as the change in electronic energy at $t = 0$. For most results in this thesis work, we take an initial temperature of $T_i = 135$ K, for which the equilibrium distortion, order parameter, and CO gap are $u_{\mathrm{eq}} = 0.031$ Å, $\delta n_{\mathrm{eq}} = 0.056$, and $\Delta_{\mathrm{gap}} = 58.9$ meV, respectively. The width of the pump beam is fixed as $W = 0.02$ eV for most simulations.

2.5.2 Nonequilibrium Dynamics Induced by Photons with $E_{\mathrm{photon}} \gg \Delta_{\mathrm{gap}}$

Since the early-time dynamics and the energy efficiency of melting the CO depend sensitively on the photon energy, the results for $E_{\mathrm{photon}} \gg \Delta_{\mathrm{gap}}$ and $E_{\mathrm{photon}} = \Delta_{\mathrm{gap}}$ are presented separately in this and the next Sections. The results for $E_{\mathrm{photon}} = 2$ eV, much greater than $\Delta_{\mathrm{gap}} = 58.9$ meV, and fluences large enough to melt the CO are presented in Figures 2.4 and 2.5. In Figure 2.4, the electron distribution functions for selected times are shown to demonstrate the evolution of $f(\varepsilon)$. Video simulations of $f(\varepsilon, t)$ for the $E_{\mathrm{photon}} \gg \Delta_{\mathrm{gap}}$ and $E_{\mathrm{photon}} = \Delta_{\mathrm{gap}}$ cases are provided in the supplementary material. In Figure 2.5, the evolution of various quantities are shown. To reveal the fast early dynamics and slow late dynamics in the same figure, the dynamics during -0.1-2 ps and 2-50 ps are displayed in different time scales. To parameterize the energy of the electron system at time t, the effective temperature $T_{\mathrm{eff}}(t)$ in the nonequilibrium state is defined by matching the total energy between the actual and the Fermi-Dirac distributions, that is,

$$\int_{-\infty}^{\infty} \varepsilon f(\varepsilon, t) D_e(\varepsilon, t) d\varepsilon = \int_{-\infty}^{\infty} \varepsilon f_{\mathrm{FD}}(\varepsilon, T_{\mathrm{eff}}(t)) D_e(\varepsilon, t) d\varepsilon, \tag{2.18}$$

where $f_{\mathrm{FD}}(\varepsilon, T_{\mathrm{eff}}(t))$ is the Fermi-Dirac distribution function with the temperature $T_{\mathrm{eff}}(t)$ and the chemical potential zero. Figure 2.5(a) shows the difference between T_{eff} and the initial temperature T_i before the pump, which is a measure of the excess energy in the electron system. The effective electron temperature T_{eff} increases to 907 K right after the optical pump. The semilogarithmic plot of $T_{\mathrm{eff}} - T_i$ versus time t reveals three distinct exponential decay rates, $r = 0.202$ ps^{-1} up to around 16 ps, $r = 0.013$ ps^{-1} between 16 ps and 21 ps, and $r = 0.053$ ps^{-1} after around 21 ps, which correspond to three stages of the relaxation process, that is, stages of CO melting, CO gap reopening, and thermal relaxation. Such multistage relaxation has been observed in CO or CDW materials. [22] We now discuss these different stages in more detail.

As shown in Figure. 2.4(a), initial electron-hole excitations for $E_{\mathrm{photon}} \gg \Delta_{\mathrm{gap}}$ occur far away from the CO gap, but fast electron-electron scattering removes the Gaussian peak features at $\varepsilon = \pm E_{\mathrm{photon}}/2$ within 0.15 ps, initiating the stage of CO melting. As mentioned in Section 3.2, the CO accompanies periodic lattice distortions. Such electronic and lattice modulations would produce superlattice peaks in x-ray and neutron scattering. Their normalized intensities are approximately squares of the displacement u or the CO density δn normalized to the equilibrium values at temperature T_i before the optical pump,

$$\begin{aligned} \bar{u}^2(t) &= \left[u(t)/u_{\mathrm{eq}}(T_i)\right]^2, \\ \delta\bar{n}^2(t) &= \left[\delta n(t)/\delta n_{\mathrm{eq}}(T_i)\right]^2. \end{aligned} \tag{2.19}$$

In equilibrium, u and δn are directly related to each other via

$$u_{\mathrm{eq}} = \frac{\lambda}{2K}\delta n_{\mathrm{eq}}. \tag{2.20}$$

Therefore, we define

$$\bar{d}(t) = \bar{u}^2(t) - \delta\bar{n}^2(t) \tag{2.21}$$

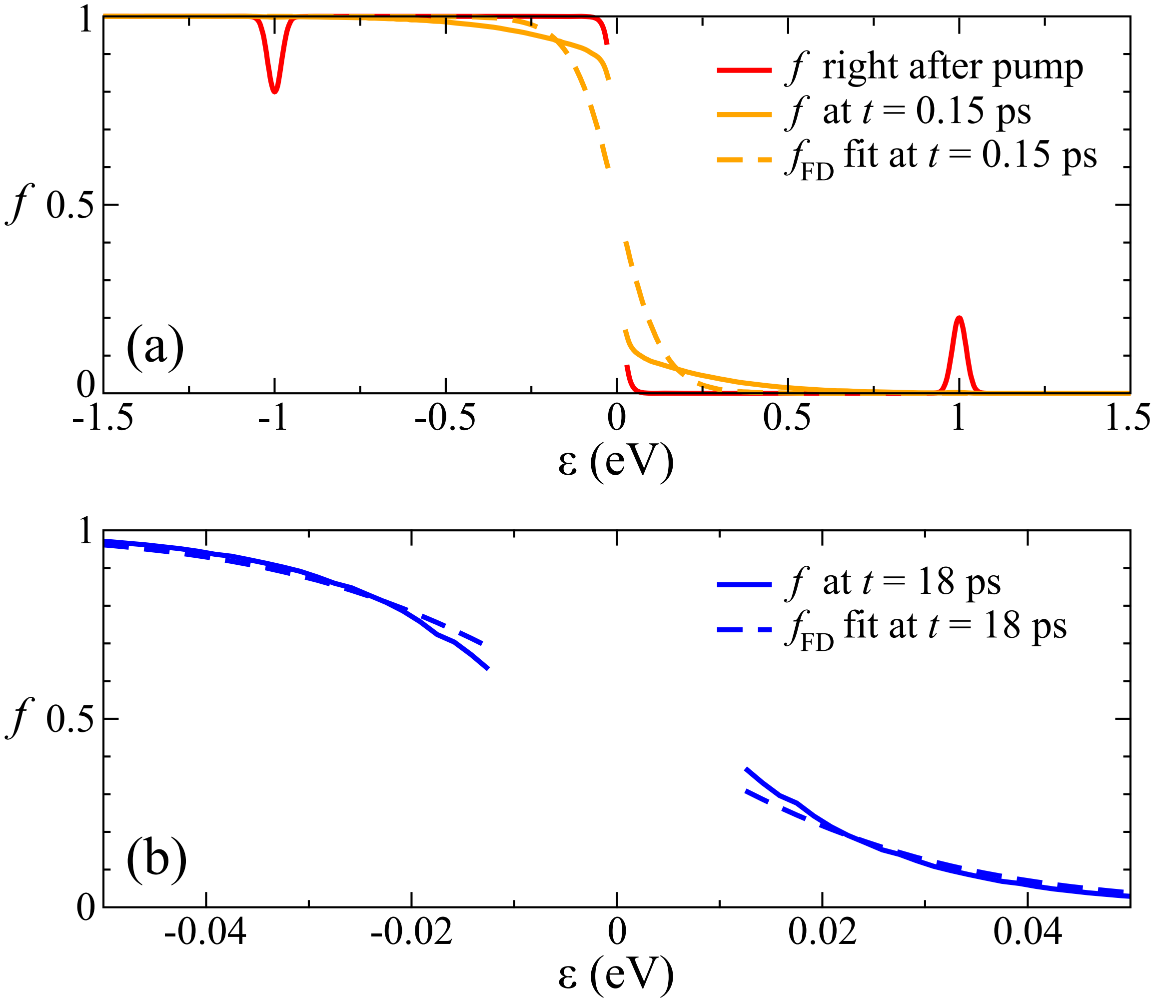

Figure 2.4 Examples for the evolution of the distribution function f versus energy ε for $E_{\text{photon}} \gg \Delta_{\text{gap}}$. (a) The red line shows the distribution function right after the optical pump, $t = 0$; the solid orange line represents the distribution function at $t = 0.15$ ps. The Fermi-Dirac distribution at the corresponding effective temperature $T_{\text{eff}} = 904$ K, defined by Eq. (2.18), at $t = 0.15$ ps is shown in a dashed orange line. (b) The solid blue line represents the electron distribution at $t = 18$ ps during the gap reopening. The Fermi-Dirac distribution with the corresponding effective temperature $T_{\text{eff}} = 177$ K at $t = 18$ ps is shown in a dashed blue line. Adapted from Ref. [77].

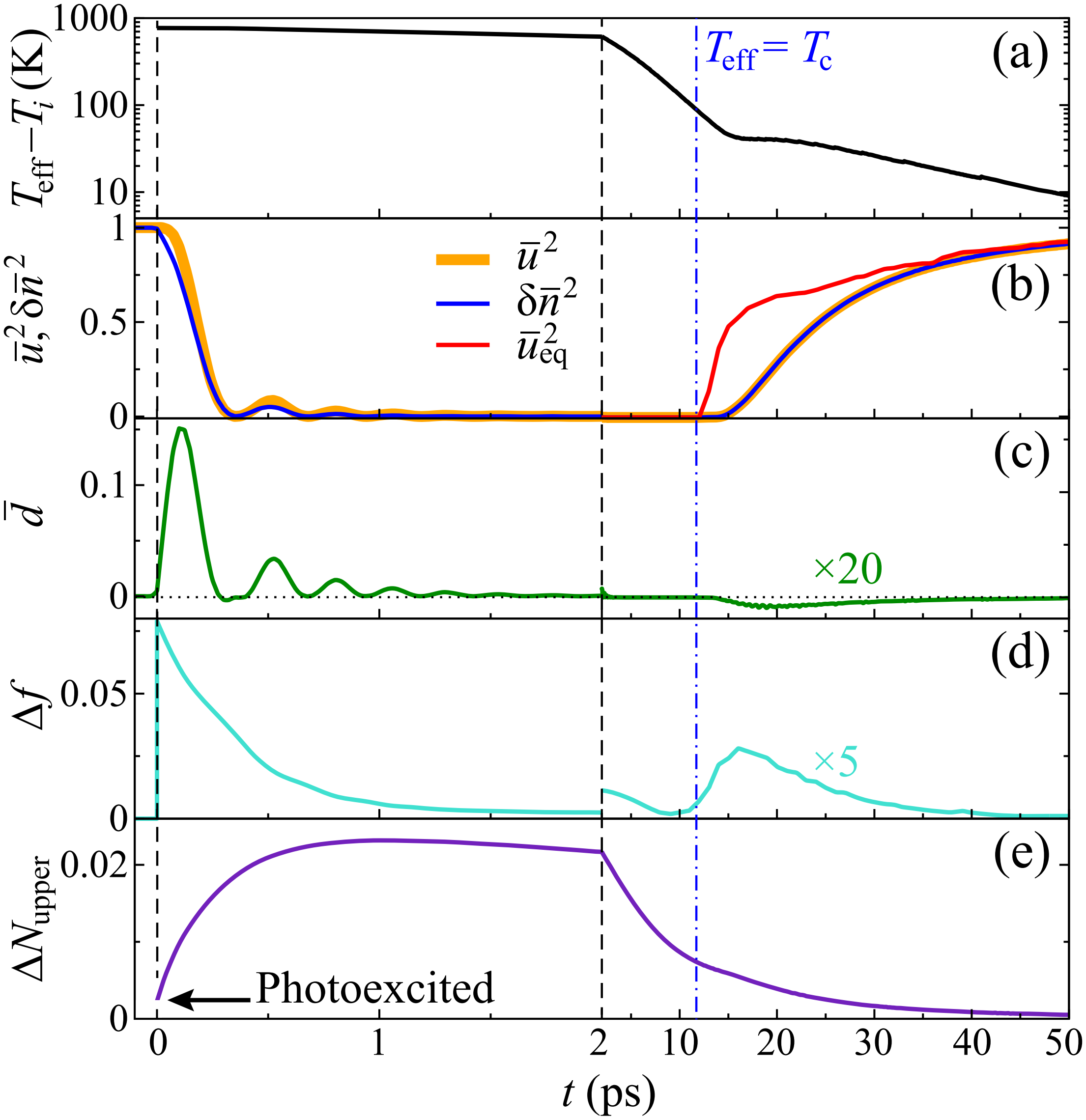

Figure 2.5 Nonequilibrium dynamics for $E_{\mathrm{photon}} \gg \Delta_{\mathrm{gap}}$ and $F = 4.38$ meV/site $> F_c$, the critical fluence for photoinduced insulator-metal transition. The time scales up to 2 ps and between 2 ps and 50 ps are chosen differently to reveal features more clearly. (a) $T_{\mathrm{eff}} - T_i$, the difference between the effective temperature of the electron system defined by Eq. (2.18) and the initial temperature before the pump, (b) the square of periodic lattice distortion $\bar{u}^2$, the square of electronic order parameter $\delta\bar{n}^2$, and the square of equilibrium distortion $\bar{u}^2_{\mathrm{eq}}$ at $T_{\mathrm{eff}}(t)$, normalized to their values before the optical pump, (c) $\bar{d} = \bar{u}^2 - \delta\bar{n}^2$, which parameterizes the decoupling between the CO and the periodic lattice distortion, (d) Δf, the average deviation of the electron distribution function $f(\varepsilon)$ from the Fermi-Dirac distribution function $f_{\mathrm{FD}}(\varepsilon, T_{\mathrm{eff}})$, defined by Eq. (2.22), (e) $\Delta N_{\mathrm{upper}}$ defined by Eqs. (2.23) and (2.24), that is, the number of excess electrons per site in the upper band with respect to the equilibrium state before the optical pump. The horizontal arrow indicates the number of electrons excited by the optical pump. For clarity, $\bar{d}$ and Δf between 2 ps and 50 ps are multiplied by constant factors indicated in the figure. Adapted from Ref. [77].

to characterize the decoupling between the CO and periodic lattice distortion in nonequilibrium. Figure 2.5(b) shows that substantial electron-hole excitations near the gap created by the electron-electron scattering reduce the order parameter δn and initiate the coherent oscillation in u, which damps out by around 1 ps. The result further reveals a difference between $\bar{u}^2$ and $\delta\bar{n}^2$, up to approximately 15% at $t \approx 0.13$ ps, as shown more clearly for $\bar{d} = \bar{u}^2 - \delta\bar{n}^2$ in Figure 2.5(c), which indicates a partial decoupling of the electrons and lattice distortions. The O ion has about thirty thousand times greater mass than an electron, which results in lattice dynamics lagging behind the electron dynamics and $\bar{d} > 0$. The oscillation amplitude of the normalized lattice distortion is larger than that of the normalized electronic order parameter for the same reason. The average difference $\Delta f(t)$ between $f(\varepsilon, t)$ and $f_{\mathrm{FD}}(\varepsilon, T_{\mathrm{eff}}(t))$, calculated according to

$$\Delta f(t) = \sqrt{\int_{-\infty}^{\infty} \left[f(\varepsilon, t) - f_{\mathrm{FD}}(\varepsilon, T_{\mathrm{eff}}(t))\right]^2 D_e(\varepsilon, t) d\varepsilon}, \tag{2.22}$$

is shown in Figure 2.5(d), which indicates that the electronic state deviates substantially from the Fermi-Dirac distribution during the CO melting. To track the transfer of electrons between the upper and the lower bands, we calculate the number of electrons per site in the upper band at time t,

$$N_{\mathrm{upper}}(t) = \int_{0}^{\infty} f(\varepsilon, t) D_e(\varepsilon, t) d\varepsilon, \tag{2.23}$$

and find the change from the number before the optical pump,

$$\Delta N_{\mathrm{upper}}(t) = N_{\mathrm{upper}}(t) - N_{\mathrm{upper}}(t < 0), \tag{2.24}$$

shown in Figure 2.5(e). The number of photoexcited electrons in the upper band is 0.002 per site, as indicated by a horizontal arrow in Figure 2.5(e), while the number of electrons excited through the subsequent thermalization up to ~ 1 ps is 0.021 per site, an order of magnitude greater, because many *low* energy electrons are excited near the gap as photoexcited *high* energy electrons decay through the energy-conserving electron-electron scattering.

As the effective electron temperature T_{eff} drops below T_c around $t = 12$ ps, indicated by the vertical dot-dashed blue line in Figure 2.5, the electron system enters the stage of CO gap reopening, and loses the *internal* equilibrium up to approximately $t = 30$ ps. Figure 2.5(b) shows that the squares of electronic order parameter and periodic lattice distortion, $\delta\bar{n}^2$ and $\bar{u}^2$, increase from zero. The square of the normalized lattice distortion that the system would have, if the system is in the equilibrium state at T_{eff},

$$\bar{u}^2_{\text{eq}}(t) = \left[\frac{u_{\text{eq}}(T_{\text{eff}}(t))}{u_{\text{eq}}(T_i)}\right]^2, \tag{2.25}$$

is also shown in Figure 2.5(b) for $t > 2$ ps. The strong reduction of the normalized actual distortion $\bar{u}(t)$ compared to the normalized equilibrium distortion $\bar{u}_{\text{eq}}(t)$ clearly shows the effect of nonequilibrium dynamics. The electronic ordering precedes the lattice ordering again and therefore, $\bar{d} = \bar{u}^2 - \delta\bar{n}^2 < 0$ [Figure 2.5(c)]. Furthermore, rapid opening of the gap pushes electron and hole energies up, which causes a very slow decay of T_{eff} [Figure 2.5(a)], a substantial deviation of $f(\varepsilon)$ from $f_{\text{FD}}(\varepsilon)$ near the gap [Figure 2.4(b)], and enhanced Δf [Figure 2.5(d)]. We discuss this in more detail in Section 2.5.5.

Finally, the stage after around 30 ps is characterized as the thermal relaxation stage, because the electron system and the periodic lattice distortion gradually approach the initial state before the optical pump, while maintaining *internal* equilibrium between them.

To compare the photoinduced and thermodynamic CO-metal transitions, we calculate the thermodynamic CO melting energy $\Delta E^{\text{eq}}_{\text{tot}}(T_i)$ [$\Delta E^{\text{eq}}_{\text{el}+u}(T_i)$] for the whole system including [excluding] the phonon thermal reservoir according to

$$\Delta E^{\text{eq}}_{\text{tot}}(T_i) = E^{\text{eq}}_{\text{tot}}(T_c) - E^{\text{eq}}_{\text{tot}}(T_i), \tag{2.26}$$

$$\Delta E^{\text{eq}}_{\text{el}+u}(T_i) = E^{\text{eq}}_{\text{el}+u}(T_{\text{c}}) - E^{\text{eq}}_{\text{el}+u}(T_i), \tag{2.27}$$

where the thermodynamic energy for electrons and periodic lattice distortion is

$$E^{\text{eq}}_{\text{el}+u}(T) = \int_{-\infty}^{\infty} \varepsilon f_{\text{FD}}(\varepsilon, T) D_e(\varepsilon, u_{\text{eq}}(T)) d\varepsilon + K u^2_{\text{eq}}(T), \tag{2.28}$$

the energy for the phonon thermal reservoir is

$$E^{\text{eq}}_{\text{phonon}}(T) = \int_0^{\infty} \omega b_\omega(T) D_p(\omega) d\omega, \tag{2.29}$$

and the total thermodynamic energy is

$$E^{\text{eq}}_{\text{tot}}(T) = E^{\text{eq}}_{\text{el}+u}(T) + E^{\text{eq}}_{\text{phonon}}(T). \tag{2.30}$$

For ultrafast photoinduced transitions, there is insufficient time to heat the phonons, and $\Delta E^{\text{eq}}_{\text{el}+u}(T_i)$ is the more relevant melting energy.

The critical fluence F_c for the insulator-metal transition versus the initial temperature T_i before the pump for $E_{\text{photon}} \gg \Delta_{\text{gap}}$ is shown in blue dots in Figure. 2.6. To compare the photoinduced and thermodynamic insulator-metal transitions, we calculate the thermodynamic CO melting energy $\Delta E_{\text{tot}}(T_i)$ at temperature $T_i < T_c$ for the whole system including the phonon thermal reservoir according to

$$\Delta E_{\text{tot}}(T_i) = E_{\text{tot}}(T_c) - E_{\text{tot}}(T_i), \tag{2.31}$$

where

$$\begin{aligned} E_{\text{tot}}(T) &= \int_{-\infty}^{\infty} \varepsilon f_{\text{FD}}(\varepsilon, T) D_e(\varepsilon, u_{\text{eq}}(T)) d\varepsilon + K u^2_{\text{eq}}(T) \\ &+ \int_0^{\infty} \omega b_\omega(T) D_p(\omega) d\omega. \end{aligned} \tag{2.32}$$

The result shown in purple line in Figure 2.6 indicates that the energy required for the photoinduced phase transition $F_c(T_i)$ is substantially lower than the energy required for the thermodynamic phase transition $\Delta E_{\mathrm{tot}}(T_i)$ for the model system, because for the photoinduced transitions there is insufficient time to heat the incoherent phonons. We also find the thermodynamic melting energy *without* the incoherent phonons $\Delta E_{\mathrm{e}+u}(T_i)$ shown in orange line in Figure 2.6, by excluding the last term in Equation (2.32) and calculating the difference between T_c and T_i. The critical fluence $F_c(T_i)$ is greater than $\Delta E_{\mathrm{e}+u}(T_i)$, indicating that a part of the energy initially deposited to the electron system leaks to the phonon thermal reservoir before the high energy electron and hole pairs cascade down to the states near the gap and initiate the insulator-metal transition.

2.5.3 Nonequilibrium Dynamics Induced by Photons with $E_{\mathrm{photon}} = \Delta_{\mathrm{gap}}$

In this subchapter, the results of the simulations with $E_{\mathrm{photon}} = \Delta_{\mathrm{gap}}$ are presented, particularly before 1.5 ps when the dynamics shows a behavior different from the case of high photon energy $E_{\mathrm{photon}} \gg \Delta_{\mathrm{gap}}$. The dynamics of the square of the normalized distortion $\bar{u}^2$ and the square of the normalized order parameter $\delta\bar{n}^2$ are shown in Figures 2.7(c)-2.7(e) for three values of the fluence $F = 0.97$, 1.83, and 5.65 meV/site, all above the critical fluence $F_{\mathrm{c}} = 0.91$ meV/site. At $t = 0$, while $\bar{u}^2$ still decreases continuously, the electronic parameter $\delta\bar{n}^2$ jumps abruptly by the amount that increases with the fluence F. This jump in $\delta\bar{n}^2$ occurs because the electrons with energies right at the gap, which are relevant to the CO, are directly excited by the optical pump. Figure 2.7(e) shows that the electronic order virtually vanishes and remains close to zero for a high enough fluence with E_{photon} close to Δ_{gap}. The energy of the electrons and holes excited by the optical pump near the gap is strongly coupled to $\bar{u}$ and gives rise to oscillating effective electron temperature T_{eff}, as shown in Figure. 2.7(a) for $F = 0.97$ meV/site. With the low energy of the photoexcited electrons, the initial electron thermalization reduces $\Delta N_{\mathrm{upper}}$, as indicated in Figure 2.7(b), very different from $E_{\mathrm{photon}} \gg \Delta_{\mathrm{gap}}$ case shown in

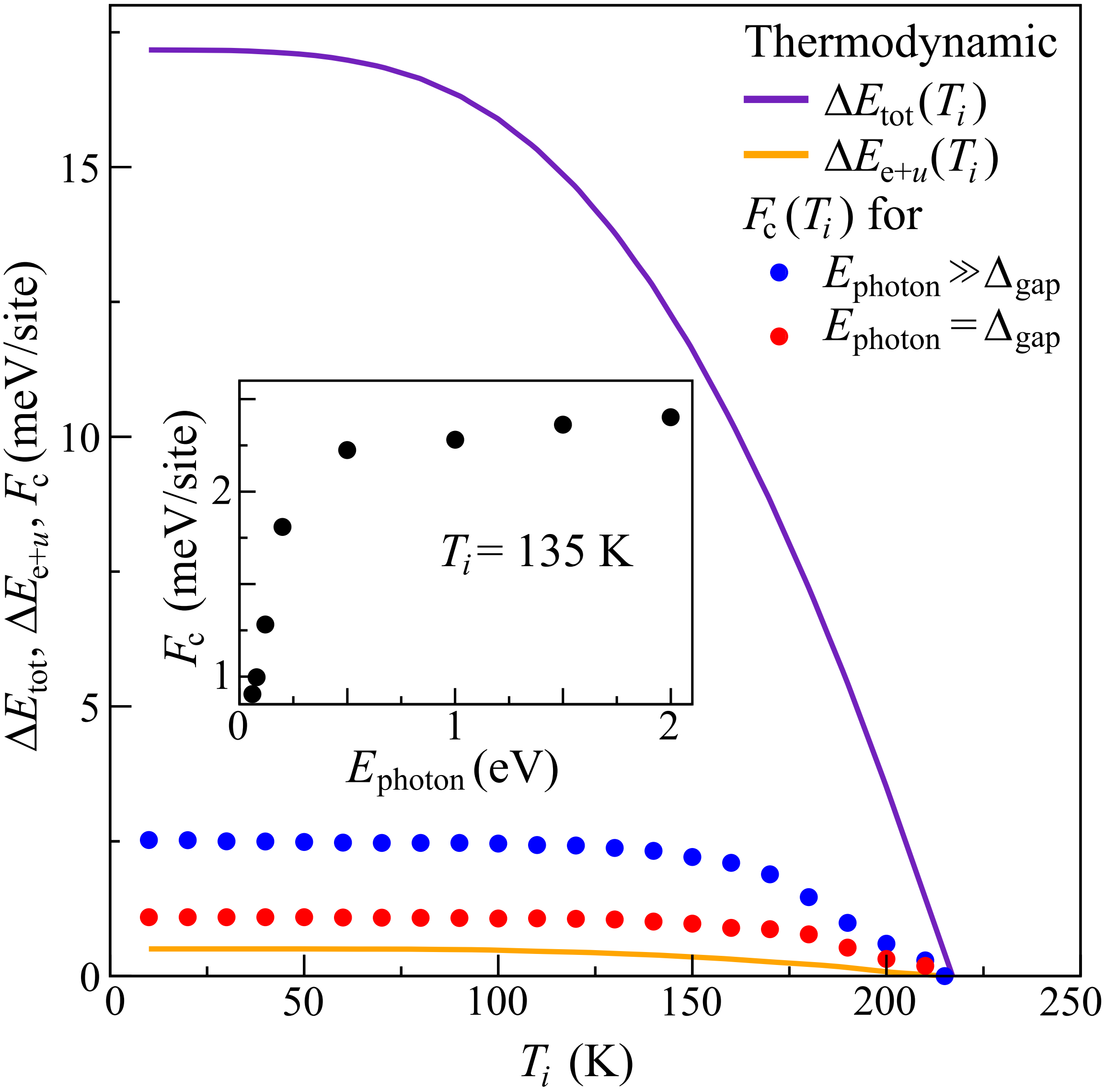

Figure 2.6 Comparison between the energies required for the thermodynamic and photoinduced insulator-metal transitions. The purple [orange] line represents the thermodynamic melting energy $\Delta E_{\mathrm{tot}}(T_i)$ [$\Delta E_{\mathrm{e}+u}(T_i)$] with [without] incoherent phonons, that is, the energy needed to thermodynamically heat the system including [excluding] incoherent phonons from T_i to T_c. The blue and red dots in the main panel represent the critical fluence $F_c(T_i)$ for the photoinduced insulator-metal transition by the pump beams with $E_{\mathrm{photon}} \gg \Delta_{\mathrm{gap}}$ and $E_{\mathrm{photon}} = \Delta_{\mathrm{gap}}$, respectively. The inset shows F_c versus E_{photon} at a fixed initial temperature $T_i = 135$ K. Adapted from Ref. [77].

Figure 2.5(e). Figures 2.7(c)-2.7(e) also show that the period of oscillation depends sensitively on time and the fluence, which will be analyzed in more detail in the next subchapter.

Red dots in Figure. 2.6 show the critical fluence F_c versus the initial temperature T_i for $E_{\text{photon}} = \Delta_{\text{gap}}$ and the inset in Figure. 2.6 displays F_c versus E_{photon} at $T_i =$ 135 K. As the photon energy decreases from $E_{\text{photon}} \gg \Delta_{\text{gap}}$ to $E_{\text{photon}} = \Delta_{\text{gap}}$, the critical fluence $F_c(T_i)$ reduces by about 60%, toward the thermodynamic melting energy $\Delta E_{\text{e}+u}(T_i)$ without incoherent phonons. The melting of the CO is greatly facilitated by exciting the electrons close to the gap, because photons in the optical pump directly alter the CO and more energy is used for the CO melting.

2.5.4 Dynamics of Energy Landscape and Coherent Oscillation Frequency

The energy landscape plays an important role in both thermodynamic and photoinduced phase transitions. We calculate the dynamic energy landscape $U(u,t)$ according to

$$U(u,t) = \frac{1}{N^2} \sum_{l\mathbf{k}} \varepsilon_{l\mathbf{k}}(u) f_{l\mathbf{k}}(t) + Ku^2, \tag{2.33}$$

where the first term, the electron energy summed over the occupation, represents the electron-lattice coupling, and the second term represents the vibrational potential energy from ion-ion interactions. In the first term, the electron distribution $f_{l\mathbf{k}}$ in the band and momentum indices is independent of the distortion u, because u is varied adiabatically. Strikingly different early-time energy landscape dynamics are found for different photon energies, as shown in Figure 2.8. Video simulations of $U(u,t)$ are provided in the supplementary material. Figures 2.8(a) and 2.8(c) display the results for $E_{\text{photon}} \gg \Delta_{\text{gap}}$. The energy landscape right after the optical pump at $t = 0$ [red line in Figure 2.8(a)] is close to a vertical shift of the energy landscape before the pump at $t < 0$ (black line), because the electronic excitations far away from the gap do not couple strongly to the periodic distortion u. Subsequently, the energy landscape

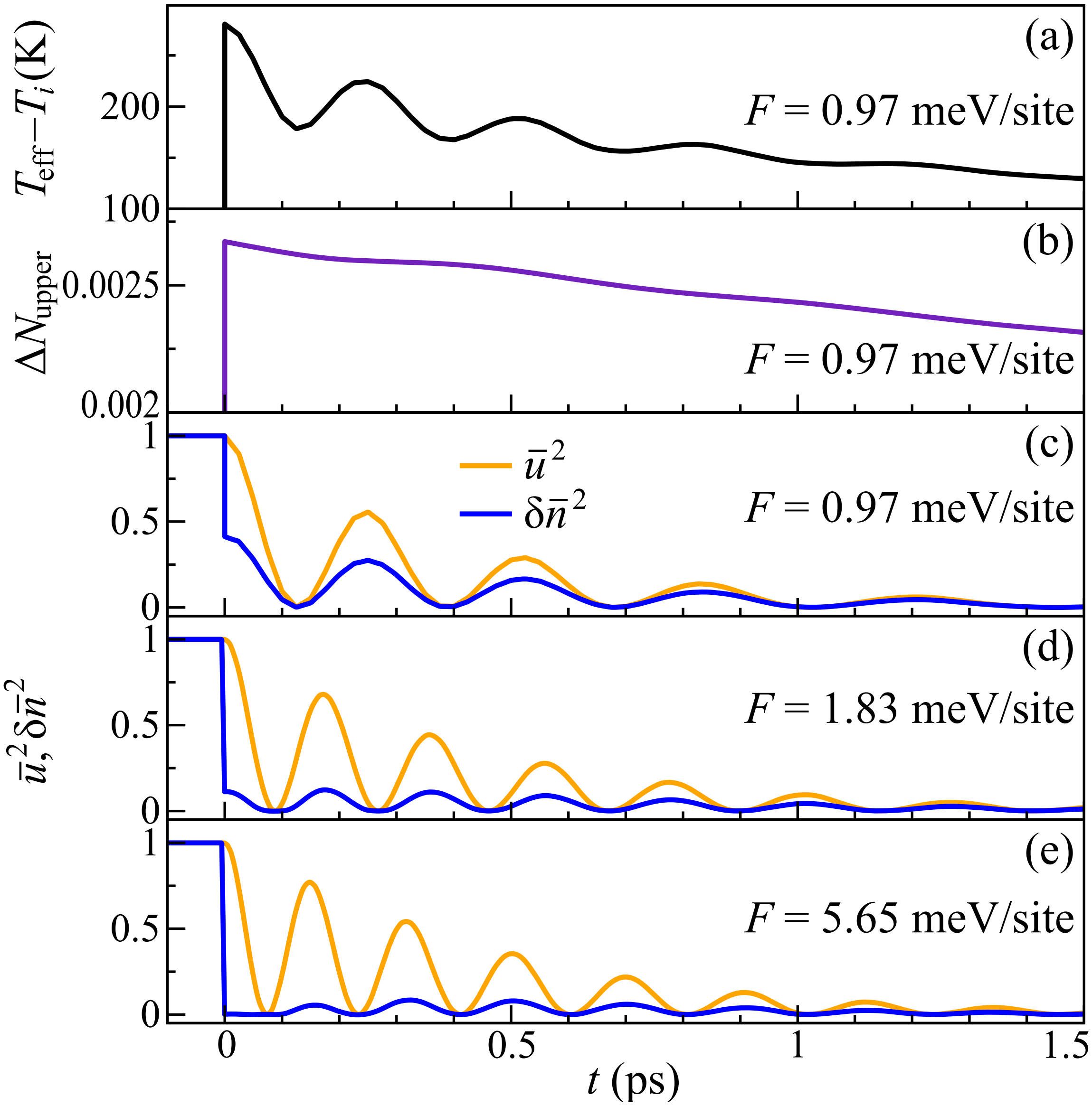

Figure 2.7 Nonequilibrium dynamics for $E_{\mathrm{photon}} = \Delta_{\mathrm{gap}}$. (a) The difference between the effective electron temperature T_{eff} and the initial temperature T_i before the pump. (b) $\Delta N_{\mathrm{upper}}$, the number of excess electrons in the upper band with respect to the equilibrium state before the pump. (c), (d), and (e): Normalized squares of the periodic lattice distortion and electronic order parameter, $\bar{u}^2$ and $\delta\bar{n}^2$, defined in Eq. (2.19) versus time t. The fluence of the pump beams are (c) $F = 0.97$ meV/site, (d) 1.83 meV/site, and (e) 5.65 meV/site, all above the critical fluence $F_c = 0.91$ meV/site. For (e), we use $W = 0.06$ eV as the width of the Gaussian peak in Eq. (2.17). Adapted from Ref. [77].

changes from a double-well (red and orange lines) to a single-well potential (green and cyan lines), and as the effective temperature T_{eff} drops below T_{c} the energy landscape becomes double-well again (dark blue and purple lines). Figure 2.8(c) shows the full energy landscape dynamics in U-u-t space, along with the dynamics of the distortion u. Energy landscape changes from a double-well to a single-well during the first oscillation in u, resulting in a slow first oscillation, as discussed in more detail later in this subchapter.

The energy landscape dynamics for the $E_{\mathrm{photon}} = \Delta_{\mathrm{gap}}$ case in Figures 2.8(b) and 2.8(d) show a behavior very different from the $E_{\mathrm{photon}} \gg \Delta_{\mathrm{gap}}$ case, particularly during $t < 3$ ps. With the CO state directly destroyed by the optical pump, the energy landscape right after the optical pump [red line in Figure 2.8(b)] already has a metallic single-well potential. Comparison between $E_{\mathrm{photon}} \gg \Delta_{\mathrm{gap}}$ case and $E_{\mathrm{photon}} = \Delta_{\mathrm{gap}}$ case in Figure 2.8 reveals that, when the pump energy is tuned at the gap, the change in the shape of the energy landscape occurs in the time scale of the pump pulse width, resulting in much faster and more energy efficient melting of the CO phase, which could be important in using such phenomena for ultrafast switching devices.

The energy landscape dynamics for the $E_{\mathrm{photon}} = \Delta_{\mathrm{gap}}$ case in Figure 2.9 shows a behavior very different from the $E_{\mathrm{photon}} \gg \Delta_{\mathrm{gap}}$ case in Figure 2.8, particularly during $t < 3$ ps. Figures 2.9(a) and 2.9(b) display the dynamics of the energy landscape for the pump fluence F above and below the critical fluence respectively, with Figure 2.9(a) corresponding to the case shown in Figure 2.7(a). With the CDW state directly destroyed by the optical pump for Figure 2.9(a), the energy landscape right after the optical pump (red line) already has a metallic single-well potential. The harmonic coefficient of this energy landscape right after the optical pump increases with the pump fluence F, consistent with the photoinduced stiffening of the phonon mode coupled to the CDW [red dots in Figure. 2.10(b)] and the Kohn anomaly [blue

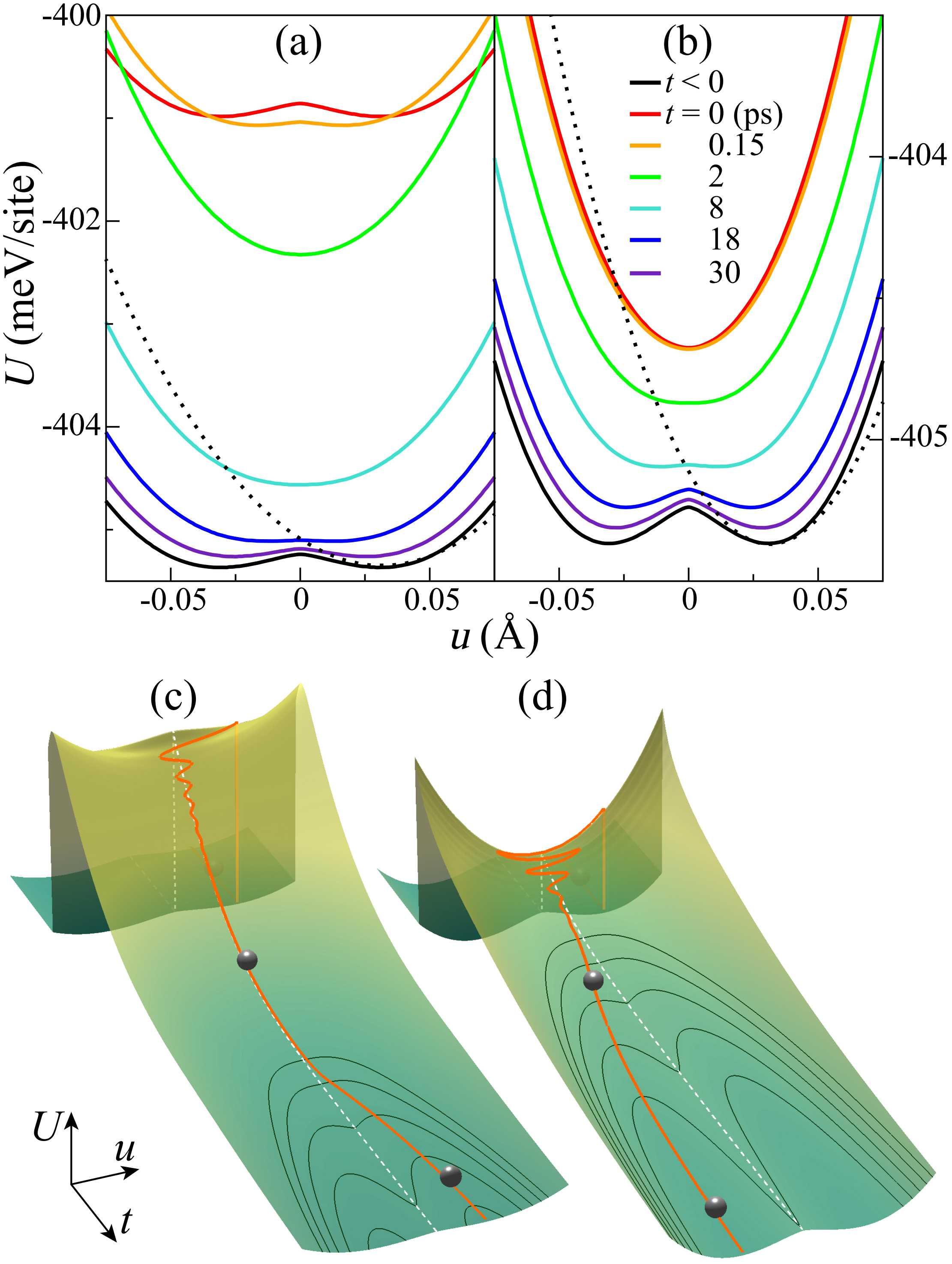

Figure 2.8 Energy landscape dynamics initiated by the optical pump with $E_{\text{photon}} = 2$ eV $\gg \Delta_{\text{gap}}$ and $F = 4.38$ meV/site for (a) and (c), and with $E_{\text{photon}} = \Delta_{\text{gap}}$ and $F = 0.97$ meV/site for (b) and (d). In (a) and (b), the dotted black lines represent the harmonic energy near the equilibrium distortion before the optical pump. In (c) and (d), the orange and green lines represent $u(t)$ and equal-energy lines respectively, with the axis ranges of -5 ps $< t <$ 25 ps and -0.06 Å $< u <$ 0.06 Å. Adapted from Ref. [77].

dots in Figure 2.3]. Even for the case of $F < F_\mathrm{c}$ shown in Figure 2.9(b), the energy landscape right after the optical pump (red line) is not a simple vertical shift of that before the pump (black line), but becomes shallower with the minimum distortion closer to zero because the energy landscape is strongly tied to the states near the gap. Comparison between Figures 2.8 and 2.9 reveals that, when the pump energy is tuned at the CDW gap, the change in the shape of the energy landscape occurs in the time scale of the pump pulse width, resulting in much faster and more efficient melting of the CDW phase, which could be important in using such phenomena for ultrafast switching devices.

Energy landscape dynamics can be experimentally observed through the time-dependent frequency of coherent oscillations. To analyze the correlation between the energy landscape and the frequency of the oscillation for the model, we first find the angular frequency $\Omega = \pi/(t_{n+1} - t_n)$ versus time $t = (t_{n+1} + t_n)/2$, where t_n is the time for the n-th local maximum of $\bar{u}^2(t)$. Figure 2.10(a) displays the results for two cases of $E_\mathrm{photon} = \Delta_\mathrm{gap}$ [cases of Figures 2.7(c) and 2.7(d)] and two cases of $E_\mathrm{photon} \gg \Delta_\mathrm{gap}$ (including the case in Figure 2.5). For comparison, Figure 2.10 also shows the bare angular frequency Ω_bare without electron-lattice coupling and the equilibrium angular frequency Ω_eq for the equilibrium double-well potential before the pump [see dotted black lines in Figures 2.8(a) and 2.8(b)]. The results reflect the rapidly changing energy landscape, as the excited electrons and holes redistribute in ways that depend on the photon energy and the fluence. For $E_\mathrm{photon} = \Delta_\mathrm{gap}$ shown in red symbols in Figure 2.10(a), instantaneous melting of CO leads to Ω either close to or higher than Ω_eq right after the optical pump, depending on whether $F \approx F_c$ or $F \gg F_c$. When the energy landscape is about to change from a single-well to a double-well around 2 ps, the energy landscape becomes highly anharmonic with the flat bottom of potential well [see the curve for $t = 2$ ps in Figure 2.8(b)], reflected in a small $\Omega < \Omega_\mathrm{eq}$ around 2 ps in Figure 2.10(a). In contrast, for $E_\mathrm{photon} \gg \Delta_\mathrm{gap}$ shown in blue

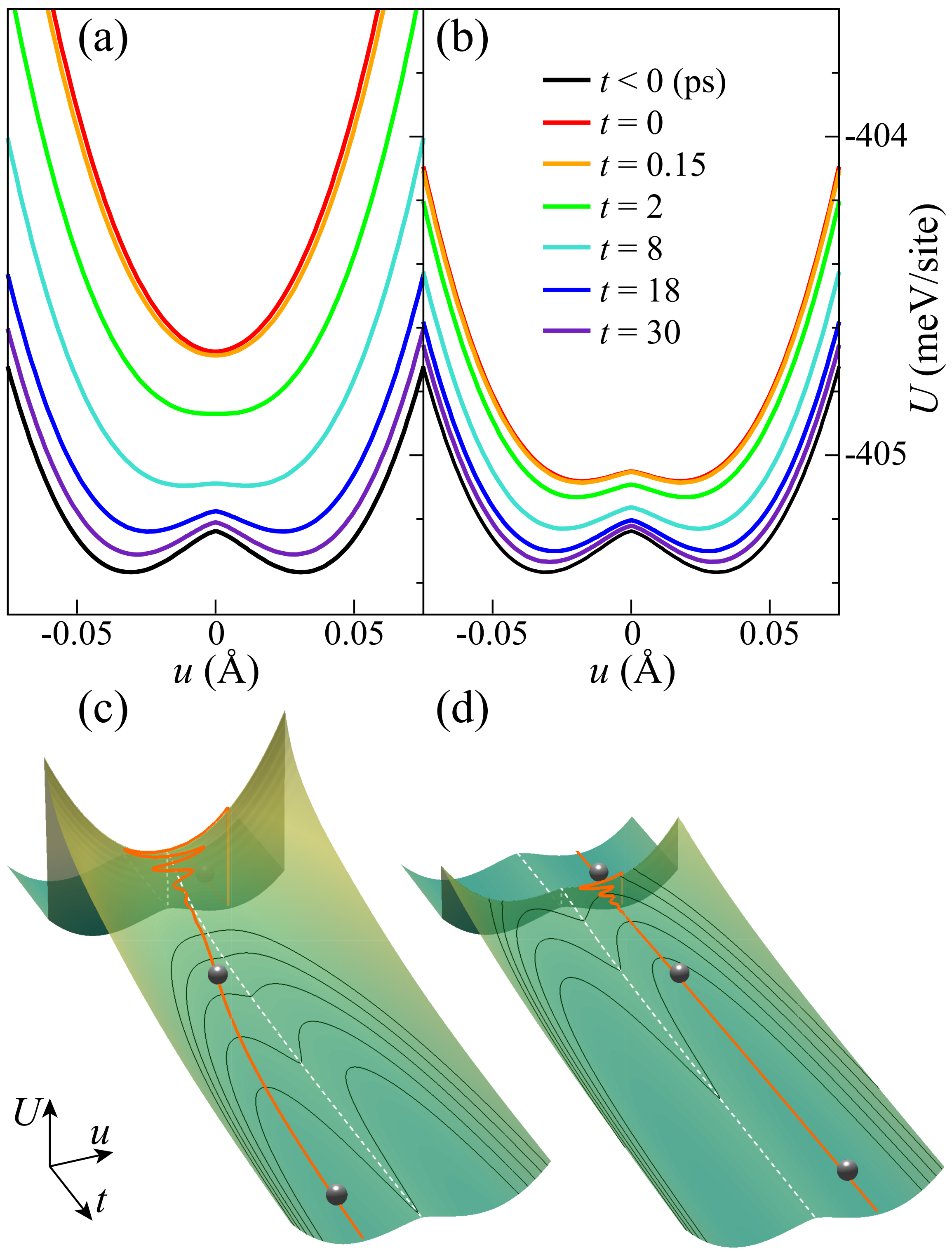

Figure 2.9 (Color online) Energy landscape dynamics initiated by the optical pump with $E_{\mathrm{photon}} = \Delta_{\mathrm{gap}}$ for (a) the fluence $F = 0.96$ meV/site, above F_{c}, and for (b) $F = 0.32$ meV/site, below F_{c}. Corresponding plots in U-u-t space are shown in (c) and (d). See the caption for Figure 2.8. Adapted and modified from Ref. [77]

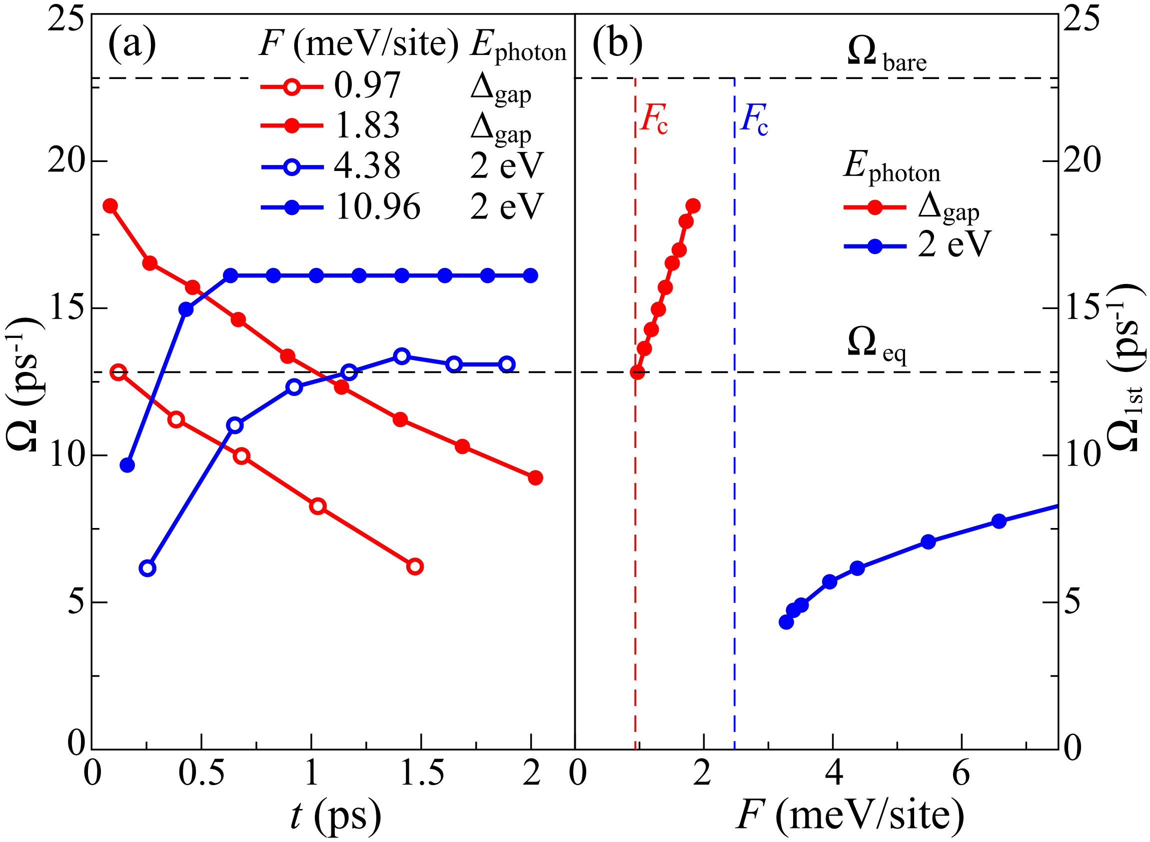

Figure 2.10 (a) Angular frequency of coherent oscillation Ω versus time t, (b) the first angular frequency $\Omega_{1\mathrm{st}}$ from the first half-oscillation versus the fluence of the optical pump F for $E_{\mathrm{photon}} = \Delta_{\mathrm{gap}}$ and $E_{\mathrm{photon}} = 2$ eV $\gg \Delta_{\mathrm{gap}}$. Lines connecting symbols are guides for eyes. The horizontal dashed black lines represents the bare angular frequency $\Omega_{\mathrm{bare}} = \sqrt{K/m}$ without electron-lattice coupling and the equilibrium angular frequency Ω_{eq} before the optical pump. The vertical dashed red and blue lines in (b) indicate the critical fluence F_c for $E_{\mathrm{photon}} = \Delta_{\mathrm{gap}}$ and 2 eV, respectively. Adapted from Ref. [77].

symbols in Figure 2.10(a), the situation is reversed. The energy landscape starts out with a double-well that turns into a single-well, reflected in a small $\Omega < \Omega_{\mathrm{eq}}$ right after the pump. The angular frequency Ω increases after melting of CO and remains almost constant for $t = 1 \sim 2$ ps because the energy landscape remains single-well till much later $t \approx 12$ ps.

From the first half-oscillation we take the initial angular frequency $\Omega_{1\mathrm{st}}$ and plot with respect to the fluence F in Figure 2.10(b) for $E_{\mathrm{photon}} = \Delta_{\mathrm{gap}}$ and $E_{\mathrm{photon}} = 2$ eV $\gg \Delta_{\mathrm{gap}}$. The corresponding critical fluences F_c are also shown in vertical dashed lines.

Much faster increase in $\Omega_{1\text{st}}$ with the fluence for $E_{\text{photon}} = \Delta_{\text{gap}}$ reflects the dominant effect of the states near the gap on the energy landscape. Transient stiffening of the phonon mode by the optical pump has been identified in a CDW phase of CeTe_3 (Reference. [29]), and is consistent with the Kohn anomaly, [27, 71] that is a softening of the phonon mode responsible for the CO or CDW when approaching T_c from above.

2.5.5 Nonthermal Electron Distribution and Electron Energy Relaxation

Nonthermal electron distribution could give rise to dynamic behaviors significantly different from the predictions of models based on thermal electron distribution, such as the absence of divergent electron relaxation time at low temperatures in metals that contradicts the prediction from the two-temperature model. [25, 26, 1, 8, 35] In this subchapter, we discuss the character and the origin of the nonthermal electron distribution during the photoinduced insulator-metal transition and the reopening of the gap. The high photon energy case shown in Figures 2.4 and 2.5 is analysed as a specific example.

The distribution function $f(\varepsilon, t = 0)$ right after the optical pump and the equilibrium Fermi-Dirac distribution function $f_{\text{FD}}(\varepsilon, T_{\text{eff}}(t = 0))$ with the same energy are schematically drawn in Figure 2.11(a). Two typical electron-electron scattering processes that would change $f(\varepsilon, t = 0)$ closer to $f_{\text{FD}}(\varepsilon, T_{\text{eff}}(t = 0))$ are also shown in green and blue arrows in Figure 2.11(a), which indicates the net electron transfer from the lower to the upper band responsible for the rapid rise of ΔN_{upper} during the first 1 ps [Figure 2.5(e)].

The reopening of the CO gap results in another stage with nonthermal electron distribution [Figure 2.5(d)]. As shown in Figure 2.4(b) for $t = 18$ ps, the difference between the actual distribution and the thermal distribution is largest near the gap. Figure 2.11(b) explains schematically why this happens. The distortion u affects energy levels near the gap most sensitively. Adiabatic opening of the gap pushes

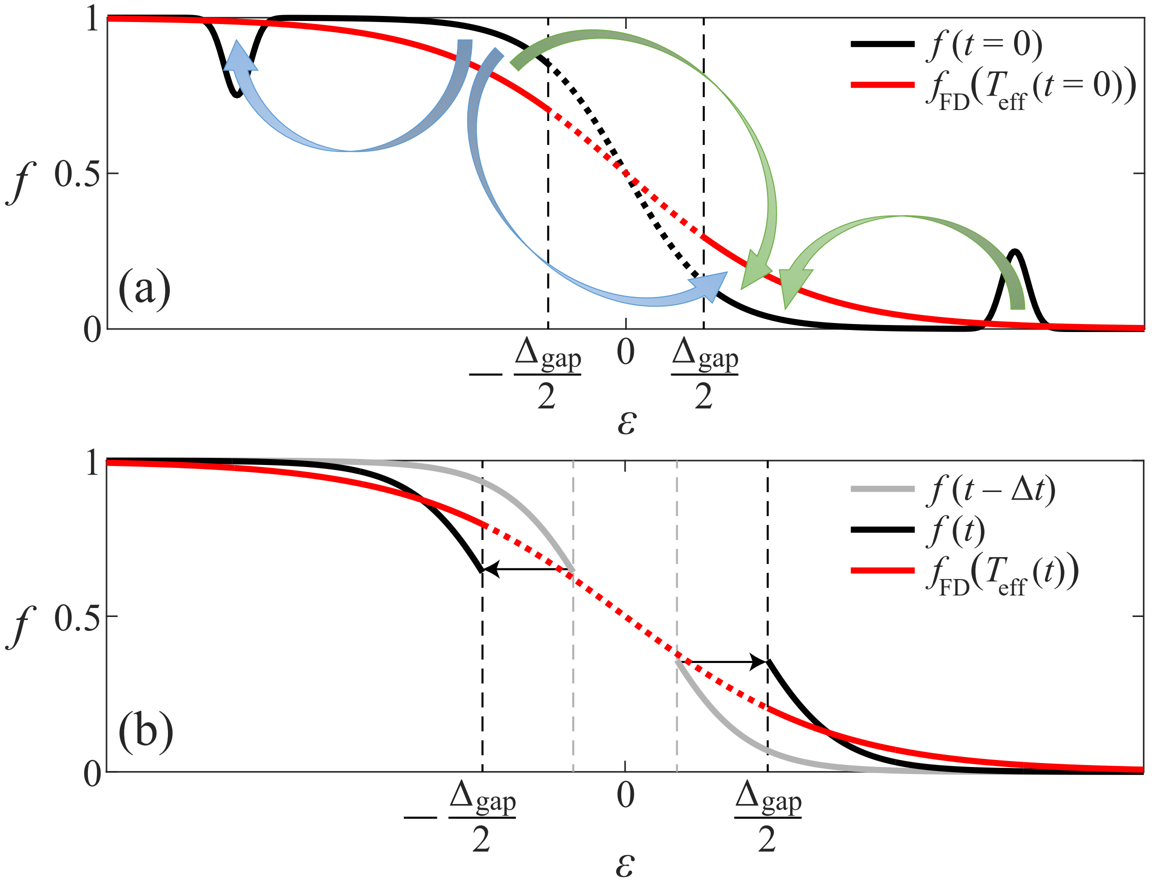

Figure 2.11 (a) Schematic diagram showing electron transfer from the lower to the upper band through two typical electron-electron scattering processes (blue and green arrows) right after the optical pump with $E_{\mathrm{photon}} \gg \Delta_{\mathrm{gap}}$. The black and the red lines represent the actual electron distribution and the corresponding Fermi-Dirac distribution, respectively. (b) Schematic diagram showing the effects of the gap reopening on f_ε. The gray line shows the actual distribution one time step Δt earlier. The black and the red lines represent the actual and the Fermi-Dirac distributions. Adapted from Ref. [77].

electron and hole energy levels up without changing the occupation $f_{l\mathbf{k}}$ of the state $|l\mathbf{k}\rangle$, as indicated by arrows in Figure 2.11(b). This shift contributes to the increase of the effective temperature T_{eff} and competes against the cooling by the phonon thermal reservoir, which gives rise to a particularly slow electron energy relaxation of exponential decay rate $r \approx 0.013$ ps^{-1}. [Figure 2.5(a)].

The dynamics of the CO gap plays an essential role for the relaxation of the electronic energy shown in Figure 2.5(a) in two aspects. First, the size of the CO gap directly affects the energy transfer from the electron to the phonon system, because phonons with energy smaller than the CO gap cannot participate in electron energy decay across the gap, limiting the thermal conductivity between the electron and the phonon system. This explains the order-of-magnitude increase of the relaxation time at the onset of the CO gap reopening. Second, the reopening of the CO gap pushes up the energy of the excited electrons and holes adiabatically, competing against the cooling of the electron system by the phonon thermal reservoir. The rapid increase of the CO gap makes the energy relaxation particularly slow right after T_{eff} drops below T_c.

2.6 Comparison with Experiments

We make comparisons between our results and experimental data. The photon energy of 1.55 eV used to melt CO in Reference [12] corresponds to the CO gap energy in $Pr_{0.5}Ca_{0.5}MnO_3$, and, therefore, the experimental results can be compared with our results for $E_{\text{photon}} = \Delta_{\text{gap}}$. Approximately, the normalized off-resonance structural superlattice peak intensity and the normalized on-resonance charge order peak intensity in Figure. 2 in Reference [12] correspond to $\bar{u}^2$ and $\delta\bar{n}^2$ in our model. Large oscillation of the structural superlattice peak intensity and almost complete suppression of the CO peak intensity in the experiments are consistent with the evolution of $\bar{u}^2$ and $\delta\bar{n}^2$ shown in Figure 2.7(e) for $E_{\text{photon}} = \Delta_{\text{gap}}$ case for our model.

Experimentally, unlike our simulation results, the energy for the photoinduced transition is not necessarily smaller than the energy for the thermodynamic transition. [12, 30, 65] It has been proposed that the observed high critical fluence is related to the long wavelength distortions, or the changes in unit cell symmetry present in these materials, which cannot fully relax during the short time scale of photoinduced phase transitions. This discrepancy between simulation results and experimental results indicates that the long wavelength distortions, which are not included in the model, may indeed play an important role in the increase of the critical fluence, competing against the opposite effect from transient decoupling of incoherent phonons.

Increased energy efficiency of the photoinduced phase transition with a lower E_{photon} found from the simulations (Figure 2.6) has been also observed in experiments. For example, in the CDW phases of $1T$-TaS_2 (Reference [30]) and VO_2 (Reference [65]), as E_{photon} is reduced from 1.5 eV to 0.5 eV, the energy required for the photoinduced transition drops by about 75% and 50% respectively, which are comparable to about 60% drop of the critical fluence between $E_{\text{photon}} \gg \Delta_{\text{gap}}$ and $E_{\text{photon}} = \Delta_{\text{gap}}$ cases in the simulations.

2.7 Summary

In summary, we have simulated photoinduced melting of charge order using a model of $M\text{O}_2$ square lattice and a phonon thermal reservoir. The stages of CO melting, CO gap reopening, and thermal relaxation have been identified. During the stage of CO melting, the dynamics of the periodic lattice distortion is partially decoupled from and lags behind the dynamics of electronic order parameter due to large inertia of ions. As the effective electron temperature T_{eff} drops below T_c, electron system enters the stage of CO gap reopening and its state changes from thermal to nonthermal.

The dynamics during the first few ps after the optical pump has been found to be sensitively dependent on the photon energy of the optical pump. For the photon energy much greater than the CO gap, the dynamics of the lattice distortion lags behind the dynamics of the electronic CO order parameter during the first few ps due to the large mass of the ions. For large enough fluences, the CDW phase melts and refreezes as the phonon thermal reservoir cools the initially hot electron system. During around 12 – 25 ps in the simulations, the reopening of the CO gap reduces the electron-phonon scattering channels, hinders the electron transfer from the upper to the lower band, slows down electron energy relaxation, and gives rise to a nonthermal electron distribution. Even for fluences too small to melt the CO phase, we have found qualitatively similar nonequilibrium phenomena as large fluence cases. Because the initial excitation occurs far away from the CO gap, the energy landscape shifts vertically along the energy axis without changing the double-well potential shape at the moment of the optical pump, which becomes shallower and a single-well potential, if the fluence is large enough, and eventually falls back to the original energy landscape.

For the photon energy tuned at the CO gap, the CO order parameter is suppressed immediately due to the direct modification of the CO by the photons, followed by much slower lattice dynamics. The frequency of the coherent oscillation shows a strong dependence on time. The simulations have further shown an increase of the oscillation frequency with the fluence due to the partial decoupling between the electrons and the lattice distortion. Because the initial excitation occurs right at the CO gap, the shape of the energy landscape changes in the time scale of the pump pulse width, for example, into a single-well potential for a large enough fluence.

For our model system, which does not include long wavelength lattice distortions, it has also been found that the critical fluence for the photoinduced CO-metal transition is smaller than the energy required to melt the CO thermodynamically, because only the electron system and a particular mode of the lattice distortion are primarily involved without much involvement of incoherent phonons with a large specific heat. In particular, the critical fluence decreases, making photoinduced transitions more energy efficient, as the photon energy is lowered. If the photon energy is tuned at the CO gap, almost all energy given to the electron system by the optical pump is used to melt the CO, leading to a critical fluence very close to the energy needed to heat just electrons and the periodic lattice distortion to T_c.

The results have shown intricately coupled dynamics of electrons, periodic lattice distortions, and incoherent phonons in nonequilibrium states excited by the optical pump in CO materials. Our approach can be extended in various ways, in particular by including more basis states in the tight-binding Hamiltonian. Inclusion of multiple orbitals would allow the study of the dynamics of orbital ordering in addition to the dynamics of charge ordering, as found in Reference. [12]. Adding spin degrees of freedom and on-site Coulomb interaction [52] would allow the simulations of dynamics of magnetic ordering found in some CO or CDW materials. The study of such extended models would shed insight on how to make ultrafast switching devices out of CO or CDW materials.

2.8 Supplementary Material

See supplementary material for video simulations of the dynamics of electron distribution function $f(\varepsilon)$ together with the energy landscape $U(u)$ for $E_{\text{photon}} \gg \Delta_{\text{gap}}$ and $E_{\text{photon}} = \Delta_{\text{gap}}$ cases.

[`ftp://ftp.aip.org/epaps/journ_appl_phys/E-JAPIAU-123-022812`]

CHAPTER 3

ELECTRONIC PROPERTIES OF STRUCTURAL TEXTURES IN MODEL TOPOLOGICAL INSULATOR WITH TOPOLOGY-STRUCTURE COUPLING

The work in this chapter was done in collaboration with Prof. Emil Prodan, from Department of Physics at Yeshiva University, and Prof. Keun Hyuk Ahn from Department of Physics at New Jersey Institute of Technology.

3.1 Introduction

Research on topological materials has been rapidly progressed over the past decade. [39, 31, 40] One of the oldest models of topological insulator is the one-dimensional (1D) Su-Schrieffer-Heeger (SSH) model [10, 49, 41], for which zero energy states could be present at the open edges or at the antiphase boundaries due to topological reasons. Depending on the sign of distortions, 1D SSH system could be either a topological or a regular insulator, which can be called 'topology-structure coupling'. For two-dimensional (2D) or three dimensional (3D) cases, more interesting structural textures are possible, for example, twin and antiphase boundaries and their mixtures. [4, 7] In this dissertation work, we investigate topologically protected zero energy states within structural textures for model 2D insulator with topology-structure coupling. We analyze electronic properties of twin boundaries (TB) and antiphase boundaries (APB) and their mixtures, using both numerical and topological approaches. We propose an experiment that can realize our results in meta-materials.

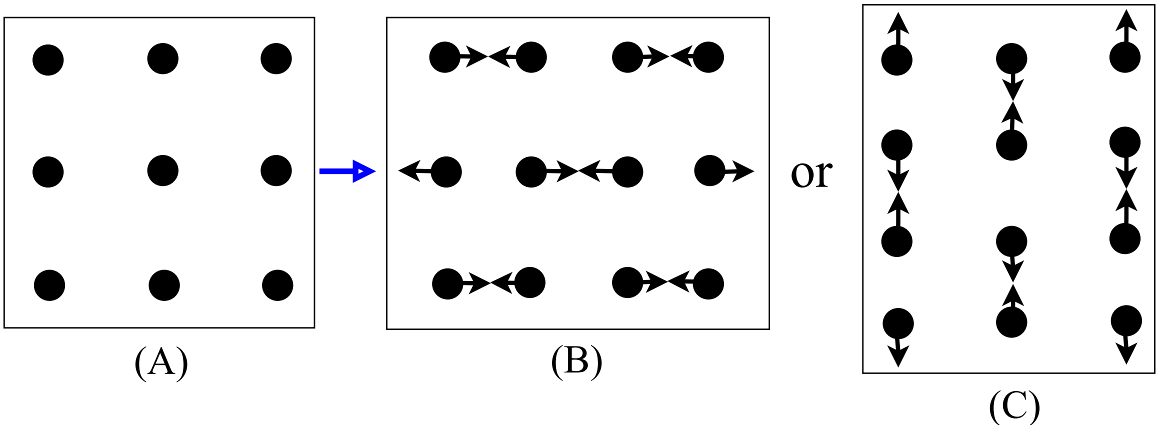

Figure 3.1 (a) 2D square lattice; (b) Vertical rectangle with x-distortion; (c) Horizontal rectangle with y-distortion.

3.2 Model

3.2.1 Model 2D structure

As a model structure, we consider a 2D structure with a uniform and staggered distortion shown in Figure 3.1. Starting from a square lattice, a rectangular uniform distortion is considered, on top of which a staggered distortion with a wave vector (π, π) is superimposed either along y axis for horizontal rectangle or along x axis for vertical rectangle. Change of the phase for the staggered distortion gives rise to antiphase boundaries, while the change of orientation for uniform rectangular distortion gives rise to twin boundaries. More complicated structural textures can also arise by mixing antiphase and twin boundaries in various patterns. For convenience, we introduce two different ways of indexing atoms. For the lattice distortions, $\mathbf{i} = (i_x, i_y)$ designates the atom originally at (i_x, i_y) in the square lattice, with x and y axes chosen along the nearest neighbors. For electronic properties, which will be discussed in the next subchapter, a two-atom unit cell is chosen with the unit cell index $\mathbf{n} = (n_1, n_2)$, which represents the unit cell at $n_1\mathbf{a}_1 + n_2\mathbf{a}_2$ ($\mathbf{a}_1$, $\mathbf{a}_2$: primitive vectors). Two atoms in the unit cell are represented by atom A and B.

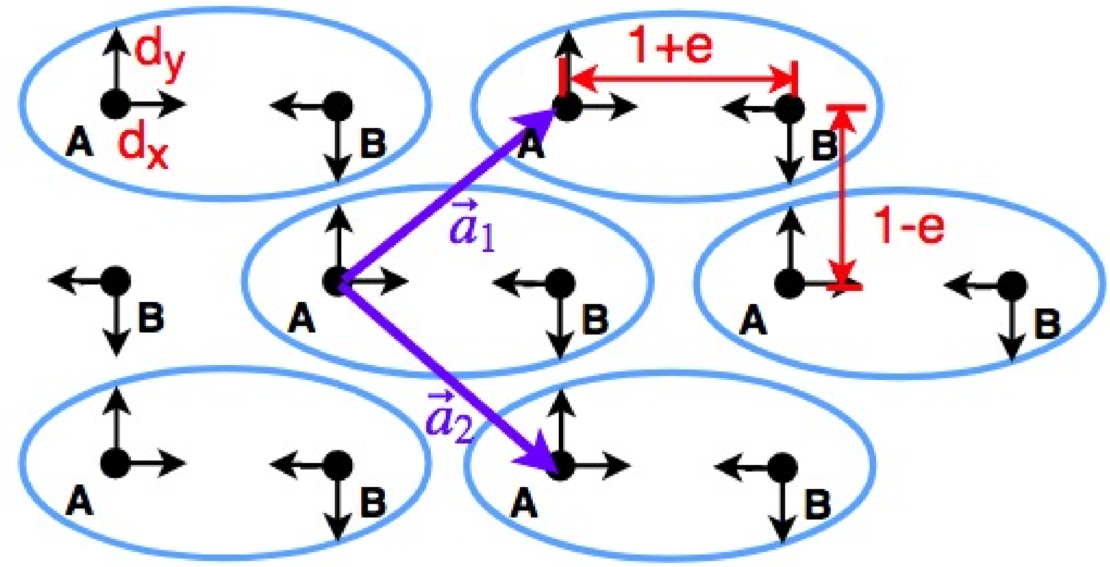

Figure 3.2 The model system of an AB_2 square lattice with periodic boundary conditions. Arrows show the displacements, represented by d_x and d_y in different directions. $1+e$ and $1-e$ represent the distance between neighbor A and B sites, in vertical and horizontal direction, respectively. The displacement parameters, d_x and d_y represent the displacement of A ion in unit cell at $0 \cdot \vec{a}_1 + 0 \cdot \vec{a}_2$.

3.2.2 Electron Hamiltonian, Chirality, and Band Structure for Uniform States

In this subchapter, we present the electronic Hamiltonian for distorted lattice without antiphase or twin boundaries. To include both distorted configurations of Figure 3.1(b) and 3.1(c) in a single Hamiltonian, we consider the distortions shown in Figure 3.2, in which e and d_x $[d_y]$ parameterize uniform and staggered distortion along x $[y]$ direction. To be specific, we choose unit cell and primitive vectors, $\mathbf{a}_1$ and $\mathbf{a}_2$, as shown in Figure 3.2, which is suitable for the analysis of 135° or 45° direction APB/TB/open edge as explained further in the next subchapter. By assuming one spinless electron state at each site and electron hopping that linearly depends on inter-atomic distance, we obtain the following Hamiltonian, in which hopping amplitude for undistorted lattice and the linear coefficient of hopping amplitude versus distance are chosen as 1 and -1, respectively.

$$\begin{aligned} H = \sum_{\mathbf{n}} & - & (1-e+2d_x)C^\dagger_{\mathbf{n},\mathrm{A}}C_{\mathbf{n},\mathrm{B}} + \mathrm{H.c.} \\ & - & (1-e-2d_x)C^\dagger_{\mathbf{n},\mathrm{B}}C_{\mathbf{n}+(1,1),\mathrm{A}} + \mathrm{H.c.} \\ & - & (1+e+2d_y)C^\dagger_{\mathbf{n},\mathrm{A}}C_{\mathbf{n}+(-1,0),\mathrm{B}} + \mathrm{H.c.} \\ & - & (1+e-2d_y)C^\dagger_{\mathbf{n},\mathrm{B}}C_{\mathbf{n}+(0,1),\mathrm{A}} + \mathrm{H.c.} \end{aligned} \tag{3.1}$$

By Fourier transformation to k-space, we obtain

$$H = \sum_{\mathbf{k}} \begin{pmatrix} C^\dagger_{\mathbf{k},\mathrm{A}} \\ C^\dagger_{\mathbf{k},\mathrm{B}} \end{pmatrix}^T \begin{pmatrix} 0 & h(k_1,k_2) \\ h^*(k_1,k_2) & 0 \end{pmatrix} \begin{pmatrix} C_{\mathbf{k},\mathrm{A}} \\ C_{\mathbf{k},\mathrm{B}} \end{pmatrix} \tag{3.2}$$

where

$$\begin{aligned} h(k_1,k_2) = & - & (1-e+2d_x) - (1-e-2d_x)e^{-i(k_1+k_2)} \\ & - & (1+e+2d_y)e^{-ik_1} - (1+e-2d_y)e^{-ik_2} \end{aligned} \tag{3.3}$$

The Hamiltonian is chiral with respect to the Pauli matrix σ_3, that is,

$$\sigma_3 H(k_1,k_2)\sigma_3 = -H(k_1,k_2), \tag{3.4}$$

which indicates that the system could have non-trival topological properties in insulating phase.

The band structure is given by

$$\varepsilon_{l\mathbf{k}}(k_1,k_2) = (-1)^l \left| h(k_1,k_2) \right| \tag{3.5}$$

with the first Brillouin zone $\Omega_{1\mathrm{BZ}} = \{\mathbf{k}| -\pi < k_1 \leq \pi, -\pi < k_2 \leq \pi\}$ and $l = 0,1$ For $d_y = 0[d_x = 0]$, we obtain a metal-insulator phase diagram in $e - d_x[(-e) - d_y]$ plane shown in Figure 3.3, where insulating phase arises when $e < 0, d_x \neq 0[e > 0, d_y \neq 0]$. This indicates a possible topological insulator phase and zero-energy gap states, similar to graphene or 1D SSH model.

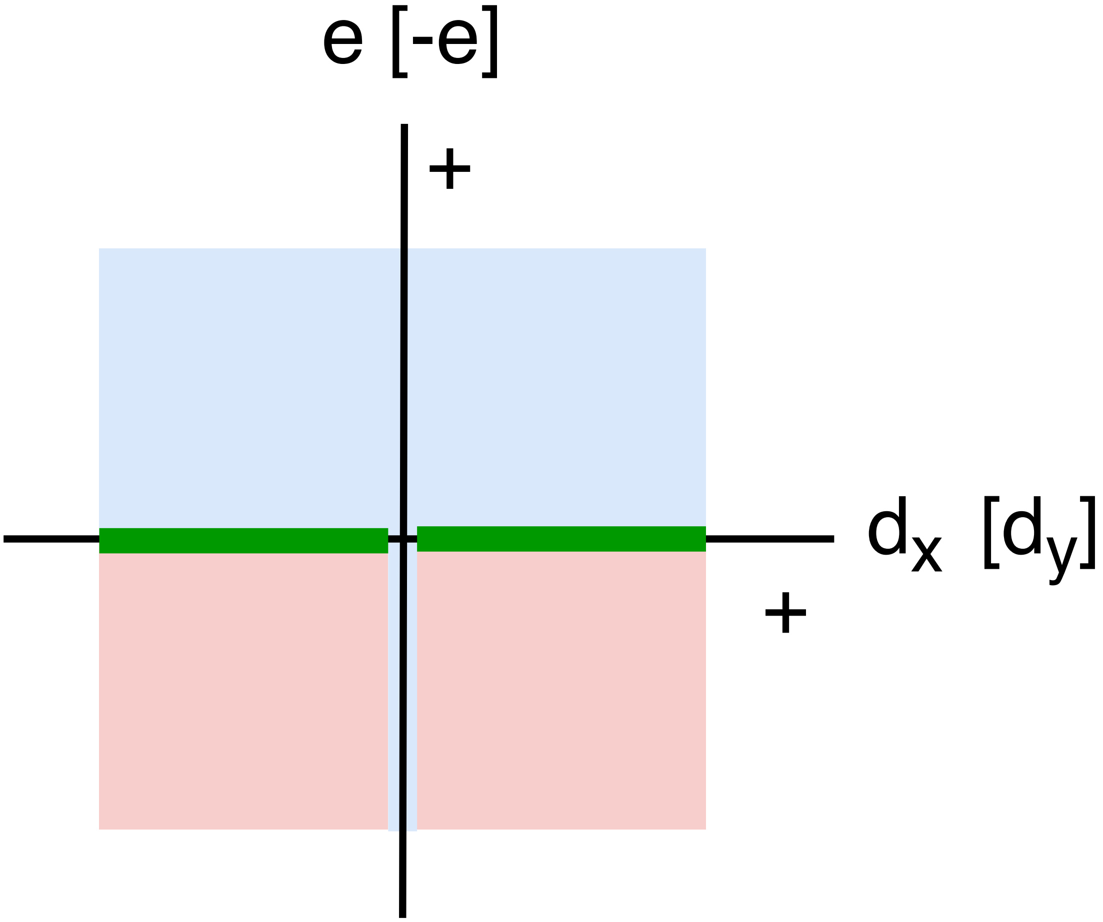

Figure 3.3 The phase diagram for the system.Red regions are the insulator phase, blue regions are the metal phase. dark green line is the semi-metal phase.

Table 3.1 Winding Number ν for Figure. 3.2

e_3	$\tilde{s}_x$	$\tilde{s}_y$	ν
$+$	0	$+$	0
$+$	0	$-$	-1
$-$	$+$	0	0
$-$	$-$	0	-1

3.2.3 Winding Number ν and Topology

With the chiral symmetry, the Hamiltonian is of type III A in the classification of topology. The Chern number is zero, but winding number could be non-zero. For the topological analysis of antiphase/twin/edge states, the unit cell and primitive vectors should be chosen as follows. First, APB, TB, and open edges should not cut through the unit cell. Second, one of the primitive vectors, for example $\mathbf{a}_2$ in Figure 3.2 for 135° boundaries, should be parallel to the direction of APB, TB, and open edges. With such choices, the winding number ν is defined as:

$$\nu = \frac{1}{2\pi i} \int_0^{2\pi} dk_2 \frac{\partial}{\partial k_2} \ln h(k_1, k_2) \tag{3.6}$$

which depend on the direction of antiphase/twin/edge boundaries.

The choice of unit cell and primitive vectors in Figure 3.2 is suitable for the analysis of APB/TB/open edge along 135° direction. The calculated winding number ν's for four possible degenerate distorted states in Figure 3.1 are shown in Table 3.1. It reveals that winding number depends on the sign of e_3 and $\tilde{s}_x$, $\tilde{s}_y$, which indicates the possibility of zero energy gap states for certain TB/APB/open edge along 135° direction, as discussed in more detail later.

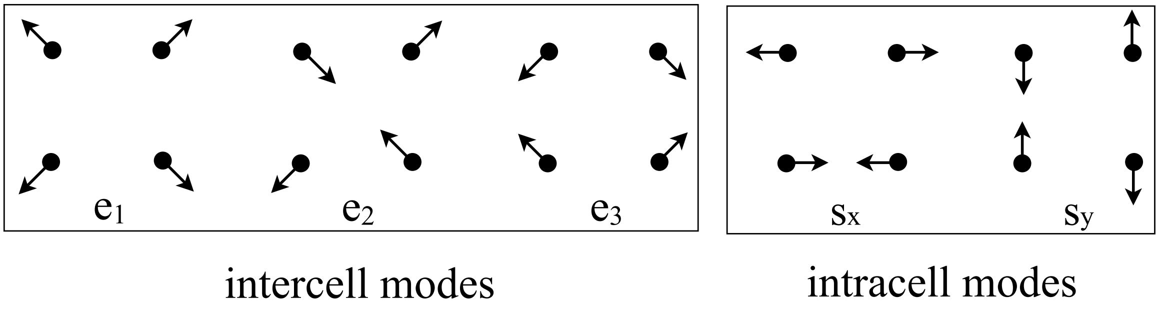

Figure 3.4 Atomic scale distortion modes for a square lattice. [7] Signs of d_x and d_y are the same with the signs of $\tilde{s}_x$ & $\tilde{s}_y$. Sign of e coincides with sign of e_3.

3.2.4 Lattice Energy for Relaxed Structural Textures

Lattice distortion field should satisfy the compatibility, that is, the bonds between atoms should not be broken or overlap with each other. Further, abrupt charge of distortion is likely to cost a lot of lattice energy. Therefore, gradual change of distortion field would be more realistic. To take both effects into account, structural textures are obtained by relaxing an energy expression E_{lattice}, written in terms of modes that represent the lattice distortions. Specifically, distortion of square lattice can be expressed in terms of five distortion modes, e_1, e_2, e_3, s_x, and s_y, shown in Figure 3.4, as proposed by Ahn et al. [4, 7, 3, 2]

We further define $\tilde{s}_x$ and $\tilde{s}_y$:

$$\begin{aligned} \tilde{s}_x(i_x, i_y) &= (-1)^{i_x+i_y} s_x(i_x, i_y) \\ \tilde{s}_y(i_x, i_y) &= (-1)^{i_x+i_y} s_y(i_x, i_y) \end{aligned} \tag{3.7}$$

The simplest energy expression E_{lattice}, which gives rise to the states in Figure. 3.1 as ground states, is as follows.

$$E_{\text{lattice}} = E_s + E_l + E_c, \tag{3.8}$$

$$E_s = \sum_{\mathbf{n}} \left[\frac{B}{2}(s_x^2 + s_y^2) + \frac{G_1}{4}(s_x^4 + s_y^4) + \frac{G_2}{2}s_x^2 s_y^2)\right]_{\mathbf{n}} \tag{3.9}$$

$$E_l = \sum_{\mathbf{n}} \left[\frac{A_1}{2}e_1^2 + \frac{A_2}{2}e_2^2 + \frac{A_3}{2}e_3^2\right]_{\mathbf{n}} \tag{3.10}$$

$$E_c = \sum_{\mathbf{n}} \left[C_3(s_x^2 - s_y^2)e_3\right]_{\mathbf{n}} \tag{3.11}$$

where E_s is the energy for short-wavelength modes includes all symmertry-allowed terms up to the fourth order. E_l represents the energy for long-wavelength modes, and E_c represents the coupling between the long- and short-wavelength modes.[7]

With $e_1 = e_2 = 0$ and $e_3 = -C_3(s_x^2 - s_y^2)/A_3$, we find the expression of minimum total energy per site for the homogeneous state. [7]

$$\begin{aligned} \frac{E_{\text{tot}}^{\text{h,min}}}{N^2} &= \frac{B}{2}(s_x^2 + s_y^2) + \frac{1}{4}(G_1 - \frac{2C_3^2}{A_3})(s_x^4 + s_y^4) \\ &+ \frac{1}{2}(G_2 + \frac{2C_3^2}{A_3})s_x^2 s_y^2. \end{aligned} \tag{3.12}$$

With $B < 0$, $G_1 - \frac{2C_3^2}{A_3} > 0$, $G_2 + \frac{2C_3^2}{A_3} > 0$, and $G_2 + \frac{2C_3^2}{A_3} > G_1 - \frac{2C_3^2}{A_3}$, the global minimum occurs at $s_x = \pm s_0$, $s_y = 0$ and $s_x = 0$, $s_y = \pm s_0$, where $s_0 = \sqrt{\frac{-B}{G_1 - \frac{2C_3^2}{A_3}}}$. We choose the parameters $A_1 = 7$, $A_2 = 4$, $A_3 = 6$, $B = -5$, $C_3 = 20$, $G_1 = 180$, $G_2 = 100$, which satisfy such conditions.

3.3 Results

In this chapter, we present the results obtained by both numerical method and topological analysis for various antiphase and twin boundaries and their mixed structural textures.

3.3.1 Antiphase boundaries along 135°

First, we consider the APB along 135° for $e_3 < 0$, which is obtained by relaxing appropriately chosen initial state of lattice distortion. The distortion pattern is schematically shown in Figure 3.5. As mentioned earlier, the unit cell and the primitive vectors are chosen as identical to those in Figure 3.2. With $e_3 < 0$, $\tilde{s}_x < 0$, $\tilde{s}_y = 0$ for the bottom left domain and $e_3 < 0$, $\tilde{s}_x > 0$, $\tilde{s}_y = 0$ for the top right domain in Figure 3.5, the winding number ν is -1 and 0, respectively [see Table 3.1], and the antiphase boundaries separates domains of different winding numbers. Therefore, zero energy states are expected within APB when APBs are separated by infinite distance. By solving electronic Hamiltonian numerically, we obtain band structure $\varepsilon_m(k_1)$ for a lattice with 32×32 unit cells and periodic boundary condition. The results are shown in Figure 3.6, in which the APB states and bulk states are marked. As expected, bulk band has a gap. The energies of APB states approach zero, as the system size increases, consistent with the topological analysis. Real space plot of APB states further show that these states are localized on A-site for one APB and on B-site for the other APB, which we also prove analytically.

Winding number in Table 3.1 indicate that APB along 135° between $e_3 > 0$, $\tilde{s}_y < 0$, $\tilde{s}_x = 0$ domain and $e_3 > 0$, $\tilde{s}_y > 0$, $\tilde{s}_x = 0$ would also host zero energy APB states, because the winding numbers are $\nu = 0$ and $\nu = -1$, respectively. From symmetry, APB along 45° would also host zero energy APB states.

3.3.2 Antiphase Boundaries Along 90° and 0°

Next, we consider APB along 90° and 0°. Because 90° line would cut through unit cell in Figure 3.2, a different unit cell and primitive vectors should be chosen for 90° APB/open edges, as shown in Figure 3.7. Table 3.2 shows winding number ν calculated for different cases of degenerate ground states in Figure. 3.1. Relaxed APB structure is obtained using E_{lattice}. An example of APB between two domains

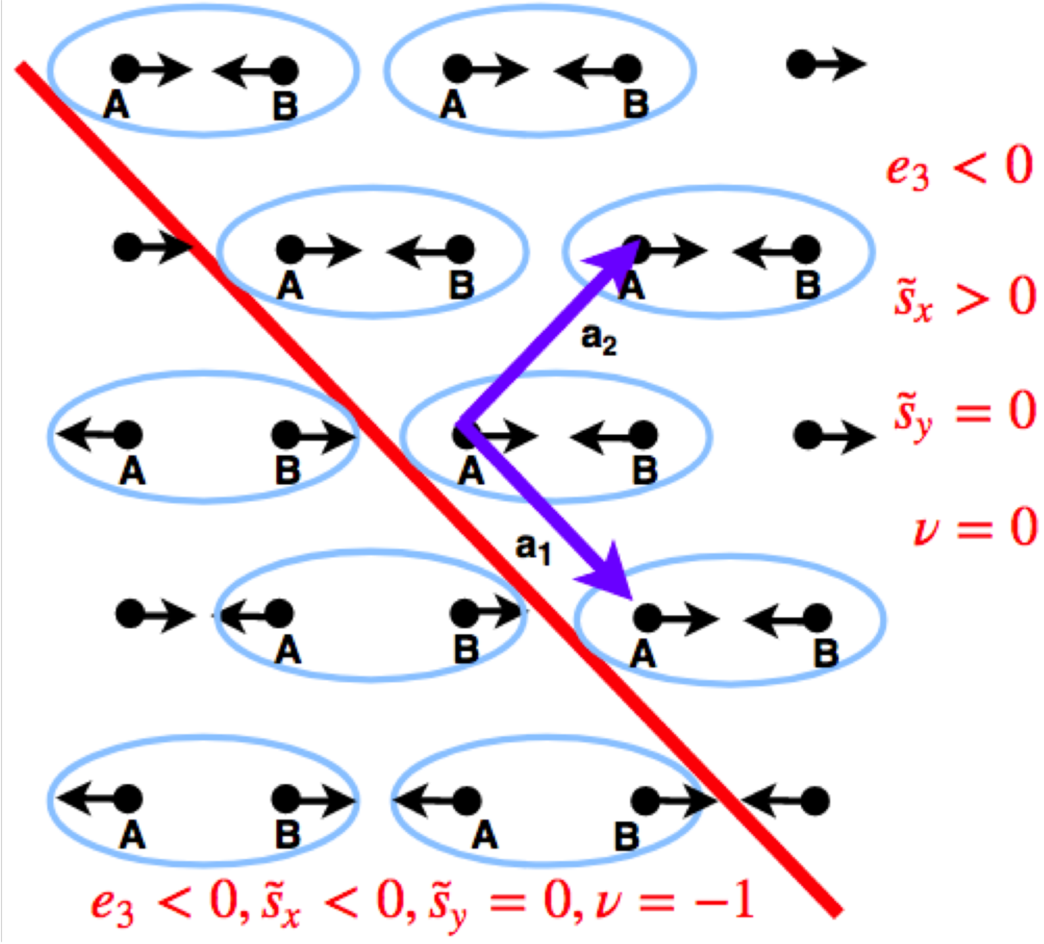

Figure 3.5 APB along 135°. Red line shows the APB, and blue circles show the unit cell.

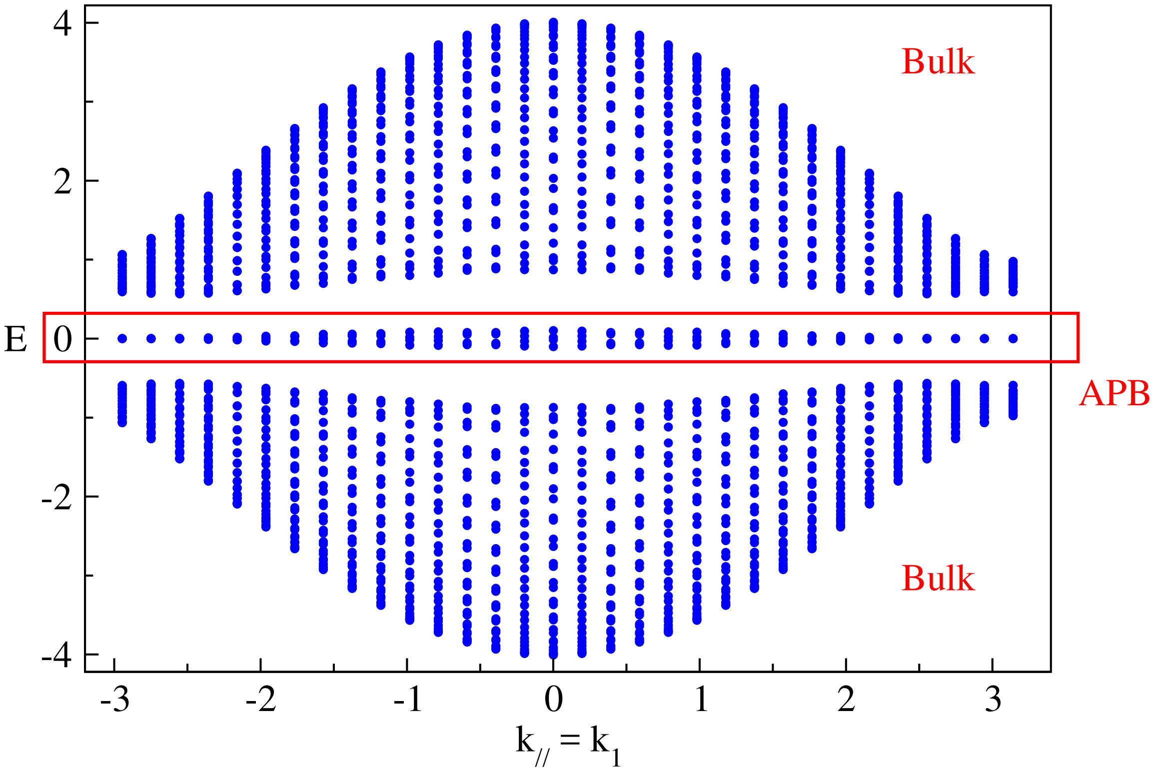

Figure 3.6 Band structure for APB along 135° with the relaxed distortion.

with $e_3 < 0,\ \tilde{s}_x > 0,\ \tilde{s}_y = 0$ and $e_3 < 0,\ \tilde{s}_x < 0,\ \tilde{s}_y = 0$ is shown schematically in Figure 3.7. The two domains have different winding number, as indicated in Table 3.2. Therefore, zero energy states are expected within APB. Numerical results of the band structure $\varepsilon_m(k_1)$ shown in Figure 3.9(a) are consistent with the topological analysis.

Table 3.2 further indicates that while 90° APB between $e_3 > 0,\ \tilde{s}_x \neq 0,\ \tilde{s}_y = 0$ domains host zero energy gap states, 90° APB between $e_3 > 0,\ \tilde{s}_x = 0,\ \tilde{s}_y \neq 0$ domains have the same winding number ν and would not host zero energy states.

We further study 0° APB between $\tilde{s}_x > 0$ and $\tilde{s}_x < 0$ domains with $e_3 < 0$ and $\tilde{s}_y = 0$. The lattice distortion is again obtained by relaxing E_{lattice} from an appropriately chosen initial lattice distortion, and is schematically shown in Figure 3.8. 90° rotation of 0° APB in Figure 3.8 corresponds 90° APB with $e_3 > 0$, $\tilde{s}_y \neq 0,\ \tilde{s}_x = 0$ listed in Table 3.2, and therefore, the domains would have the same

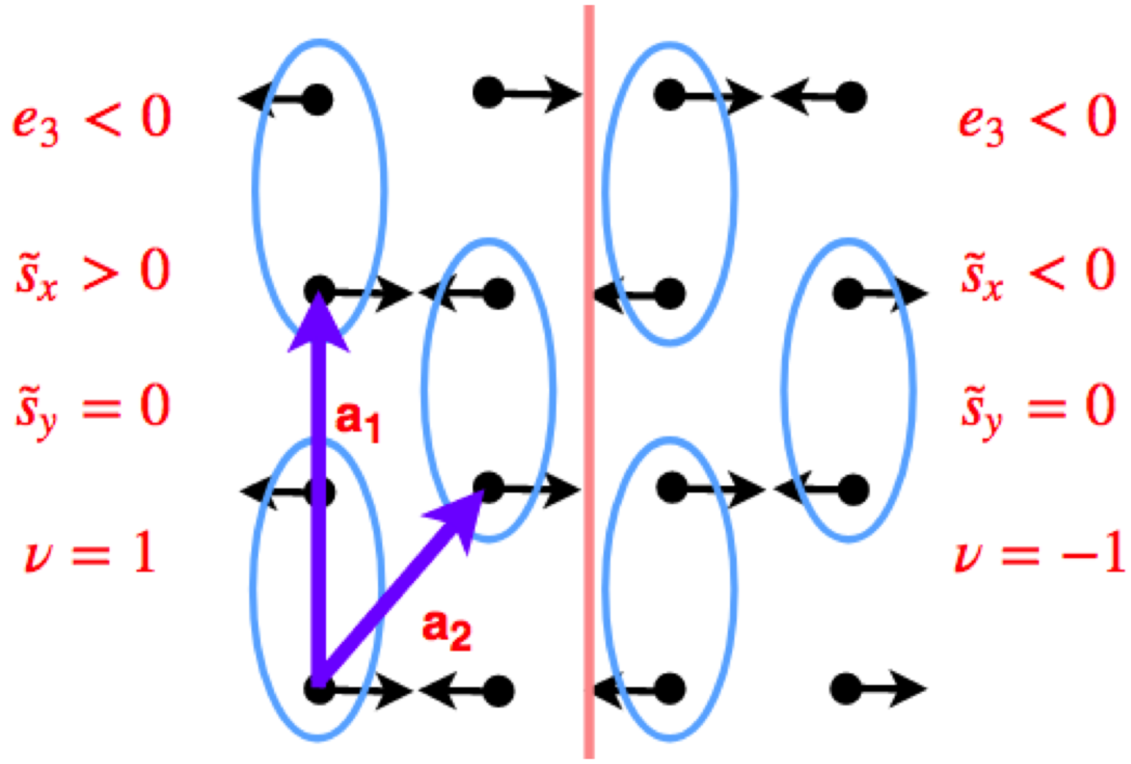

Figure 3.7 When APB parallel y-axis, circle show the way how to choose unit cell.

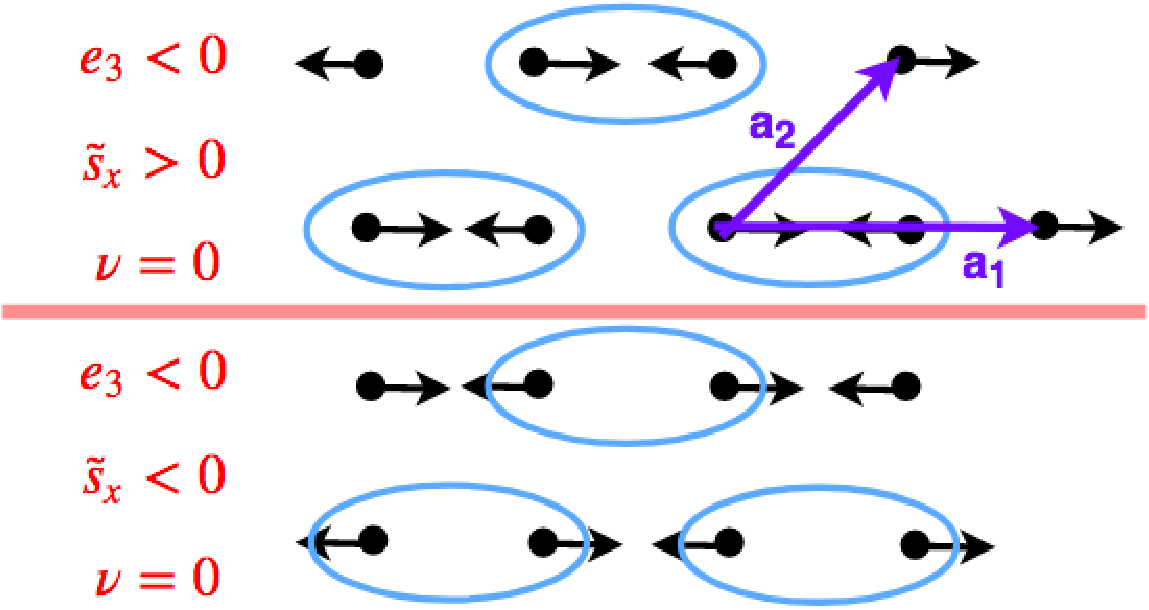

Figure 3.8 When APB parallel x-axis, circle show the way how to choose unit cell.

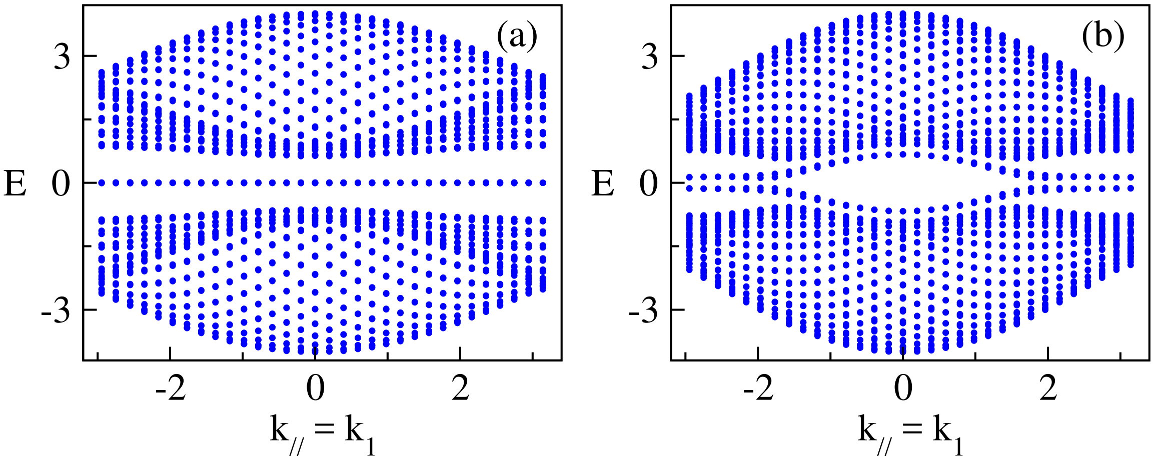

Figure 3.9 (a) Band structure for APB at 90° in Figure 3.7; (b) Band structure for APB at 0° in Figure 3.8 .

Table 3.2 Winding Number ν that Applied to 90° Boundaries in Figure. 3.7

e_3	$\tilde{s}_x$	$\tilde{s}_y$	ν
$+$	0	$+$	0
$+$	0	$-$	0
$-$	$+$	0	1
$-$	$-$	0	-1

Table 3.3 Winding Number ν for Figure. 3.8

e_3	$\tilde{s}_x$	$\tilde{s}_y$	ν
$+$	0	$+$	1
$+$	0	$-$	-1
$-$	$+$	0	0
$-$	$-$	0	0

winding number and zero energy states are not expected. The topological analysis is consistent with the band structure $\varepsilon_m(k_1)$ in Figure 3.9(b), which shows no zero energy states. Winding numbers for the unit cell and primitive vectors in Figure 3.8 are listed in Table 3.3.

3.3.3 Twin Boundaried Along 135°

We also study electronic properties of twin boundaries. First, it is well known that TB along either 45° or 135° direction has a lower elastic energy cost at the TB. Therefore, we focus on TB along 135°. Both Figures 3.10 and 3.11, show a domain with $e_3 < 0$ at the lower left corner and a domain with $e_3 > 0$ at the upper right corner, separated by 135° TB. The difference is the relative sign of $\tilde{s}_x$ and $\tilde{s}_y$. In Figure 3.10, $\tilde{s}_x$ and $\tilde{s}_y$ have the same sign, for example, $\tilde{s}_x > 0$ and $\tilde{s}_y > 0$ for the two domains, as indicated in Figure 3.10. In this case, relaxation of the lattice energy E_{lattice}, leads to the TB structure as schematically shown in Figure 3.10, for which the center of TB profile is at the center of the bonds. In contrast, $\tilde{s}_x$ and $\tilde{s}_y$ have the opposite signs $\tilde{s}_x > 0$ and $\tilde{s}_y < 0$ for the two domains, shown in Figure 3.11. In this case, we find the center of TB lies at sites when the lattice energy E_{lattice} is relaxed, as indicated in Figure 3.11.

From Table 3.1, the winding numbers of domains separated by TB are identical for Figure 3.10 case, while different for Figure 3.11 case. The band structure shown

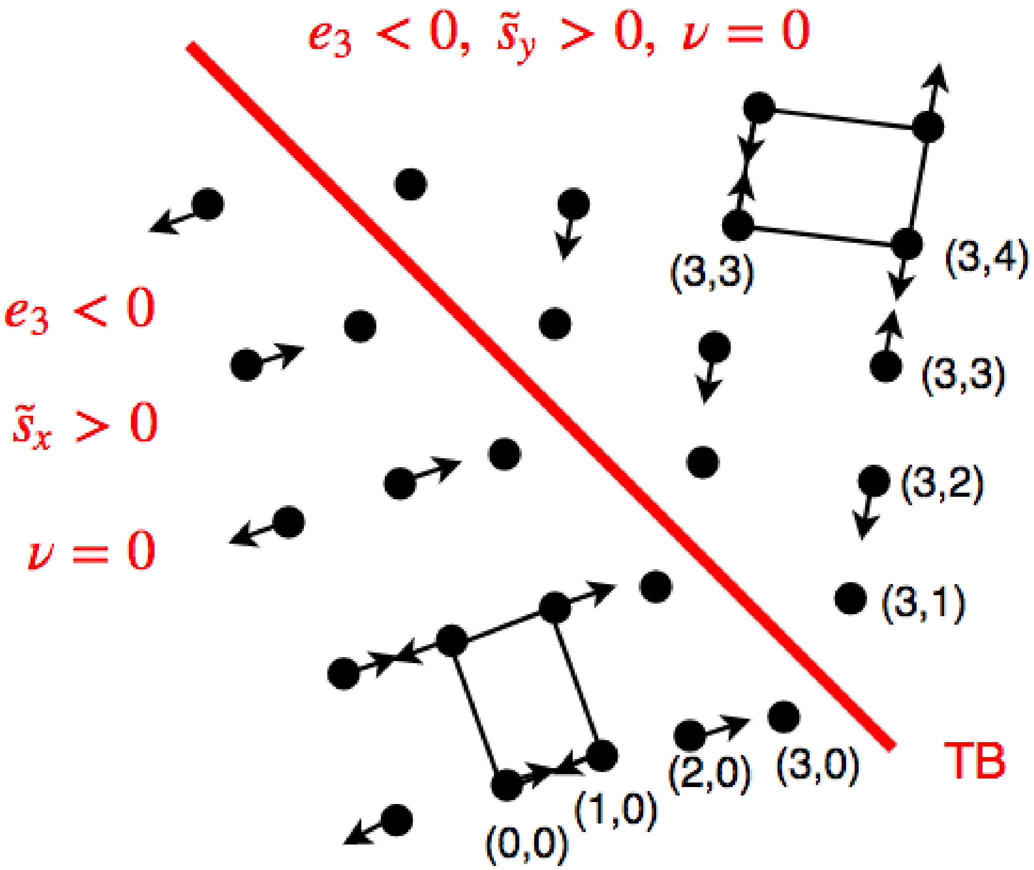

Figure 3.10 TB along 135°, and beside the TB, $\tilde{s}_x$, $\tilde{s}_y$ have the same sign.

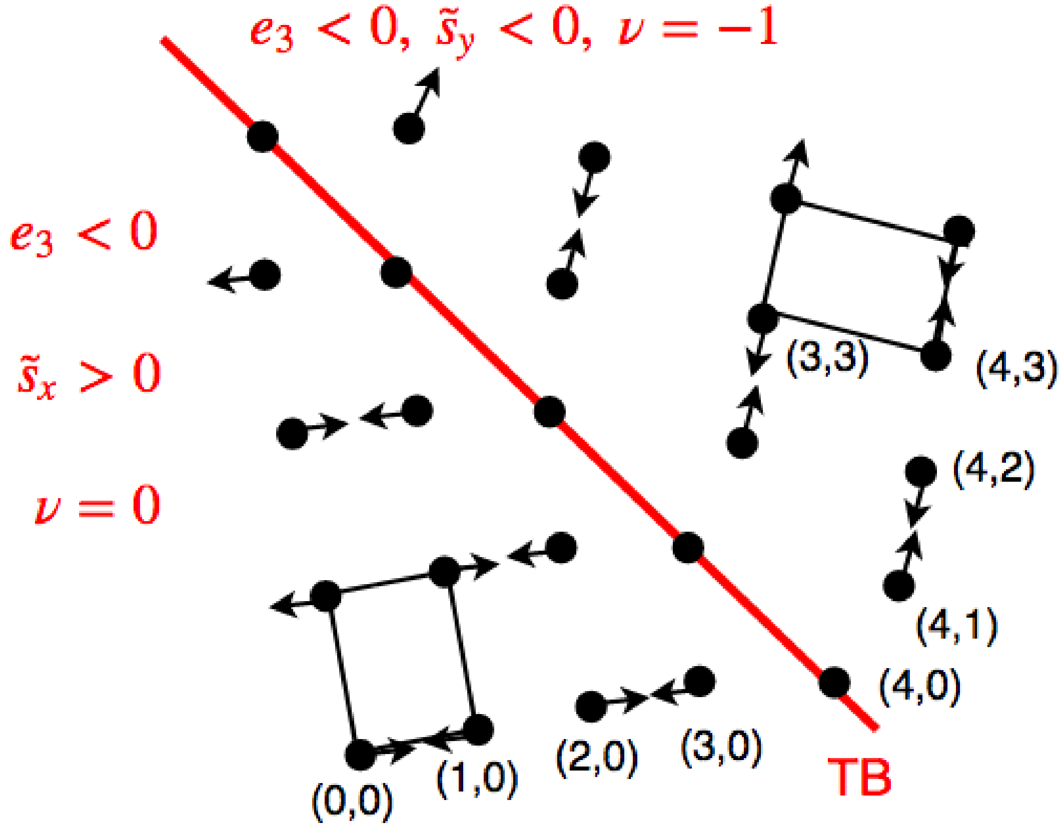

Figure 3.11 TB along 135°, and beside the TB, $\tilde{s}_x$, $\tilde{s}_y$ have the opposite sign.

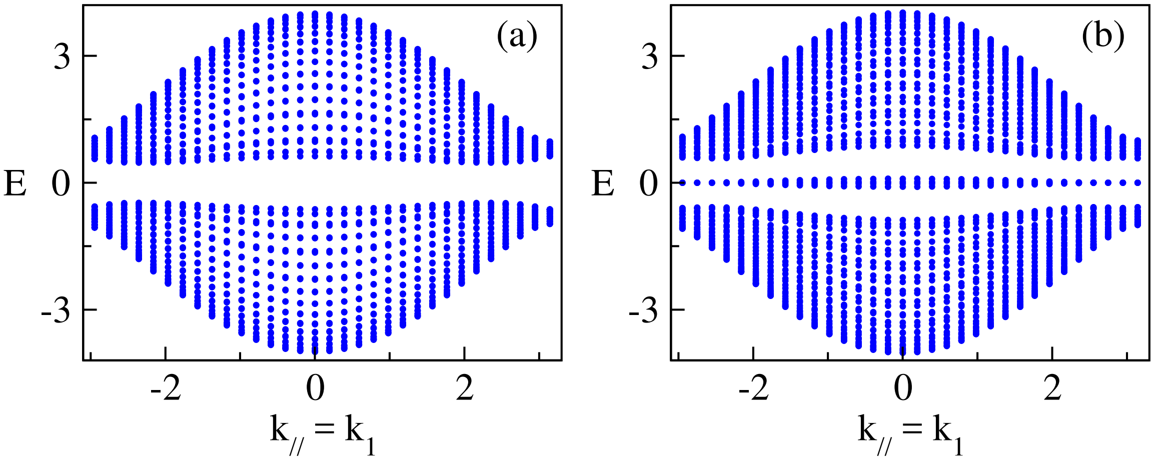

Figure 3.12 (a) Band structure for TB along 135° which separates domains with $\tilde{s}_x$, $\tilde{s}_y$ of the same sign, (b) Band structure for TB along 135°, which separates domians with $\tilde{s}_x$, $\tilde{s}_y$ of opposite signs.

in Figure 3.12(b) reveals the presence of zero energy TB states for Figure. 3.11 case, while Figure 3.12(a) reveals the absence of zero energy TB states for Figure 3.10, consistent with the topological analysis.

3.3.4 Texture of Mixed Twin and Antiphase Boundaries

We further study the electronic properties of structural textures with mixed APB and TB. Specifically, we consider the texture schematically, shown in Figure 3.13(a), in which 45°-APB and two kinds of 135° TB coexist. From the winding number analysis, zero energy gap states are expected only along the thick black line in Figure 3.13(a). We verify that by calculating local DOS at zero energy shown in Figure 3.13(b). Indeed, the zero energy states are localized only particular APB and TB, as predicted by the topological analysis.

As mentioned at the beginning, the flat bands found for the system could be useful to create stable or slowly moving localized states. While the 2D Lieb lattice provides bands that are flat in the 2D Brillouin zone, our 2D lattice provides bands that are flat in the 1D subspace of the 2D Brillouin zone for states localized within the TB/APB/OE. Such difference gives a unique possibility to our lattice, that is,

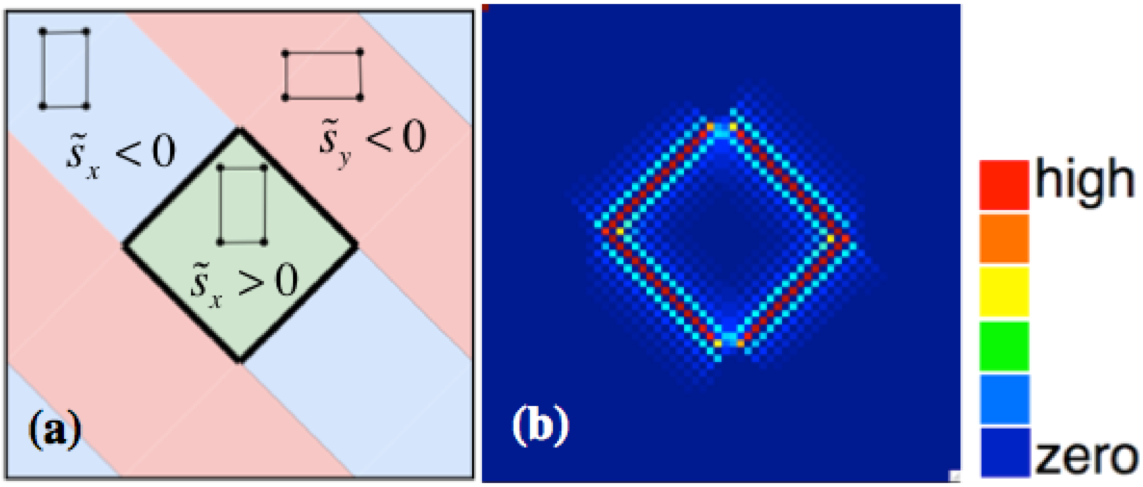

Figure 3.13 (a) Schematic drawing of structural texture with both APB and TB. Blue regions have $e_3 > 0$ and $\tilde{s}_x < 0$, red region have $e_3 < 0$ and $\tilde{s}_y < 0$, and green region have $e_3 > 0$ and $\tilde{s}_x > 0$. Thick black lines indicate the boundaries where zero-energy states are expected from topological analysis. (b) Local DOS at $E = 0$.

the tunability of the band dispersion or the group velocity of localized states by the distance between TB/APB/OE. As a demonstration, we consider a pair of 135° APB, similar to Figure 3.14(b), but with a varying distance D measured along the horizontal direction, for 64×64 unit cells, and find that the dispersion of zero-mode states increases as D decreases. The approximate average group velocity is calculated as $c_g = \left[\varepsilon_{\mathrm{APB}}^{\max}(k_2 = 0) - \varepsilon_{\mathrm{APB}}^{\max}(k_2 = -\pi)\right]/\pi$, where $\varepsilon_{\mathrm{APB}}^{\max}(k_2)$ is the largest among the four zero-mode APB state energies. The result of c_g versus D is shown in Figure 3.14(g), which reveals rapid increase of c_g as D decreases below around 15. This tunability could be useful to design devices with controlled speed of propagation of localized states.

To examine whether the propagation of such localized zero-mode states could change its directions without current loss, a pair of zig-zag APB schematically shown in Figure 3.15(a) for 64×64 atoms are considered, where three domains with a vertical rectangular distortion have the phase of the staggered distortion d_x positive, negative and positive from left to right. The actual distortion pattern for the lower half is shown in Figure 3.15(b). Electronic energy spectrum for the whole distorted lattice is

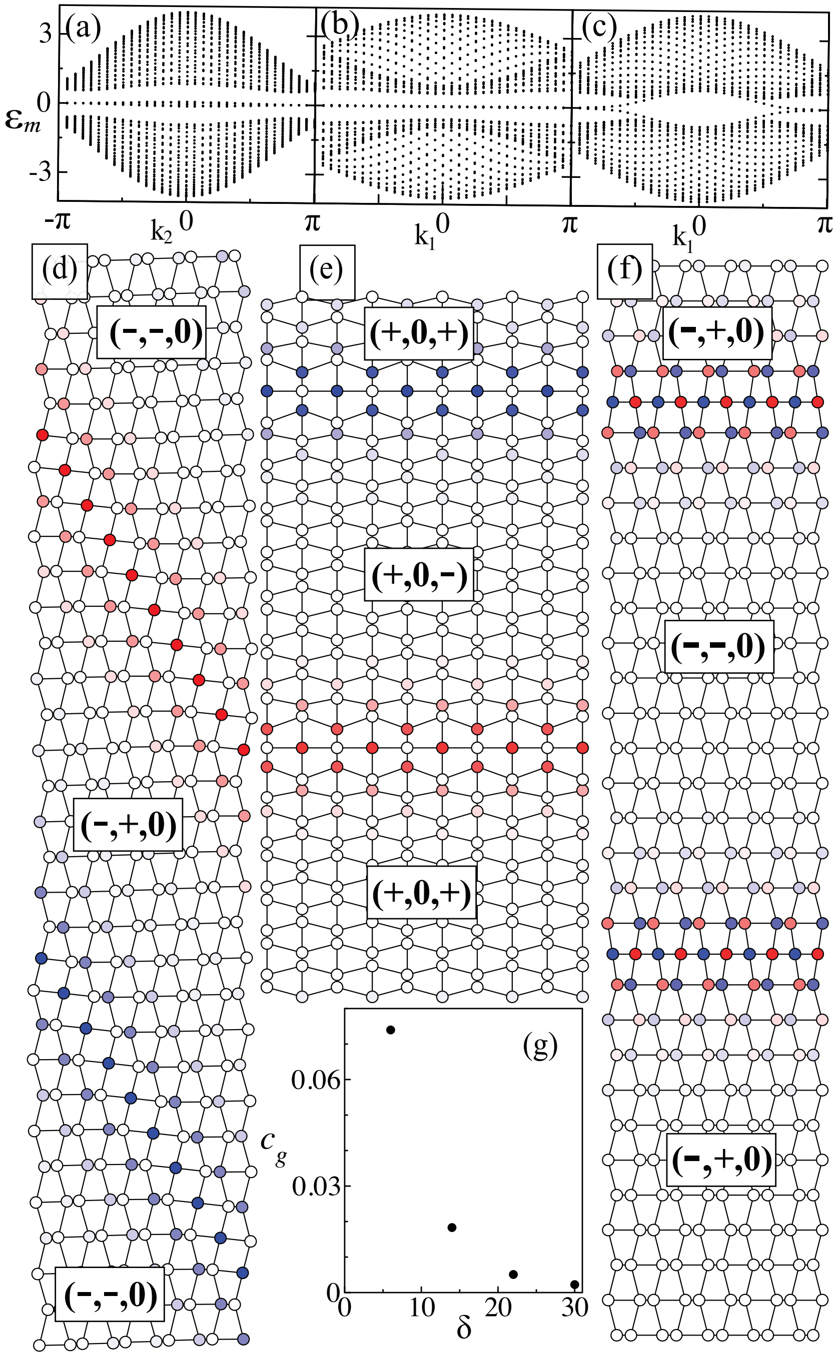

Figure 3.14 (color online) (a), (b), (c) Band structures for the lattices with APB shown in (d), (e) and (f), respectively. APB zero-mode bands are present in (a) and (b), but are absent in (c). Highly dispersive bands inside the gap in (c) are not of topological origin. (d), (e), (f) Lattices with APB in 135° direction for (d) and 0° direction for (e) and (f). In (f), the colors represent the integrated electron density for the states within $\varepsilon_m = \pm 0.1$. (g) Average group velocity c_g versus the number of bonds δ in the horizontal direction between 135° direction APB. Adapted from Ref. [76]

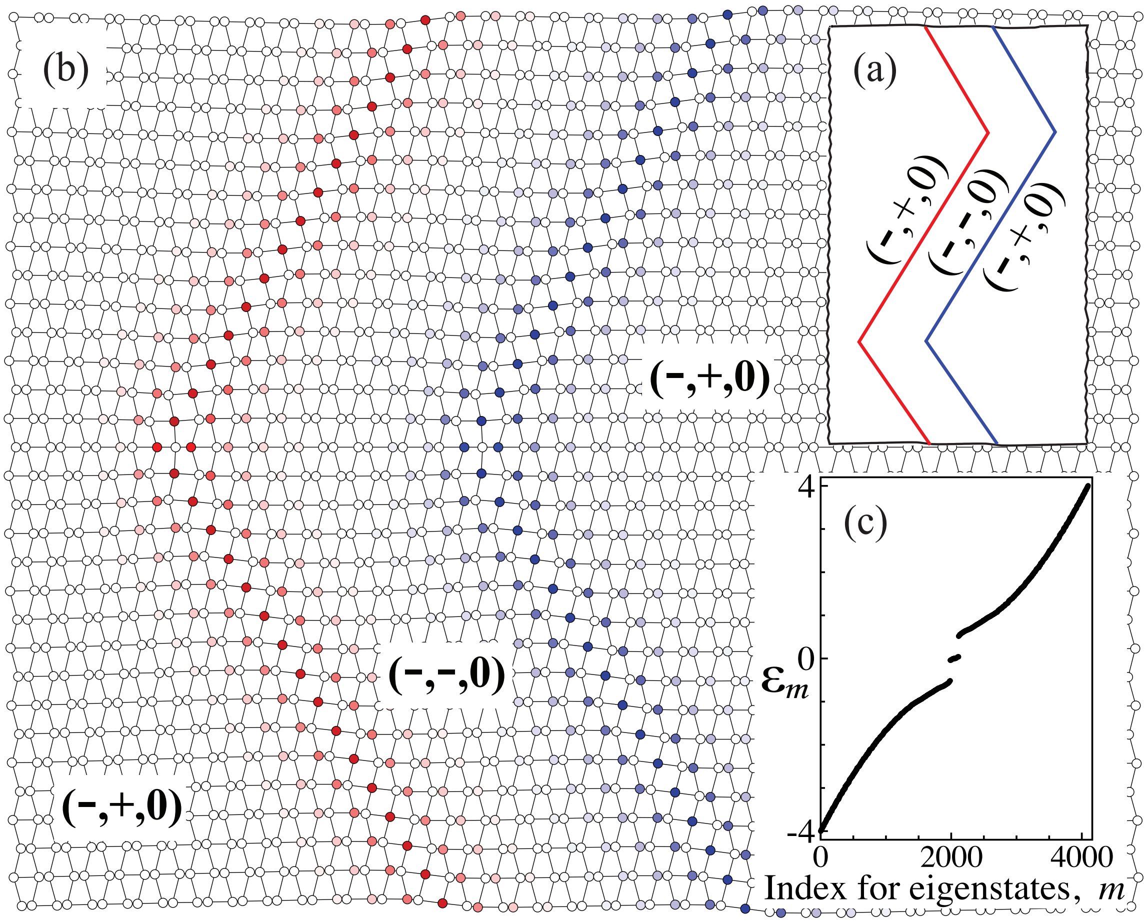

Figure 3.15 (color online) (a) Schematic sketch showing a pair of zig-zag APB with $e < 0$ and $d_y = 0$ for 64 × 64 atoms with periodic boundary conditions. From left to right, the phase of d_x changes from positive to negative back to positive for the three domains; (b) Actual distortion and integrated electron density of zero mode states for the lower half of (a); (c) Plot of energy for eigenstates, ε_m, versus the index m for the states in the order of increasing energy. Adapted from Ref. [76]

found numerically and energy eigenvalue ε_m versus the index of energy eigenstates m in the order of increasing energy is displayed in Figure 3.15(c), which shows that the zero-mode APB states are well separated from bulk states in energy in spite of kinks. The integrated electron density for these zero-mode states shown in Figure 3.15(b) indicates that these modes are confined at APB and the current would not be lost at kinks. Such patterned metamaterials, for example, optical crystals, could be used to guide slowly propagating localized states along desired paths.

Although we have used electronic Hamiltonian as a specific example, our model can be applied to other systems, such as photonic or mechanical metamaterials or cold atom lattices. Because chirality symmetry is essential, the metamaterials should have identical on-site energies, or resonances, at all sites, including TB/APB/OE, and the nearest neighbor coupling should have the variations of weakly coupled shifted SSH chains as studied here.

We discuss what kinds of electronic materials would have topological properties of the Hamiltonian discussed here. First, the materials need to have dimerization, as our 2D model has. Second, the dimerized chain shift alternatively in a direction perpendicular to the chain. Unfortunately, we are not aware of such 2D electronic materials, and perhaps such 2D electronic materials do not exist. However, 3D materials may exist. Then, how could we extend our 2D model to 3D space. Because it is important that the nearest neighbor SSH chains are shifted from each other, the 3D configuration that would have flat topologically protected surface bands might be the configuration in which x-direction SSH chain are shifted and stacked in y and z-directions. The materials which have such dimerized ground states would have topological properties of our Hamiltonian. Although we could not provide explicit chemical formula for such materials, we hope our work motivates experimentalists to search such materials and topologically protected flat energy bands localized within twin and antiphase boundaries and at the open surface.

3.4 Summary

In summary, using a 2D lattice with topology-structure coupling, we have demonstrated the presence of flat zero-mode energy bands in the entire 1D Brillouin zone for states localized within TB/APB/OE. It has been found that the slow group velocity of these localized zero-mode states could be controlled by the distance between the boundaries and guided through a zig-zag pattern. We propose our model can be realized in various metamaterials.

CHAPTER 4

FLAT FREQUENCY BANDS AT OPEN EDGES OF TWO DIMENSIONAL SPINNER SYSTEMS

The work in this chapter was done in collaboration with Prof. Camelia Prodan, David Apigo, Kai Qian, and Prof. Keun Hyuk Ahn from Department of Physics at New Jersey Institute of Technology, and Prof. Emil Prodan, from Department of Physics at Yeshiva University.

4.1 2D Spinner system and effective Hamiltonian

In this chapter, we propose possible experimental realization of our model in Section 3. Although 2D materials with distorted ground state like Figure 3.1 and associated electronic Hamiltonian like Equation [3.1] are not known, 2D meta-materials with Hamiltonians like Equation [3.1] could be fabricated. As a specific example, spinner model Hamiltonian like the ones studied in References [9, 58] are presented here. With four-armed spinners schematically shown in Figure. 4.1(a) that have magnets of different color-coded strengths, a pattern like Figure. 4.1(b) can be generated. The Lagrangians for three pairs of interacting spinners in Figure. 4.1(c)–4.1(e) are written as

$$\begin{aligned} L_{gg} &= \frac{1}{2}I(\dot{\varphi}_1^2+\dot{\varphi}_2^2)-\frac{1}{2}\alpha_g(\varphi_1^2+\varphi_2^2)-\beta_g\varphi_1\varphi_2, \\ L_{bb} &= \frac{1}{2}I(\dot{\varphi}_1^2+\dot{\varphi}_2^2)-\frac{1}{2}\alpha_b(\varphi_1^2+\varphi_2^2)-\beta_b\varphi_1\varphi_2, \\ L_{rr} &= \frac{1}{2}I(\dot{\varphi}_1^2+\dot{\varphi}_2^2)-\frac{1}{2}\alpha_r(\varphi_1^2+\varphi_2^2)-\beta_r\varphi_1\varphi_2, \end{aligned} \tag{4.1}$$

where subscripts g, b, and r represent magnets at the places of green, blue, and red dots, and α_g, α_b, α_r, β_g, β_b, and β_r are all positive.The Lagrangian for the whole

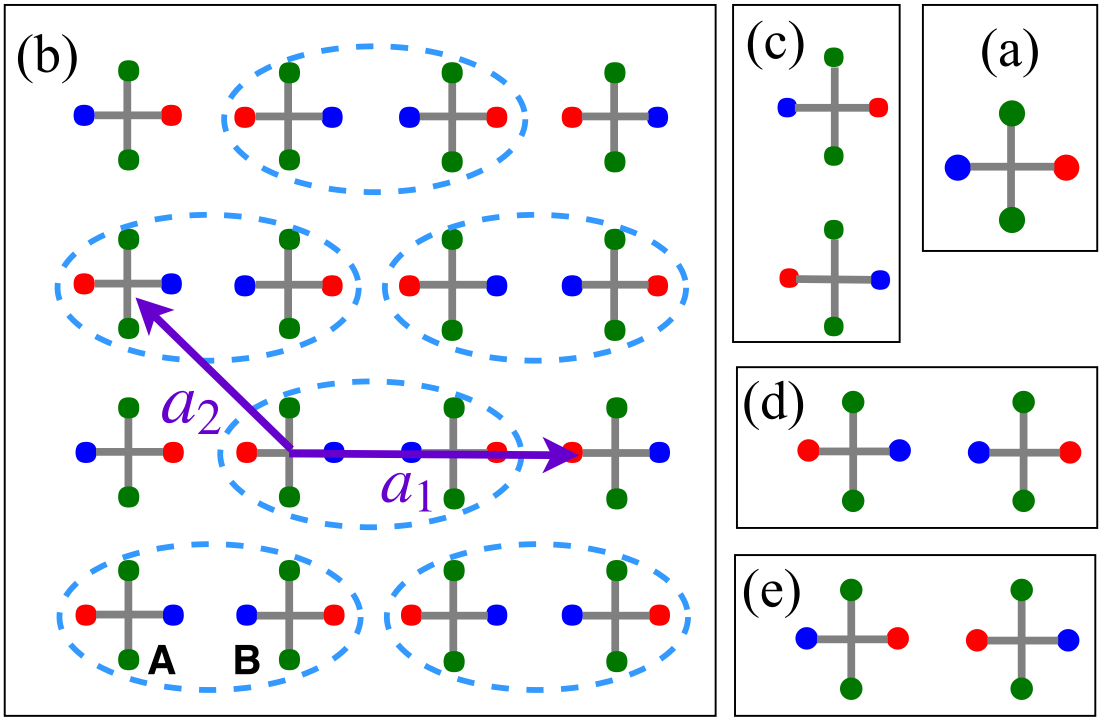

Figure 4.1 (a) The four-armed spinners; (b) A pattern made by the four-armed spinners; (c) Spinners interacting with green pairs; (d) Spinners interacting with blue pairs; (e) Spinners interacting with red pairs. Magnets' south and north poles are aligned, so that all nearest neighbor interactions are attractive. For example, *A* spinner's all four magnets have north poles pointing outward, whole *B* spinner's magnets have south poles pointing outward.

infinite system can be written as:

$$\begin{aligned} L &= \sum_{\mathbf{n}} \frac{1}{2} I(\dot{\varphi}_{\mathbf{n}A}^2 + \dot{\varphi}_{\mathbf{n}B}^2) - \frac{1}{2}\alpha_{\text{tot}}(\varphi_{\mathbf{n}A}^2 + \varphi_{\mathbf{n}B}^2) \\ &- \beta_b \varphi_{\mathbf{n}A}\varphi_{\mathbf{n}B} - \beta_r \varphi_{\mathbf{n}B}\varphi_{\mathbf{n}+(1,1)A} - \beta_g \varphi_{\mathbf{n}A}\varphi_{\mathbf{n}+(-1,0)B} \\ &- \beta_g \varphi_{\mathbf{n}B}\varphi_{\mathbf{n}+(0,1)A} \end{aligned} \tag{4.2}$$

where $\alpha_{\text{tot}} = 2\alpha_g + \alpha_r + \alpha_g$, $\mathbf{n} = (n_1, n_2)$ is the index of unit cell at $\mathbf{R} = n_1\mathbf{a}_1 + n_2\mathbf{a}_2$, and $\mathbf{a}_1$, $\mathbf{a}_2$ are promitive vectors shown in Figure 4.1. To make our spinner system like Figure 1 in Reference [9], we replace one of green magnets by yellow magnet with strengths α_y and β_y, as shown in Figure 4.2. The dynamics of the system can be

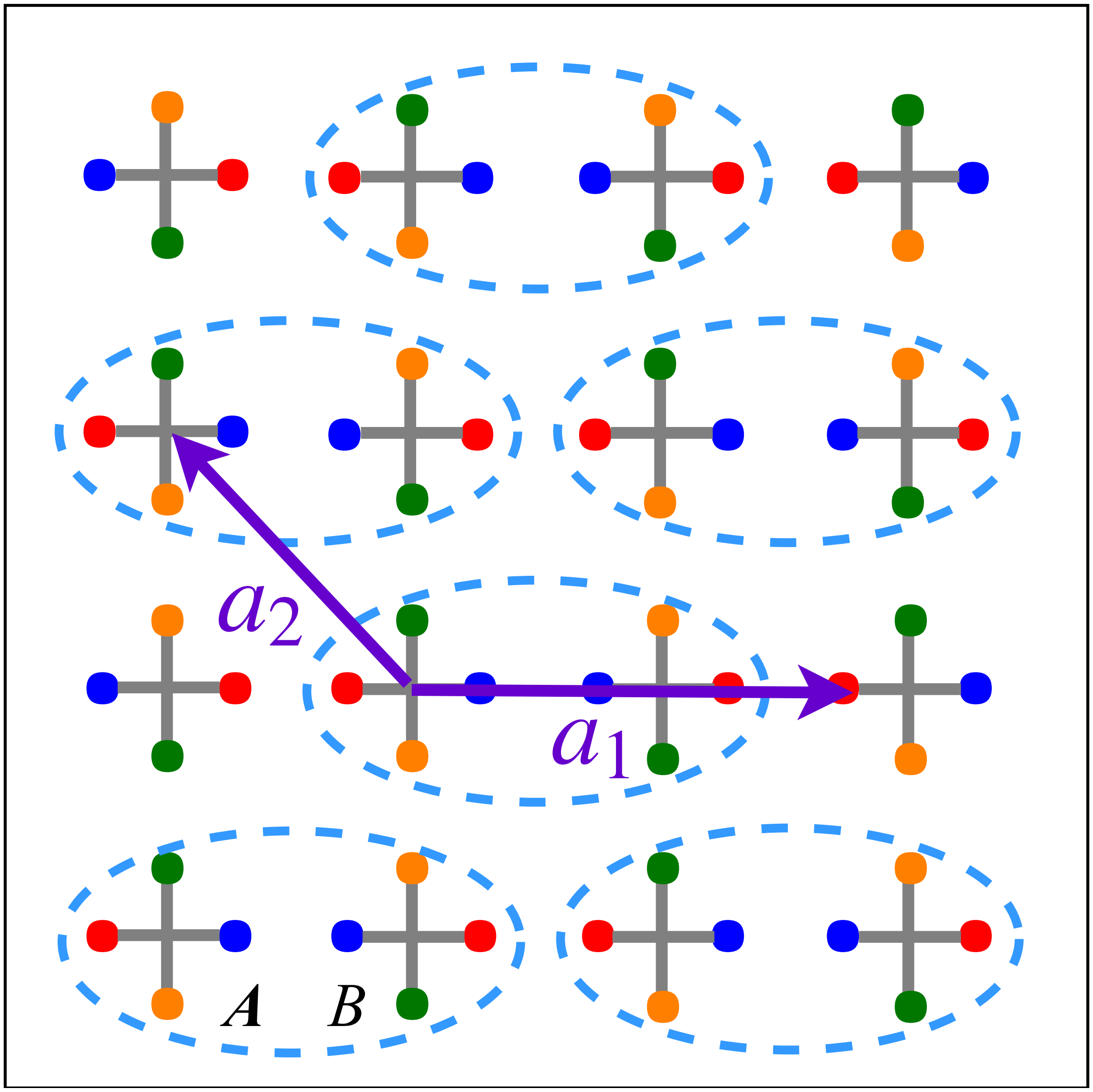

Figure 4.2 A pattern made by the four-armed spinners, with magnets of four different strengths, represented by red, blue, green, and yellow colors. Similar with Figure 4.1, replace one of green magnets by yellow magnet.

described by the following Hamiltonian,

$$4\pi^2 I f^2 \left|\Psi\right\rangle = H \left|\Psi\right\rangle \tag{4.3}$$

with

$$\begin{aligned} H_{spinner} &= \sum_{\mathbf{n}} \alpha_{\text{tot}} \left|\mathbf{n}, A\right\rangle \left\langle\mathbf{n}, A\right| + \alpha_{\text{tot}} \left|\mathbf{n}, B\right\rangle \left\langle\mathbf{n}, B\right| \\ &- \beta_b \left|\mathbf{n}, A\right\rangle \left\langle\mathbf{n}, B\right| - \beta_r \left|\mathbf{n}, B\right\rangle \left\langle\mathbf{n} + (1,0), A\right| \\ &- \beta_g \left|\mathbf{n}, A\right\rangle \left\langle\mathbf{n} + (0,1), B\right| \\ &- \beta_y \left|\mathbf{n}, B\right\rangle \left\langle\mathbf{n} + (1,1), A\right| + \text{H.c}, \end{aligned} \tag{4.4}$$

with $\alpha_{\text{tot}} = \alpha_b + \alpha_r + \alpha_g + \alpha_y$. The first two terms represent a constant shift of energy levels, which do not affect the topological analysis. Comparison between the remaining four terms and Equation [3.1] reveals the following relations would make the spinner system and the electron system on distorted lattice with $d_y = 0$ equivalent,

$$\begin{aligned} \beta_b &= t_0(1 - e + 2d_x), \\ \beta_r &= t_0(1 - e - 2d_x), \\ \beta_g &= t_0(1 + e + 2d_y), \\ \beta_y &= t_0(1 + e - 2d_y), \end{aligned} \tag{4.5}$$

where the hopping amplitude without any distortion is chosen as t_0, a positive number. By inverting these relations, we obtain

$$\begin{aligned} t_0 &= \frac{\beta_r + \beta_b + \beta_g + \beta_y}{4}, \\ d_x &= \frac{\beta_b - \beta_r}{\beta_r + \beta_b + \beta_g + \beta_y}, \\ d_y &= \frac{\beta_g - \beta_y}{\beta_r + \beta_b + \beta_g + \beta_y}, \\ e &= \frac{\beta_g + \beta_y - \beta_b - \beta_r}{\beta_r + \beta_b + \beta_g + \beta_y}, \end{aligned} \tag{4.6}$$

Table 4.1 Winding Number $\nu(135°)$ and $\nu(0°)$ Depend on β_g, β_y, β_r, β_b.

$\beta_g + \beta_y - \beta_b - \beta_r$	$\beta_b - \beta_r$	$\beta_g - \beta_y$	$\nu(135°)$	$\nu(0°)$
+	0	+	0	-1
+	0	-	1	+1
-	+	0	0	0
-	-	0	1	0

that is $\beta_r + \beta_b + \beta_g + \beta_y > 0$. For the electron system studied in Ref [76], the conditions of $d_y = 0$, $e < 0$, $d_x \neq 0$ or $d_y \neq 0$, $e > 0$, $d_x = 0$ result in the gap between bulk bands. From the above relations between t_0, d_x, d_y, e and (β_b, β_r, β_g, β_y), these conditions for the gap opening are translated to $\beta_g = \beta_y$, $\frac{\beta_r+\beta_b}{2} > \beta_g$, $\beta_r \neq \beta_b$ or $\beta_r = \beta_b$, $\frac{\beta_g+\beta_y}{2} > \beta_b$, $\beta_g \neq \beta_y$. Antiphase boundary either along 135° or 90° would host topologically protected oscillation modes. Unlike lattice distortion model in Figure 3.10 and 3.11, the direction of twin boundary for spinner system is not restricted to 45° and 135°, but could have 0° and 90° also and meandering TBs are also possible. Other meta materials, such as the lattice of semiconductor pillars or holes, could also simulate the Hamiltonian in Equation 3.1. The winding number $\nu(135°)$ and $\nu(0°)$ depend on β_g, β_y, β_r, β_b as shown in Table 4.1, or equivalently Table 4.1, obtained from Table I in Ref. [76]. So far, infinite 2D systems with periodic boundary conditions are considered. Before analyzing 2D systems with open edges, infinite and finite 1D spinner systems are analyzed in the following subsection.

4.2 1D SSH Spinner System with Open Edges

We first study a 1D spinner system to gain insights on spinner systems, particularly with open edges. Here, we consider a 1D spinner chain that simulations Su-SchriefferHeeger Hamiltonian. Following the analogy explored in the previous subsection and the studies in Refs. [9, 58], we consider 1D chain shown in Figures 4.3

Table 4.2 Winding Number $\nu(135°)$ and $\nu(0°)$ Depend on β_g, β_y, β_r, β_b.

$\beta_g + \beta_y - \beta_b - \beta_r$	$\beta_b - \beta_r$	$\beta_g - \beta_y$	$\nu(135°)$	$\nu(0°)$
$\beta_b = \beta_r < \frac{\beta_g+\beta_y}{2}$	$\beta_b = \beta_r$	$\beta_g > \beta_y$	0	+1
$\beta_b = \beta_r < \frac{\beta_g+\beta_y}{2}$	$\beta_b = \beta_r$	$\beta_g < \beta_y$	1	+1
$\beta_g = \beta_y < \frac{\beta_b+\beta_r}{2}$	$\beta_b > \beta_r$	$\beta_g = \beta_y$	0	0
$\beta_g = \beta_y < \frac{\beta_b+\beta_r}{2}$	$\beta_b < \beta_r$	$\beta_g = \beta_y$	1	0

and 4.4. The set up in Figure 4.4 has been also used for experiments, which will be discussed below. The long and short distances (or wide and narrow gap) between magnets are 8 mm and 5 mm and corresponding α and β parameters are indicated by subscript L and S in the equations below.

There is an impotent difference between electron systems studied in Chapter. 3 and spinner systems studied here. While the onsite energy at TB/APB/OE is equal to that inside bulk for electron system, the on-site energy, or resonant energy at TB/APB/OE may not be the same as that inside bulk for spinner system. That is because interactions between magnets give both resonant energy parameterized by α's and the interaction energy parameterized by β's. So if we have terminate of spinners like Figure 4.3, α_{tot} for the spinners at both edges will be different from spinners inside, which would break the chiral symmetry of the system and invalidate all topological arguments. To fix this problem, we should add spinners at the end that are immobile but have magnets like other spinners like Figure 4.4. In that way, all spinners, inside and at the edges, have the identical resonant energy α_{tot} and the chiral symmetry is restored, which allows the application of topological arguments. With these fixed spinners, the Lagrangian for spinner systems like Figure 4.4 is written as:

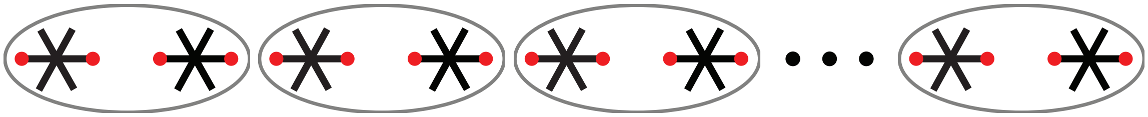

Figure 4.3 The 1D spinner system with the open edge. Grey line demonstrated unit cells.

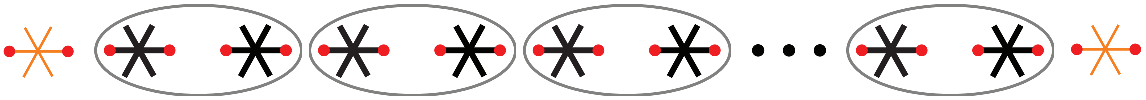

Figure 4.4 The 1D spinner system with the two fixed side spinners. Grey line demonstrated unit cells.

$$
\begin{aligned}
L &= \frac{1}{2}I\dot{\varphi}_l^2 + \frac{1}{2}I\dot{\varphi}_r^2 + \sum_n \frac{1}{2}I\dot{\varphi}_n^2 \\
&- \frac{1}{2}\alpha_l\varphi_l^2 - \frac{1}{2}\alpha_r\varphi_r^2 - \frac{1}{2}\sum_{n=1}^{N-2}(\alpha(d_{n-1}) + \alpha(d_n)) \\
&- \frac{1}{2}(\alpha_l + \alpha_0)\varphi_0^2 - \frac{1}{2}(\alpha_{N-2} + \alpha_r)\varphi_{N-1}^2 \\
&- \sum_{n=0}^{N-2}\beta(d_n)\varphi_n\varphi_{n+1} - \beta_l\varphi_l\varphi_0 - \beta_r\varphi_{N-1}\varphi_r. \qquad (4.7)
\end{aligned}
$$

If we fix the left and right spinner, $\dot{\varphi}_l$, $\dot{\varphi}_r$, φ_l, φ_r are zero. The Lagrangian for the 'fixed two side' spinner system:

$$
\begin{aligned}
L &= \sum_{n=0}^{N-1}\frac{1}{2}I\dot{\varphi}_n^2 + \sum_{n=1}^{N-2}\left[-\frac{1}{2}(\alpha(d_{n-1}) + \alpha(d_n))\varphi_n^2 - \beta(d_n)\varphi_n\varphi_{n+1}\right] \\
&- \frac{1}{2}(\alpha_l + \alpha_0)\varphi_0^2 - \frac{1}{2}(\alpha_{N-2} + \alpha_r)\varphi_{N-1}^2. \qquad (4.8)
\end{aligned}
$$

The dynamics of the system can be described by the Hamiltonian:

$$
f^2 |\Psi\rangle = H |\Psi\rangle . \qquad (4.9)
$$

where the Hamiltonian as follow:

$$
\begin{aligned}
H &= \sum_{m=0}^{M-1} (\alpha_L + \alpha_R)(|\mathbf{m}, A\rangle \langle \mathbf{m}, A| + |\mathbf{m}, B\rangle \langle \mathbf{m}, B|) \\
&+ \beta_L(|\mathbf{m}, A\rangle \langle \mathbf{m}, B| + |\mathbf{m}, B\rangle \langle \mathbf{m}, A|) \\
&+ \beta_S(|\mathbf{m}+1, A\rangle \langle \mathbf{m}, B| + |\mathbf{m}, B\rangle \langle \mathbf{m}+1, A|), \qquad (4.10)
\end{aligned}
$$

where m represents the index of unit cell, and α's and β's are normalized by $4\pi^2 I$ as done in Ref. [9].

From Ref. [9], $\alpha_L = 160$, $\alpha_L = 350$, $\beta_L = 130$, $\beta_S = 280$ for 5 mm and 8 mm gaps. From the Hamiltonian, we can get the frequency, and the results are shown in Table 4.3, in Figure 4.5.

For the 'edge' states ($f = 22.57\ Hz$ and $f = 22.59\ Hz$), we plot the eigenvector in Figure. 4.6. It shows that only A spinners are oscillating near the left edge while B spinners are oscillating near the right edge, consistent with the results for electronic SSH model and topological argument. For easier comparison with experiments, we also show absolute values of eigenvectors in Figure 4.7.

Professor Camelia Prodan group carried out preliminary measurements, shown in Figures 4.8 and 4.9.

The label 1-16 in Figure 4.8 represent the index of the spinner, n. Spinner (n=1) is put into oscillation by actuator and the oscillations of other spinners are measured by sensors and RMS voltage output from the sensors are plotted versus frequency of the actuator for different spinners, $n = 1, \cdots, 16$. Although this data is preliminary, important features are consistent with our theoretical calculations in Table 4.3, Figure 4.5, 4.6, and 4.7. First, the frequency range of bulk modes is about 10-18 Hz and 27-31 Hz in experimental data in Figures 4.8, consistent with calculation foe 10-18 Hz and 26-30 Hz. The frequencies of edge modes in side the bulk gap are about 21-23 Hz in experiments in Figure 4.8, consistent with about 22.6 Hz predicted in calculation in Table 4.3. Professor Prodan group plotted edge mode

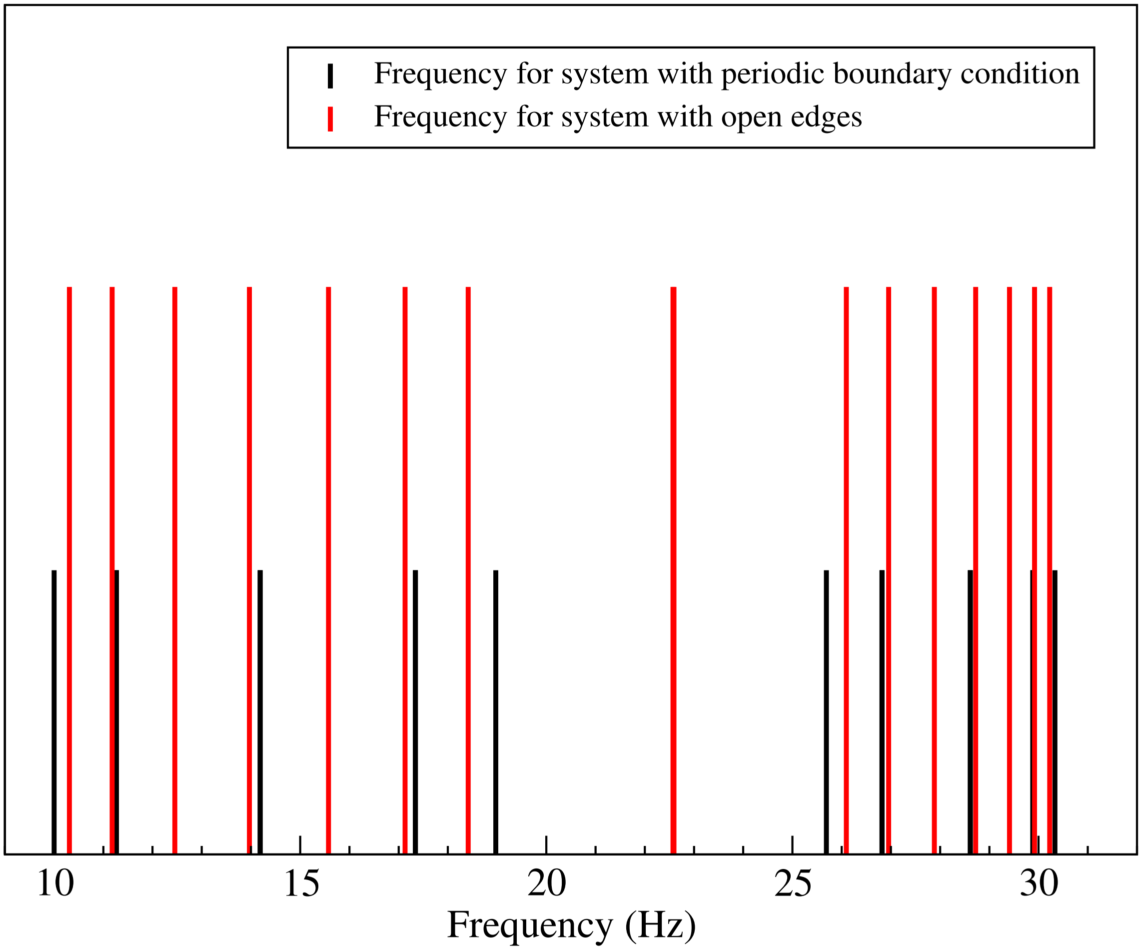

Figure 4.5 The frequency for the spinner system with period boundary condition and with open edges.

Table 4.3 Frequency (Hz) for 1D Spinner System with Eight Unit Cells

Calculated Frequencies (Hz) for System with Period Boundary Condition	Calculated Frequencies (Hz) for System with Open Edges
10.00	10.30
11.26	11.18
11.26	12.45
14.18	13.96
14.18	15.58
17.33	17.13
17.33	18.41
18.93	**22.57**
25.69	**22.59**
26.82	26.09
26.82	26.95
28.61	27.88
28.61	28.72
29.88	29.41
29.88	29.91
30.33	30.23

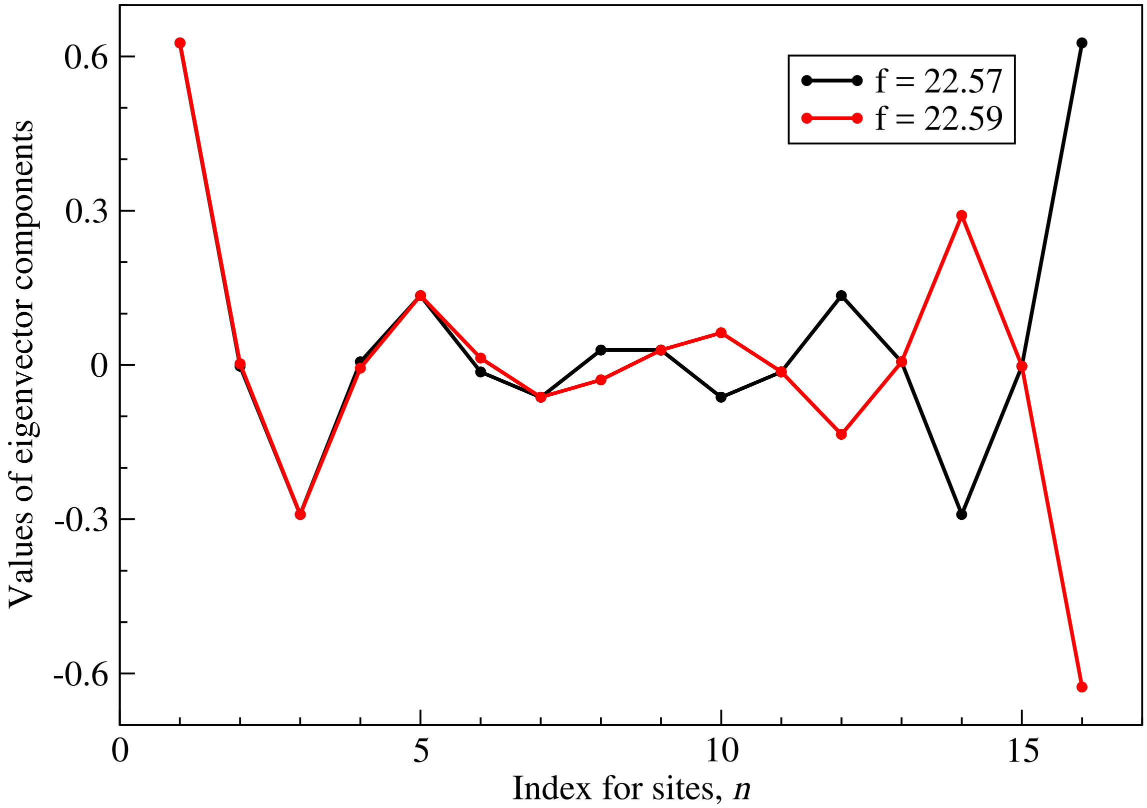

Figure 4.6 The values of eigenvector component for the edge modes at each site.

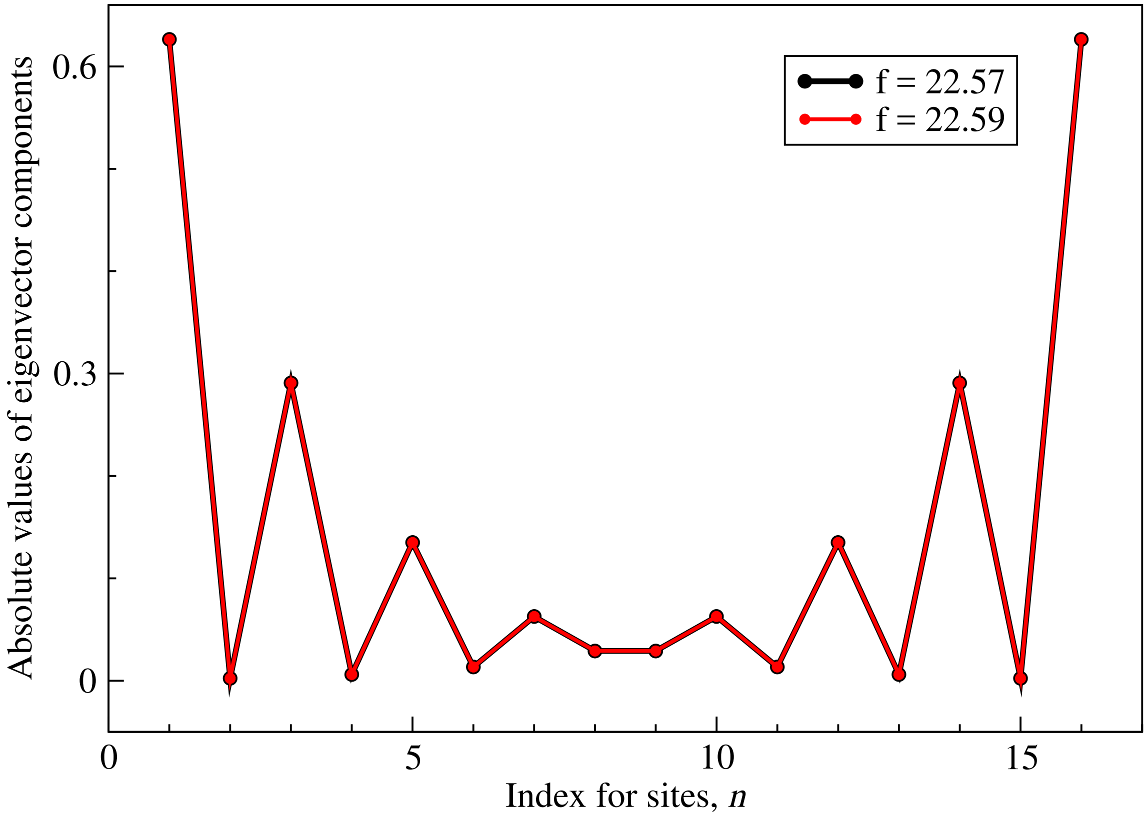

Figure 4.7 The absolute value of eigenvector component for the edge modes at each site.

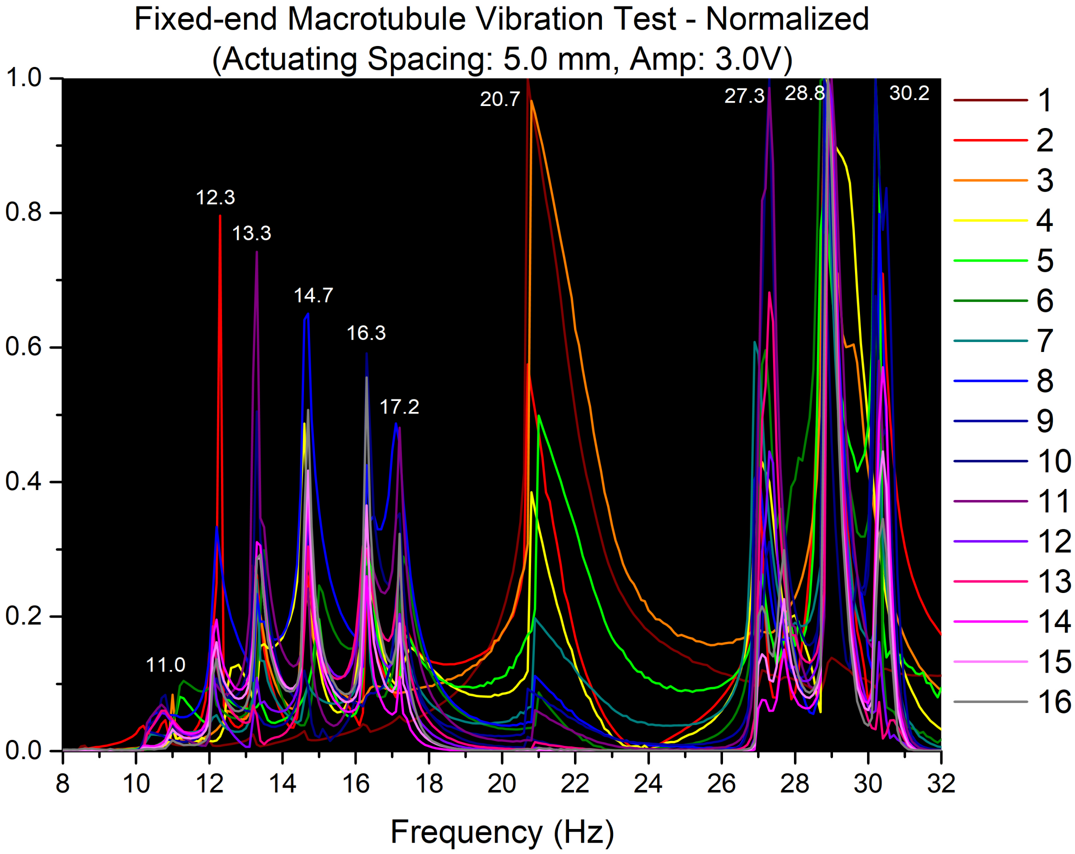

Figure 4.8 Preliminary experimental data for the frequency for the spinner system with eight unit cells and open edges. This data has been obtained by Prof. Camelia Prodan, David Apigo, and Kai Qian at New Jersey Institute of Technology.

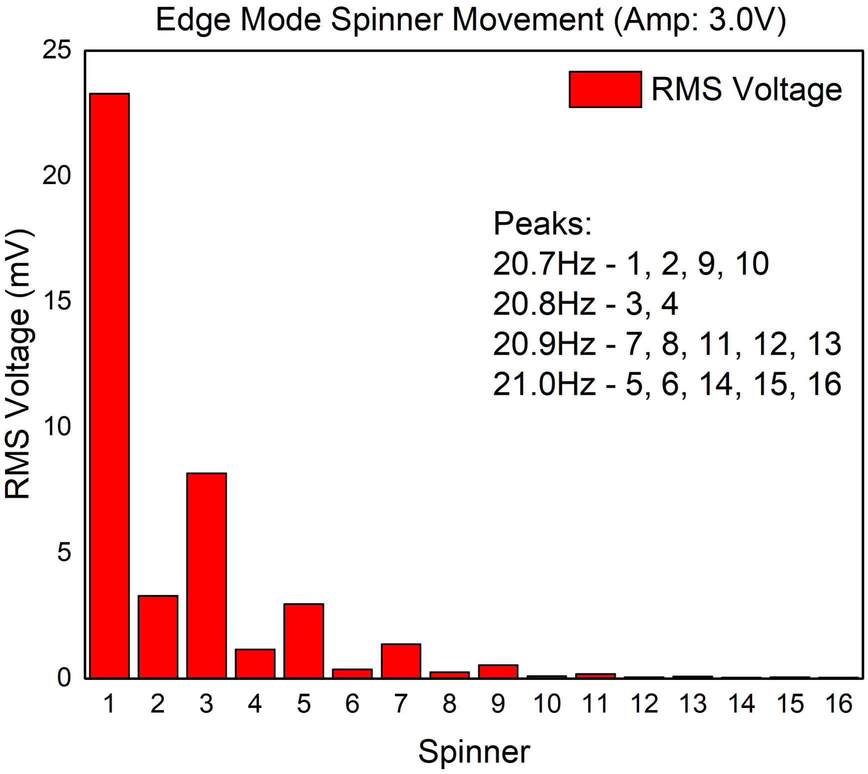

Figure 4.9 The experimental movement for edge mode of the spinner system with open edge. his data has been obtained by Prof. Camelia Prodan, David Apigo, and Kai Qian at New Jersey Institute of Technology.

strength versus spinner index n from the RMS voltage measured for the actuator frequency around 21 Hz, and have shown in Figure 4.9. Comparison with theoretical prediction in Figure 4.6 show simulating, that is, large components on A-spinners for the edge mode on left. However, in experimental data, B-spinners also have small but finite amplitude, unlike the theoretical prediction. Movie of the edge mode oscillation confirms that spinner 1 and spinner 3 rotate in opposite directions, consistent with Figure 4.6. The agreements between theory and preliminary experimental data show the model and topological and numerical analyses describe experiments reasonably well. We now present our calculation for 2D system with open edges.

4.3 Experimental Model 2D Ribbon Spinner System with 135° Open Edge

Finally, we consider 2D spinner systems with open edges. Specifically, we focus on the 'spinner ribbon' along 135° with the open edges at the two sides, as show in Figure. 4.10. The spinners with black arms are rotatable, while the spinner with orange arms at the both edges are fixed, so that the system has the chiral symmetry, just like 1D case in the previous section.

With $\beta_g < \frac{\beta_b+\beta_r}{2}$ and $\beta_b < \beta_r$, the system has a winding number $\nu(135°) = 1$ for 135° direction open edges and the flat frequency band is expected on each edge. The goals of our study are how the flatness of the edge mode bands and the slow group velocity of localized edge states would depend on the width of the ribbon. Experimental set up is not ready yet, and we use typical values of β_r, β_b, β_g, α_{tot} for demonstrations. Specifically, we use $\beta_r = 250.0$, $\beta_b = 150.0$, $\beta_g = 120.0$, and $\alpha_{tot} = 750.0$. The plots of f^2 versus k_2 and f versus k_2 are shown in Figures. 4.11 and 4.12, where the number of unit cells in the horizontal direction is 4, 8, and 12. The results show the edge states in the gap, with dispersion decreases are the ribbon becomes wider. An example of the map of integrated mode strengths for these edge modes is

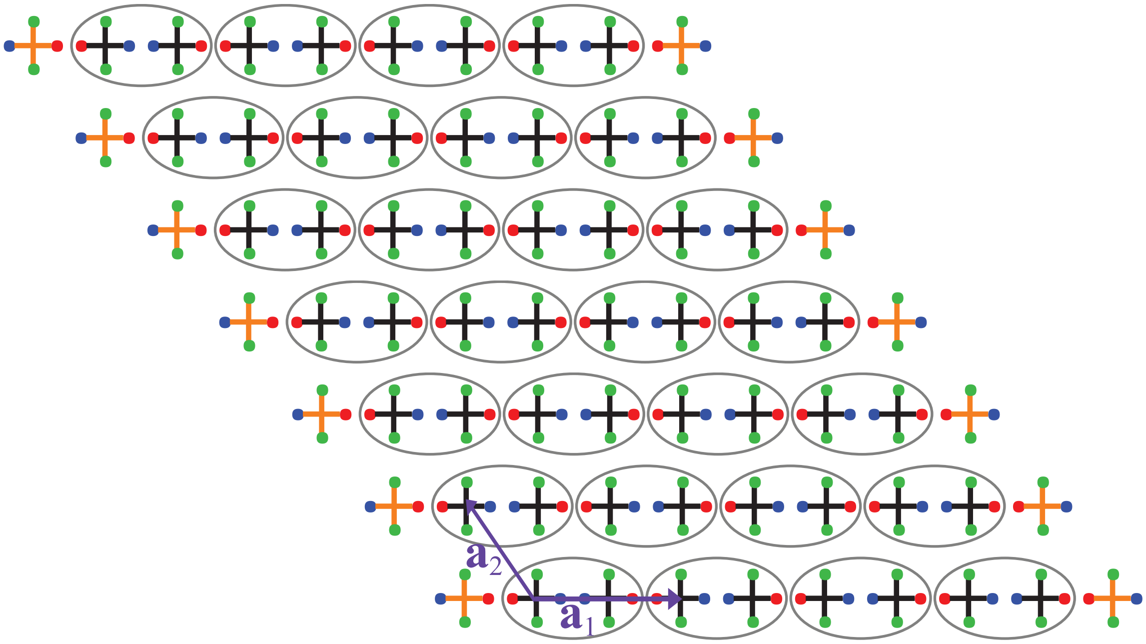

Figure 4.10 Four-armed spinner ribbon system along 135° with the open edges.

shown in Figure 4.13 for a 16 unit cell wide ribbon, where the red and blue colors represent A and B sites, respectively. The results are consistent with predictions based on topological analysis, in particular, bulk-boundary correspondence.

From the dispersion, we estimate the group velocity c_g of the localized edge excitation as $c_g = \frac{\Delta\omega}{\Delta k} = 2\pi\Delta f a$ where a is the axis-to-axis distance between the nearest neighbor spinners, and Δf is the charge of edge mode frequency between zone boundary and zone center. The results are shown in Figure 4.14 for ribbon with the unit cell number 4, 8, 12, 16 and 20, which shows the sensitive dependence of the group velocity c_g with the width of the spinner ribbon. With c_g ranging from less than 1 cm/s to 10 cm/s, the slow propagation of the edge mode and its dependence on the ribbon width will be studied experimentally by Professor Prodan group and compared with the theory results shown here. It is clear, for this case, we choose the primitive vectors $\mathbf{a}_1$ and $\mathbf{a}_2$ as before, and the boundaries along $\mathbf{a}_2$ direction. From Equation 4.3, we can plot the f^2 for different k_2. In the Figure 4.11, we show an example when we have 16 unit cells (32 spinners), the relation between f^2 and k_2.

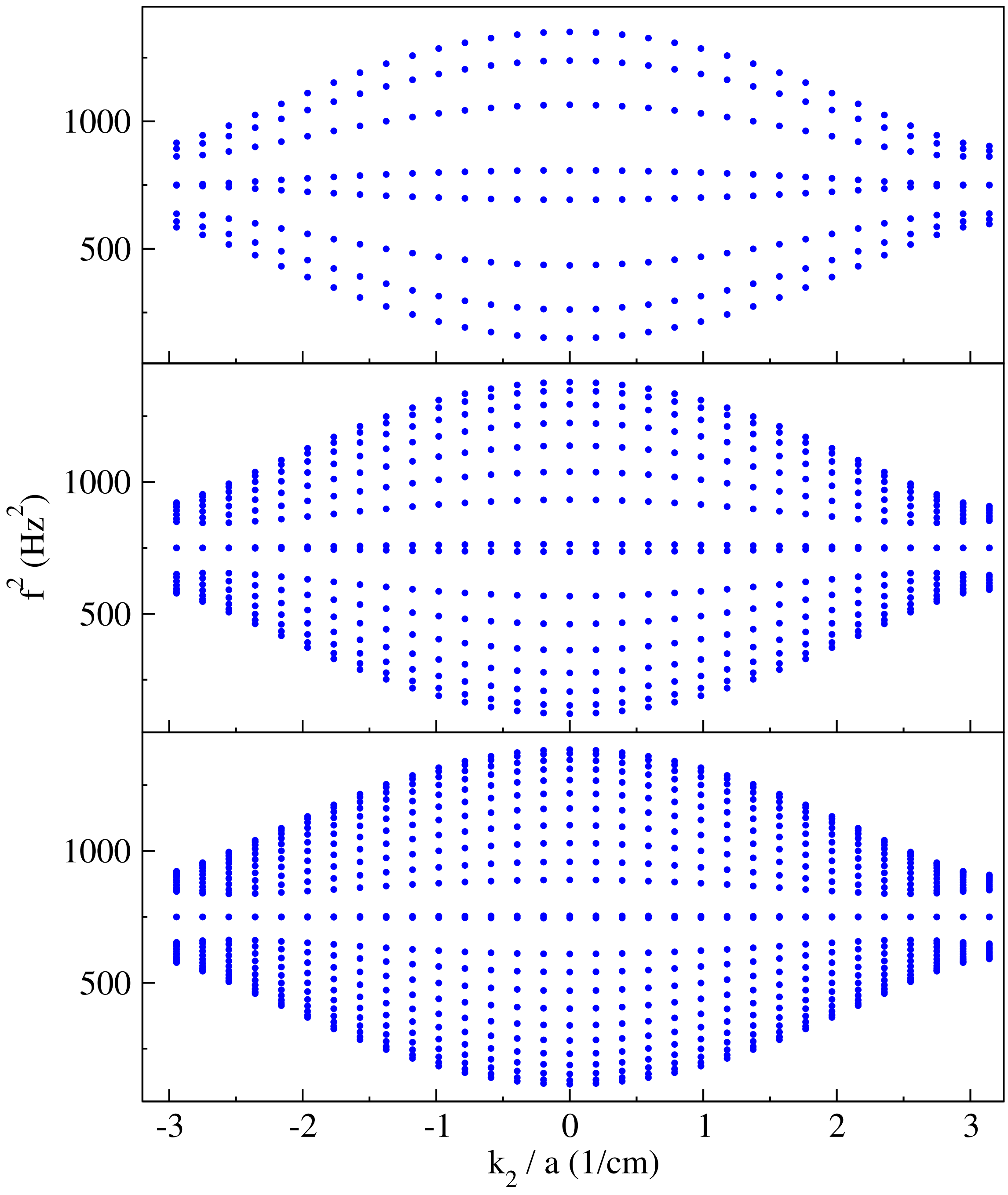

Figure 4.11 With different unit cells (4,8, and 12), the relation between f^2 and k_2/a.

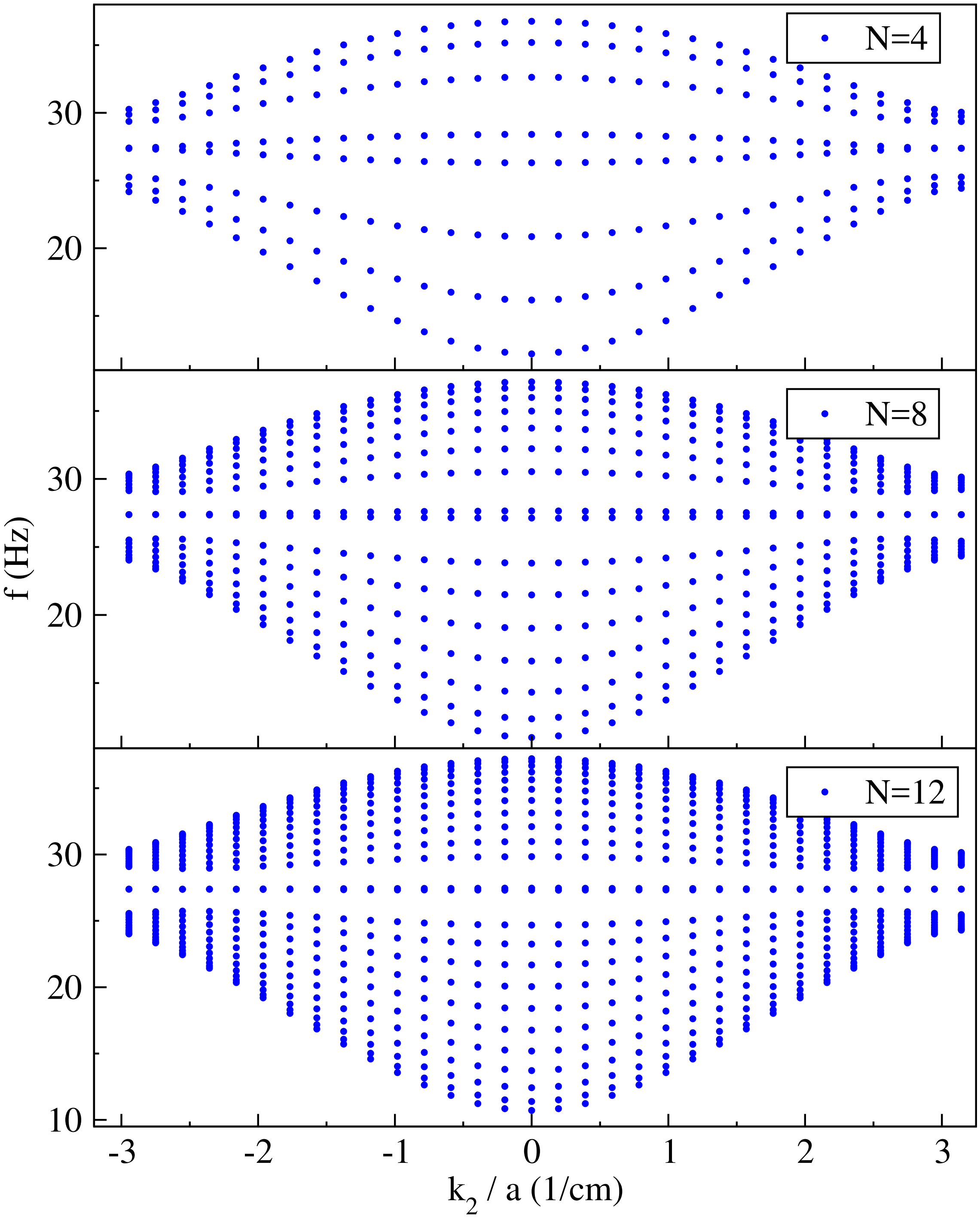

Figure 4.12 With different unit cells (4,8, and 12), the relation between f and k_2/a.

We can see the edge states in the gap, as we expected. Also, we plot the f for this case in Figure. 4.12. For the 'spinner ribbon' system, when we change D (the number of spinners we set), we can get the group velocity and show in Figure.4.14.

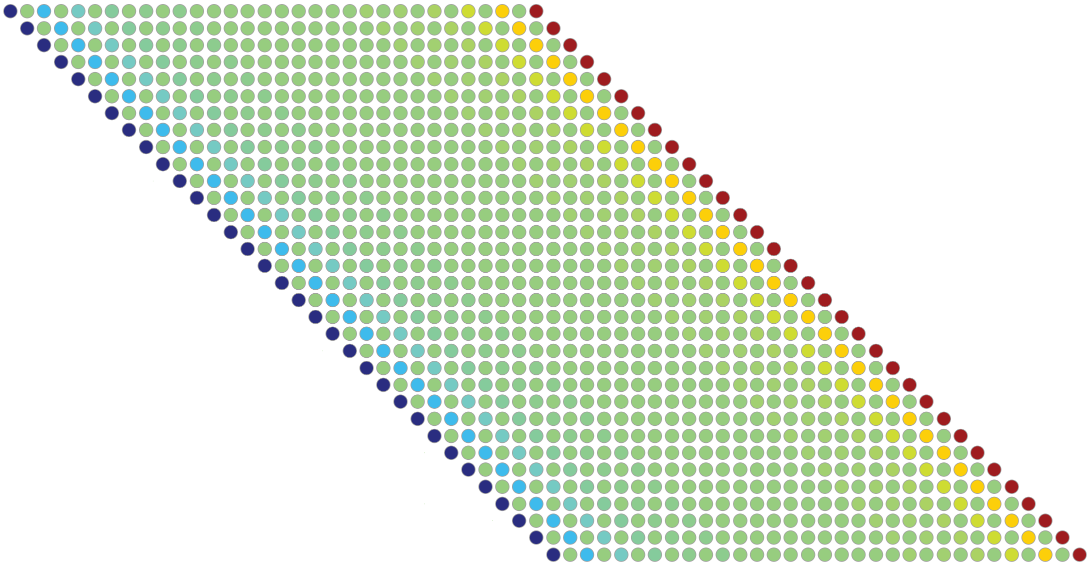

Figure 4.13 Map of Integrated mode strengths for the edge bands for a spinner ribbon with 16 unit cell width. The red and blue colors represent A and B sites, respectively.

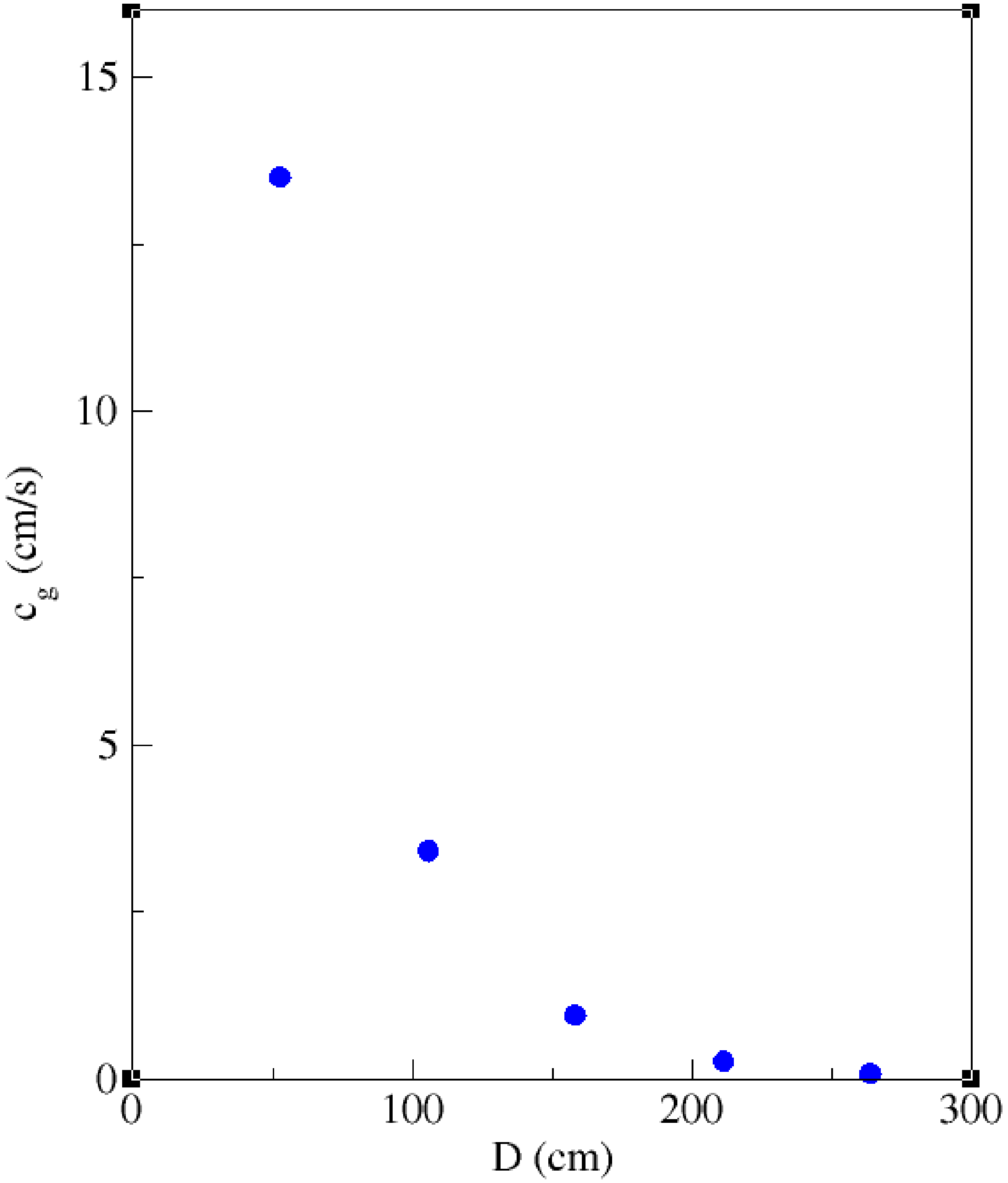

Figure 4.14 The group velocity of edge modes versus the width of the spinner ribbon. Results for 4, 8, 12, 16, and 20 unit cell wide ribbons are shown here.

CHAPTER 5

SUMMARY

First, we studied photoinduced nonequilibrium dynamics in CO materials, with coupled electrons, periodic lattice distortions, and incoherent phonons. Our simulation shows a damped oscillation of coherent lattice distortion after the electronic excitation by the optical pulse. By studying the stages of CO melting, we identified the CO gap reopening, and thermal relaxation. During the stage of CO melting, the dynamics of the periodic lattice distortion is partially decoupled from and lags behind the dynamics of electronic order parameter due to large inertia of ions. When the effective electron temperature drops below the critical temperature, CO gap open again and the electronic state changes from thermal to nonthermal. During the stage of thermal relaxation, the electron system and the periodic lattice distortion maintain internal equilibrium, as they relax back to the initial state. The energy efficiency of photoinduced switching from insulator to metal increases, as the photon energy is reduced towards the CO gap. The frequency of coherent oscillation depends sensitively on time, fluence, and photon energy, which correlates with the energy landscape dynamics.

Second, we using a 2D model in the weak AIII/BDI topology class with topology-structure coupling, we have demonstrated the presence of flat zero-mode energy bands in the entire 1D Brillouin zone for states localized within TB/APB/OE. It has been found that the flatnesses of these bands and the slow group velocities for the localized zero-mode states could be controlled by the distance between the boundaries and the slow motion of the localized excitations can be guided through a zig-zag path. We propose our model can be realized in various metamaterials, which would open possibilities for unique device applications.

Third, we analyzed a model for topological mechanical metamaterials made of spinners interacting through magnets. The model serves as a test for topological electron Hamiltonian developed in Chapter 3. We showed how the results for electron system can be used to predict the results for mechanical system. We first studied 1D system with open edges and compared with the preliminary experimental data, which reveals consistency between theory and experiments, in particular the frequency and vibrational mode of edge modes. Encourages by the agreement, we carried out calculations for 2D systems, which correspond to 2D electron system studied in Chapter. 3, and made predictions. From the calculations, flat frequency bands are found in the bulk frequency band gap, localized at open edges of a ribbon. We calculated how the group velocity for these bands depend on the width of the ribbon, which can be compared with future experiments.

The significance of our work lies in the enhancement of our understanding how the structure of materials affect the electronic states or excitation modes. Our study on dynamics may help the development of energy efficient ultrafast switching devices. Our study on topological flat bands localized within boundaries could be used to trap photons and slow move along designed paths in photonic crystals. Our work on spinner systems showed the same phenomena could be found diverse metamaterials, where slowly moving localized state could be used for unique device applications.

In future, our dynamics work could be expanded to include other degrees of freedom, such as spin degrees of freedom. More realistic band structure could be incorporated into the tight-binding Hamiltonian, which would allow more quantitative comparison with experimental data. Our work on topological boundary modes with flat bands could be expanded to compare with experimental data, and geometry other than ribbons. The approach could be also expanded to other photonic, phononic, mechanical, sonic, water wave, and ultracold fermion systems, where the same topological arguments would predict the presence of topologically-protected flat energy bands localized within twin and antiphase boundaries and at open edges.

CHAPTER 6

CODE DEVELOPED FOR NUMERICAL CALCULATIONS

6.1 C++ Code for the Simulations of Photoinduced Nonequilibrium Dynamics in Charge Order Materials

Listing 6.1 An example of main codes used for the results in Chapter. 2

```
#include <stdio.h>
#include <math.h>
#define NN 512
#define Pi 3.14159265
#define PP 2801
void Set_Elk(double Elk[2][NN][NN], double kx[], double ky[],
              int N, double t, double lm, double u0)
{
    for(int i = 0; i < N; i++)
    {
        kx[i]=2*Pi/N*(i+1)-Pi;
    }
    for(int i = 0; i < N; i++)
    {
        ky[i]=2*Pi/N*(i+1)-Pi;
    }
    for(int q=0; q<2; q++)
    {
        for(int i=0; i<N; i++)
        {
```

```
            for(int j=0; j<N; j++)
            {
                Elk[q][i][j]=pow(-1,q)*sqrt(4*t*t*(cos(kx[i])
                             +cos(ky[j]))
                *(cos(kx[i])+cos(ky[j]))+lm*lm*u0*u0);
            }
        }
    }
}
void Set_Elkp(double Elkp[2][NN][NN], double kx[], double ky[],
       int N, double t, double lm, double u0)
{
    for(int i = 0; i < N; i++)
    {
        kx[i]=2*Pi/N*(i+1)-Pi;
    }
    for(int i = 0; i < N; i++)
    {
        ky[i]=2*Pi/N*(i+1)-Pi;
    }
    for(int q=0; q<2; q++)
    {
        for(int i=0; i<N; i++)
        {
            for(int j=0; j<N; j++)
            {
                Elkp[q][i][j]=pow(-1,q)*sqrt(4*t*t*(cos(kx[i])
```

```
                              +cos(ky[j]))
                *(cos(kx[i])+cos(ky[j]))+lm*lm*u0*u0);
            }
        }
    }
}
void give_print(double En[], double g[],
 double Dos[], int Ne, char *Str)
{
    FILE *fp=fopen(Str,"w");
    for(int i=0;i<Ne;i++)
    {
        if(Dos[i]!=0.0)
        {
            fprintf(fp,"%13.12f    %13.12f\n",En[i],g[i]);
        }
    }
    fclose(fp);
}

int main()
{
    int i,j,k,q,p,Np,N=NN,Nk=1500,Npt,Ne=2400,P=PP;
    int j1,j2,j3,j4,jmax,jmin;
    int Flag[Ne];
    double m,t,lm,K;
    double gm=0.009,gm0,gm3,gm4,eps;
```

```
    double kb=0.000086173324;
    double Emax,Emin,IDos[Ne],Dos[Ne],delE;
    double dt,Tt,Sum;
    double v0,v,w,w0,u00;
    double kx[N],ky[N];
    double Elk[2][NN][NN],En[Ne+1];
    double fe[Ne+1],fk[2][N][N],Elkp[2][NN][NN];
    double feold[Ne],fkold[2][N][N],f_r[Ne];
    double u0,u,u_eq,dn0;
    double d0,DE,W,dfmax,gee_const;
    double df[2][N][N];
    double T,Te,bw[500],x,y,z;
    double WD,Ep[500],Dpb[500],Dp[500],GM,Alf,Sp,gep[Ne],g[Ne];
    double gee[Ne],Kee,Kep;
    double dE2,dE1,dE0,Etot;
    double a,b;
    double dn,eve[NN][NN];
    double up,Eel0,Nlkupper,Nlklower,Neupper,Nelower;
    char *Str;
    char Name[12];
    double Eel,Eel_up,Eel_lo;
    FILE *fp,*fp2,*fp3,*fp1;

    initial_kx(kx,NN);
    initial_ky(ky,NN);
   m=0.0033212; dt=0.025; t=0.5; lm=1.2*0.78; K=0.85; DE=2.0;
    Kee=651.0*3.0; Kep=0.93*0.25; WD=0.1*0.6; GM=0.015; Npt=20;
```

```
T=132.601; W=0.02; dfmax=0.20; Te=kb*T;
eps=0.00001;
u0=0.031225504481243; v0=0.0;
u00=0.031225504481243; dn0=0.056712964098;
fp=fopen("/home/l/lz242/Dynamic_Window_Method/SaveData/
NN512_Ne2400_All_Distribution_k_ForSave.txt","rt+");
for(q=0;q<2;q++)
{
    for(i=0;i<N;i++)
    {
        for(j=0;j<N;j++)
        {
            fscanf(fp,"%lf\n",&fk[q][i][j]);
        }
    }
}
fclose(fp);
for(p=-1;p<P;p++)
{
    Tt=p*dt;
    Set_Elk(Elk,kx,ky,NN,t,lm,u0);
    if(p==0)
    {
        for(q=0;q<2;q++)
        {
            for(i=0;i<N;i++)
            {
```

```
            for(j=0;j<N;j++)
            {
                df[q][i][j]=pow(-1,q)*dfmax
                         *exp(-(Elk[q][i][j]
                -pow(-1,q)*DE/2)*(Elk[q][i][j]
                -pow(-1,q)*DE/2)/
                (2*W*W));
            }
        }
    }
    for(i=0;i<N;i++)
    {
        for(j=0;j<N;j++)
        {
            fk[0][i][j]+=df[0][i][j];
            fk[1][i][j]+=df[1][i][j];
        }
    }

}
Eel=0.0;
for(q=0;q<2;q++)
{
    for(i=0;i<N;i++)
    {
        for(j=0;j<N;j++)
        {
```

```
                Eel+=Elk[q][i][j]*fk[q][i][j]/(2*N*N);
            }
        }
    }
    Eel_lo=0.0;
    for(i=0;i<N;i++)
    {
        for(j=0;j<N;j++)
        {
            Eel_lo+=Elk[1][i][j]*fk[1][i][j]/(2*N*N);
        }
    }
    Nlkupper=0.0;
    for(i=0;i<N;i++)
    {
        for(j=0;j<N;j++)
        {
            Nlkupper+=fk[0][i][j]/(2*N*N);
        }
    }
    Nlklower=0.0;
    for(i=0;i<N;i++)
    {
        for(j=0;j<N;j++)
        {
            Nlklower+=fk[1][i][j]/(2*N*N);
        }
```

```
}

dn=0.0;
for(i=0;i<N;i++)
{
    for(j=0;j<N;j++)
    {
        eve[i][j]=-lm*u0*(2*t*(cos(kx[i])+cos(ky[j]))
        +Elk[0][i][j])/
        (8*t*t*(cos(kx[i])+cos(ky[j]))*(cos(kx[i])
        +cos(ky[j]))
        +2*lm*lm*u0*u0+4*t*Elk[0][i][j]*(cos(kx[i])
        +cos(ky[j])))*fk[0][i][j]
        -lm*u0*(2*t*(cos(kx[i])+cos(ky[j]))
        -Elk[0][i][j])/
        (8*t*t*(cos(kx[i])+cos(ky[j]))
        *(cos(kx[i])+cos(ky[j]))
        +2*lm*lm*u0*u0-4*t*(cos(kx[i])
        =cos(ky[j]))*Elk[0][i][j])*fk[1][i][j];
    }
}
for(i=0;i<N;i++)
{
    for(j=0;j<N;j++)
    {
        dn+=eve[i][j]/(N*N);
    }
```

```
    }
    dE0=0.0;
    for(i=0;i<N;i++)
    {
        for(j=0;j<N;j++)
        {
            dE0+=lm*lm*u0/Elk[0][i][j]*fk[0][i][j]
            -lm*lm*u0/Elk[0][i][j]*fk[1][i][j];
        }
    }
    dE1=2*K*u0+dE0/N/N/2;
    dE0=0.0;
    for(i=0;i<N;i++)
    {
        for(j=0;j<N;j++)
        {
            dE0+=(lm*lm*Elk[0][i][j]-lm*lm*lm*lm*u0*u0
            /Elk[0][i][j])/
            (4*t*t*(cos(kx[i])+cos(ky[j]))*(cos(kx[i])
            +cos(ky[j]))+lm*lm*u0*u0)
            *(fk[0][i][j]-fk[1][i][j]);
        }
    }
    dE2=2*K+dE0/N/N/2;
    a=dE2;
    b=dE1-a*u0;
    u_eq=-b/a;
```

```
    d0=gm*gm/(4*m*m)-2.0*a/m;
    if(d0<0.0)
    {
        w0=sqrt(a/2/m);
        gm0=gm/4/m;
        w=sqrt(w0*w0-gm0*gm0);
        u=sin(w*dt)/w*exp(-gm0*dt)*v0+(gm0/w*sin(w*dt)
        +cos(w*dt))*exp(-gm0*dt)*(u0-u_eq)+u_eq;
        v=(-gm0/w*sin(w*dt)+cos(w*dt))*exp(-gm0*dt)*v0
        -(gm0*gm0/w+w)*exp(-gm0*dt)*sin(w*dt)*(u0-u_eq);
    }
    if(d0==0.0)
    {
        w0=sqrt(a/2/m);
        gm0=gm/4/m;
        u=exp(-gm0*dt)*(1+gm0*dt)*(u0-u_eq)+exp(-gm0*dt)
        *v0*dt+u_eq;
        v=-gm0*gm0*dt*exp(-gm0*dt)*(u0-u_eq)+(1-gm0*dt)
        *exp(-gm0*dt)*v0;
    }
    if(d0>0.0)
    {
        gm3=-gm/4/m+sqrt(gm*gm-4*a*2*m)/4/m;
        gm4=-gm/4/m-sqrt(gm*gm-4*a*2*m)/4/m;
        u=(-gm4/(gm3-gm4)*(u0-u_eq)+1/(gm3-gm4)*v0)
        *exp(gm3*dt)
        +(gm3/(gm3-gm4)*(u0-u_eq)-1/(gm3-gm4)*v0)
```

```
            *exp(gm4*dt)+u_eq;
            v=(-gm3*gm4/(gm3-gm4)*(u0-u_eq)+gm3/(gm3-gm4)
            *v0)*exp(gm3*dt)
            +(gm3*gm4/(gm3-gm4)*(u0-u_eq)-gm4/(gm3-gm4)
            *v0)*exp(gm4*dt);
        }
        Emax=sqrt(16*t*t+lm*lm*u0*u0);                                  /*Density
        Emin=-Emax;
        delE=(Emax-Emin)/(Ne-1);
        Np=int(WD/delE);
        for(k=0;k<Np;k++)
        {
            Ep[k]=delE*(k+1);
            Dpb[k]=Ep[k]*Ep[k];
        }
        for(k=Np;k<Np+Npt;k++)
        {
            Ep[k]=delE*(k+1);
            Dpb[k]=WD*WD*exp(-(Ep[k]-WD)*(Ep[k]-WD)/(2*GM*GM));
        }
        Sp=0.0;
        for(k=0;k<Np+Npt;k++)
        {
            Sp+=Dpb[k]*delE;
        }
        Alf=5.0/Sp;

```

```
        for(k=0;k<Np;k++)
        {
                Dp[k]=Alf*Ep[k]*Ep[k];
        }
        for(k=Np;k<Np+Npt;k++)
        {
                Dp[k]=Alf*WD*WD*exp(-(Ep[k]-WD)*(Ep[k]-WD)/(2*GM*GM));
        }
          for(k=0;k<Np+Npt;k++)
          {
         Sum+=Dp[k]*delE;
          }
        for(k=0;k<Ne;k++)
        {
                //En[k]=Emin+k*delE-0.5*delE;
                En[k]=Emin+k*delE;
        }
        for(i=0;i<Ne;i++)
        {
                IDos[i]=0.0;
        }
        for(q=0;q<2;q++)
        {
                for(i=0;i<N;i++)
                {
                        for(j=0;j<N;j++)
                        {
```

```
                k=int((Elk[q][i][j]-Emin+0.5*delE)/delE);
                IDos[k]+=1/delE;
            }
        }
    }
    for(k=0;k<Ne;k++)
    {
        Dos[k]=IDos[k]/(2*N*N);
    }
    for(i=0;i<Ne;i++)
    {
        fe[i]=0.0;
    }
    for(q=0;q<2;q++)
    {
        for(i=0;i<N;i++)
        {
            for(j=0;j<N;j++)
            {
                k=int((Elk[q][i][j]-Emin+0.5*delE)/delE);
                fe[k]+=fk[q][i][j]/(Dos[k]*N*N*delE)/2;
            }
        }
    }

    Eel_lo=0.0;
    for(i=0;i<Ne/2;i++)
```

```
        {
            Eel_lo+=En[i]*fe[i]*Dos[i]*delE;
        }
        Eel_up=0.0;
        for(i=Ne/2;i<Ne;i++)
        {
            Eel_up+=En[i]*fe[i]*Dos[i]*delE;
        }
        Nelower=0.0;
        for(i=0;i<Ne/2;i++)
        {
            Nelower+=fe[i]*Dos[i]*delE;
        }
        Neupper=0.0;
        for(i=Ne/2;i<Ne;i++)
        {
            Neupper+=fe[i]*Dos[i]*delE;
        }
        i=0;
        while(i<Ne)
        {
            i++;
            jmin=i;
            if(Dos[i]!=0.0 && fabs(1.00-fe[i])>eps)
                break;
        }
        jmax=Ne-jmin-1;
```

```
for(i=0;i<Np+Npt;i++)
{
    bw[i]=1.0/(exp(Ep[i]/Te)-1.0);
}
for(i=0;i<Ne;i++)
{
    if(Dos[i]<0.000000000000001)
        Flag[i] = 0;
    else
        Flag[i] = 1;
}
for(i=0;i<Ne;i++)
{
    g[i]=0.0;
    gee[i]=0.0;
    gep[i]=0.0;
}
gee_const = delE * delE * Kee * 0.5;
for(j1=jmin;j1<jmax+1;j1++)
{
    for(j2=jmin;j2<jmax+1;j2++)
    {
        for(j3=jmin;j3<jmax+1;j3++)
        {
            j4 = j1 + j3 - j2;
            if (j4>=jmin&&j4<jmax+1)
            {
```

```
                    if (j1==j2||j1==j4) continue;
                    if (Flag[j1]==1 && Flag[j2]==1
                     && Flag[j3]==1 && Flag[j4]==1)
                    {
                        gee[j1]+=gee_const*Dos[j2]
                        *Dos[j3]*Dos[j4]
                        *(fe[j1]*fe[j3]*
                        (fe[j2]+fe[j4]-1.0) -fe[j2]
                        *fe[j4]*(fe[j1]+fe[j3]-1.0));
                    }
                }
            }
        }
    }
    for(k=0;k<Np+Npt;k++)
    {
        for(i=jmin;i<jmax+1;i++)
        {
            j=i+k+1;
            if(j<jmax+1&&Flag[i]==1&&Flag[j]==1)
            {
                y=fe[i]*(1-fe[j])*bw[k];
                x=fe[j]*(1-fe[i])*(bw[k]+1);
                z=x-y;
                gep[i]+=Kep*z*Dos[j]*Dp[k]*delE;
                gep[j]+=-Kep*z*Dos[i]*Dp[k]*delE;
            }
```

```
        }
    }
    for(i=0;i<Ne;i++)
    {
        g[i]=gee[i]+gep[i];
    }
    for(i=0;i<Ne;i++)
    {
        fe[i]+=g[i]*dt;
    }

    for(q=0;q<2;q++)
    {
        for(i=0;i<N;i++)
        {
            for(j=0;j<N;j++)
            {
                k=int((Elk[q][i][j]-Emin+0.5*delE)/delE);
                fk[q][i][j]=fe[k];
            }
        }
    }
    u0=u;
    v0=v;
}
Str="New_Distribution_E.txt";
give_print(En,fe,Dos,Ne,Str);
```

```
    return(0);
}
```

6.2 Fortran Code for Calculation of Electronic States in Model Topological Insulators

Listing 6.2 An example of main codes used for the results in Chapter 3

```
PROGRAM Hamiltion

  IMPLICIT NONE
  INTEGER N,NT,m,NEMAX,SITEMAX,EFMAX,My
  REAL*8 EPS,PI
  PARAMETER(N=32)
  PARAMETER(NT=N*N)
  PARAMETER(m=NT*4)
  PARAMETER(My=32)
  PARAMETER(PI=3.1415926)
  PARAMETER(NEMAX=1000)
  PARAMETER(SITEMAX=10)
  PARAMETER(EFMAX=5)

  INTEGER ix,iy,it,itx,ity,ixx,iyy,ny,nE,j,i,itt,j0,i0,j00,i00
  INTEGER iwork(NT),ierr,modeD,matz
  REAL*8 Dde(N,N),Dda(N,N),Dy
  DOUBLE COMPLEX ab(N),ac(N),bb(N),bc(N),cb(N),cc(N)
  REAL*8 dx,ky
  REAL*8 e(N),d(N),Ddx(N),Ddy(N)
```

```
  REAL*8 HI(2*N,2*N),HR(2*N,2*N),wr(2*N),wi(2*N),zr(2*N,2*N),
           zi(2*N,2*N),vr(N,N),vi(N,N),kyy(My)
  REAL*8 fv1(2*N),fv2(2*N),fv3(2*N)
  DOUBLE COMPLEX H(2*N,2*N), ini
  REAL*8 t0,alp,Emin

!---- Read in input
!---- Read in input
  open(50,file=’fle.in’,status=”unknown”)
  read(50,*) t0
  read(50,*) alp
  read(50,*) Emin
  read(50,*) nE
  read(50,*) modeD
  close(50)
!---- Write parameters
 write(10,*) ’modeD=’,modeD
!---- Read in and set Ddx and Ddy
 if(modeD.eq.100)
 open(51,file=’tiw.100.0.DdxDdy’,status=”unknown”)
 if(modeD.eq.101)
 open(51,file=’tiw.100.1.DdxDdy’,status=”unknown”)
 if(modeD.eq.102)
 open(51,file=’tiw.100.2.DdxDdy’,status=”unknown”)
 if(modeD.eq.103)
 open(51,file=’tiw.100.3.DdxDdy’,status=”unknown”)
 if(modeD.eq.104)
```

```
 open(51,file='tiw.100.4.DdxDdy',status="unknown")
 do ix=1,N
    read(51,*) Ddx(ix),Ddy(ix)
 end do
 close(51)
!---- Set d(iy) and e(iy)
  do ix=1,N
     e(ix)=Ddy(ix)
  end do

  do ix=1,N
      d(ix)=(Ddx(ix)+Ddy(ix))*(-1.d0)**ix
  end do
!---- Set and write ab ac b and c
  do ny=(-My/2+1),(My/2)
     kyy(ny)=(ny*1.d0/(My*1.d0))*2.d0*PI
     ky=kyy(ny)
     do ix=1,N
        ab(ix)=-(1-e(ix))*(1+CMPLX(COS(ky),-SIN(ky)))
        ac(ix)=-(1-e(ix))*(1+CMPLX(COS(ky),SIN(ky)))
        bb(ix)=-(1+e(ix))*(1+d(ix))*CMPLX(COS(ky),-SIN(ky))
        bc(ix)=-(1+e(ix))*(1-d(ix))
        cb(ix)=-(1+e(ix))*(1-d(ix))
        cc(ix)=-(1+e(ix))*(1+d(ix))*CMPLX(COS(ky),SIN(ky))
     end do
!---- Construct the Hamiltion matrix
     ini = CMPLX(0,0)
```

```
do i=1,2*N
   do j=1,2*N
      H(i,j)=ini
   end do
end do
do i=1,2*N
   do j=1,2*N
      i0=int((i+1)/2)
      j0=int((j+1)/2)
      if(i0.eq.j0) then
         if((i+1).eq.j) then
             H(i,j)=ab(i0)
         else if((j+1).eq.i) then
             H(i,j)=ac(i0)
         end if
       end if
       if((i0+1).eq.j0) then
           if((i+1).eq.j) then
               H(i,j)=bc(i0)
           else if((i+3).eq.j) then
               H(i,j)=bb(i0)
           end if
       end if
       if((j0+1).eq.i0) then
           if((j+1).eq.i) then
               H(i,j)=cb(j0)
           else if((j+3).eq.i) then
```

```
              H(i,j)=cc(j0)
          end if
      end if
      if(i.eq.1) then
         if(j.eq.(2*N)) then
             H(i,j)=cb(N)
         end if
      end if
      if(i.eq.2) then
         if(j.eq.(2*N-1)) then
            H(i,j)=cc(N)
         end if
      end if
      if(i.eq.(2*N-1)) then
         if(j.eq.2) then
            H(i,j)=bb(N)
         end if
      end if
     if(i.eq.(2*N)) then
         if(j.eq.1) then
             H(i,j)=bc(N)
         end if
     end if
  end do
end do
do i=1,2*N
   do j=1,2*N
```

```
            HR(i,j)=REAL(H(i,j))
            HI(i,j)=AIMAG(H(i,j))
         end do
      end do

!----- Find eigensystems of the matrix
      call cg(2*N,2*N,HR,HI,wr,wi,1,zr,zi,fv1,fv2,fv3,ierr)
!----- Write eigenvector magnitude
     call quicksort(wr, 1, 2*N)
     do it=1,N*2
        write(18,*) ky, wr(it)
     end do
  end do
   END PROGRAM Hamiltion
```

6.3 Fortran Code for Calculation of Flat Frequency Bands at Open Edges of 2D Spinner Systems

Listing 6.3 An example of main codes used for the results in Chapter 4

```
PROGRAM Hamiltion

  IMPLICIT NONE

  INTEGER N,NT,m,NEMAX,SITEMAX,EFMAX,My,N1,N2,Ns

  REAL*8 EPS,PI

```

```
PARAMETER(N=12)
PARAMETER(NT=N*N)
PARAMETER(m=NT*4)
PARAMETER(My=32)
PARAMETER(N1=N)
PARAMETER(N2=2*N+1)
PARAMETER(Ns=N2+2*N1)

PARAMETER(PI=3.1415926)
PARAMETER(NEMAX=1000)
PARAMETER(SITEMAX=10)
PARAMETER(EFMAX=5)

INTEGER ix,iy,it,itx,ity,ixx,iyy,im,imm,j,i,itt,i0,j0
INTEGER iwork(NT),ierr,modeD,matz
INTEGER m1,m2,q1,q2,nx,ny
INTEGER xsA,ysA,xsB,ysB,xA,yA,xB,yB
REAL*8 Nr,dx,dy,e
DOUBLE COMPLEX ab(N),ac(N),b(N),c(N)
DOUBLE COMPLEX Vn(2*N),Valp(N),Vbeta(N),PsiA(N1,N2),
 PsiB(N1,N2),Phi(N2+2*N1,N2+2*N1)
REAL*8 alp,betaR,betaB,betaG,betaY,ky,k2,kyy(My)
REAL*8 HI(2*N,2*N),HR(2*N,2*N),wr(2*N),wi(2*N),zr(2*N,2*N),
 zi(2*N,2*N),vr(N,N),vi(N,N)
REAL*8 fv1(2*N),fv2(2*N),fv3(2*N)
REAL*8 PhiR(N2+2*N1,N2+2*N1),PhiI(N2+2*N1,N2+2*N1)
DOUBLE COMPLEX H(2*N,2*N),ini
```

```
  REAL*8 locdos(N2+2*N1,N2+2*N1),Ew,Ewm,WF(N2+2*N1,N2+2*N1),
  tlocdos(N2+2*N1,N2+2*N1)

  Ew=750.0+2.0
  Ewm=750.0-2.0
!----- Set N1 and N2
  Nr=N2*1.d0
!----- Set alp and bat
   alp=750.0d0
   betaR=250.0d0
   betaB=150.0d0
   betaG=120.0d0
   betaY=120.0d0
!----- Set and write ab ac b and c
locdos=0.d0
do ny=1,My
    kyy(ny)=((ny*1.d0-16.d0)/(16.d0))*PI
    ky=kyy(ny)
    k2=ky
  do ix=1,N
     ab(ix)=-betaB-betaG*CMPLX(COS(k2),SIN(k2))
     ac(ix)=-betaB-betaG*CMPLX(COS(k2),-SIN(k2))
     b(ix)=-betaY*CMPLX(COS(k2),SIN(k2))-betaR
     c(ix)=-betaY*CMPLX(COS(k2),-SIN(k2))-betaR
  end do
!----- Construct the Hamiltion matrix
  ini = CMPLX(0,0)
```

```fortran
do i=1,2*N
   do j=1,2*N
      H(i,j)=ini
   end do
end do
do i=1,2*N
   do j=1,2*N
      i0=int((i+1)/2)
      j0=int((j+1)/2)

      if(i.eq.j) then
        H(i,j)=alp
      end if

      if(i0.eq.j0) then
          if((i+1).eq.j) then
              H(i,j)=ab(i0)
          else if((j+1).eq.i) then
              H(i,j)=ac(i0)
          end if
      end if
      if((i0+1).eq.j0) then
          if((i+1).eq.j) then
             H(i,j)=b(i0)
          end if
       end if

```

```
            if((j0+1).eq.i0) then
                if((j+1).eq.i) then
                        H(i,j)=c(j0)
                end if
            end if

        end do
    end do
    do i=1,2*N
        do j=1,2*N
            HR(i,j)=REAL(H(i,j))
            HI(i,j)=AIMAG(H(i,j))
        end do
    end do

!—— Find eigensystems of the matrix
    call cg(2*N,2*N,HR,HI,wr,wi,1,zr,zi,fv1,fv2,fv3,ierr)
    do it=1,N*2
        write(16,*) ky, wr(it)
    end do
    do it=1,N*2
        write(18,*) ky, sqrt(wr(it))
    end do
    do m1=1,Ns
        do m2=1,Ns
            Phi(m1,m2)=ini
        end do
```

```
end do
do im=1,2*N
   if((wr(im).lt.Ew).and.(wr(im).gt.Ewm)) then
      write(40,*) im, wr(im)

      do it=1,2*N
          Vn(it)=CMPLX(zr(it,im),zi(it,im))
      end do

      do it=1,N
         Valp(it)=Vn(2*it-1)
         Vbeta(it)=Vn(2*it)
      end do

      do m1=1,N1
         do m2=1,N2
            PsiA(m1,m2)=(1.d0/SQRT(Nr))*Valp(m1)*
                        CMPLX(COS(k2*m2),SIN(k2*m2))
            PsiB(m1,m2)=(1.d0/SQRT(Nr))*Vbeta(m1)*
                        CMPLX(COS(k2*m2),SIN(k2*m2))
         end do
      end do

      do m1=1,N1
         do m2=1,N2
            xA=2*m1-m2
            yA=m2
```

```

                xB=2*m1-m2+1
                yB=m2

                xsA=xA+N2
                ysA=yA

                xsB=xB+N2
                ysB=yB

                Phi(xsA,ysA)=PsiA(m1,m2)
                Phi(xsB,ysB)=PsiB(m1,m2)

                write(50,*) m1,m2,xA,yA,xB,yB,xsA,ysA,xsB,ysB
            end do
        end do
        do m1=1,(N2+2*N1)
            do m2=1,(N2+2*N1)
                PhiR(m1,m2)=REAL(Phi(m1,m2))
                PhiI(m1,m2)=AIMAG(Phi(m1,m2))
                WF(m1,m2)=PhiR(m1,m2)**2+PhiI(m1,m2)**2
                locdos(m1,m2)=locdos(m1,m2)+WF(m1,m2)
                tlocdos(m1,m2)=locdos(m1,m2)*(-1)**(m1+m2)
            end do
        end do

    end if
```

```
    end do
end do
do j=Ns,1,-1
    do i=1,Ns
        write(100,*) locdos(i,j)
        write(101,*) tlocdos(i,j)
    end do
end do
do i=1,Ns
    do j=1,Ns
        write(10,*) i, j, 0.0, 0.0
    end do
end do
!------------------------------------------------------------------------

END PROGRAM Hamiltion
```

BIBLIOGRAPHY

[1] K. H. Ahn, M. J. Graf, S. A. Trugman, J. Demsar, R. D. Averitt, J. L. Sarrao, and A. J. Taylor. Ultrafast quasiparticle relaxation dynamics in normal metals and heavy-fermion materials. *Physical Review B*, 69:045114, Jan 2004.

[2] K. H. Ahn, T. Lookman, and A. R. Bishop. *Nature (London)*, 428:401, 2004.

[3] K. H. Ahn, T. Lookman, A. Saxena, and A. R. Bishop. *Physical Review B*, 68:092101, 2003.

[4] K. H. Ahn, T. Lookman, A. Saxena, and A. R. Bishop. Electronic properties of structural twin and antiphase boundaries in materials with strong electron-lattice couplings. *Physical Review B*, 71:212102, 2005.

[5] K. H. Ahn and A. J. Millis. Effects of magnetic ordering on the anisotropy and temperature dependence of the optical conductivity in lamno_3 : a tight-binding approach. *Physical Review B*, 61:13545–13559, May 2000.

[6] K. H. Ahn and A. J. Millis. Effects of uniaxial strain in lamno_3. *Physical Review B*, 64:115103, Aug 2001.

[7] K. H. Ahn, T. F. Seman, T. Lookman, and A. R. Bishop. Role of complex energy landscapes and strains in multiscale inhomogeneities in perovskite manganites. *Physical Review B*, 88:144415, 2013.

[8] P. B. Allen. Theory of thermal relaxation of electrons in metals. *Physical Review Letters*, 59:1460–1463, Sep 1987.

[9] D. Apigo, C. Prodan, and E. Prodan. Topological patterns. *arXiv preprint arXiv:1803.00984*, 2018.

[10] J. K. Asbóth, L. Oroszlány, and A. Pályi. *A Short Course on Topological Insulators.* Springer, New York, 2015.

[11] P. Baum, D.-S. Yang, and A. H. Zewail. 4d visualization of transitional structures in phase transformations by electron diffraction. *Science*, 318(5851):788–792, 2007.

[12] P. Beaud, A. Caviezel, S. O. Mariager, L. Rettig, G. Ingold, C. Dornes, S.-W. Huang, J. A. Johnson, M. Radovic, T. Huber, T. Kubacka, A. Ferrer, H. T. Lemke, M. Chollet, D. Zhu, J. M. Glownia, M. Sikorski, A. Robert, H. Wadati, M. Nakamura, M. Kawasaki, Y. Tokura, S. L. Johnson, and U. Staub. A time-dependent order parameter for ultrafast photoinduced phase transitions. *Nat. Mater.*, 13:923–927, Oct 2014.

[13] K.-H. Bennemann and J. B. Ketterson. *Superconductivity: Volume 1: Conventional and Unconventional Superconductors Volume 2: Novel Superconductors*. Springer Science & Business Media, 2008.

[14] A. Cavalleri, T. Dekorsy, H. H. Chong, J.-C. Kieffer, and R. W. Schoenlein. Evidence for a structurally-driven insulator-to-metal transition in vo 2: A view from the ultrafast timescale. *Physical Review B*, 70(16):161102, 2004.

[15] A. Cavalleri, M. Rini, H. Chong, S. Fourmaux, T. Glover, P. Heimann, J. Kieffer, and R. Schoenlein. Band-selective measurements of electron dynamics in vo 2 using femtosecond near-edge x-ray absorption. *Physical Review Letters*, 95(6):067405, 2005.

[16] A. Cavalleri, C. Tóth, C. W. Siders, J. Squier, F. Ráksi, P. Forget, and J. Kieffer. Femtosecond structural dynamics in vo 2 during an ultrafast solid-solid phase transition. *Physical Review Letters*, 87(23):237401, 2001.

[17] A. D. Caviglia, M. Först, R. Scherwitzl, V. Khanna, H. Bromberger, R. Mankowsky, R. Singla, Y.-D. Chuang, W. S. Lee, O. Krupin, W. F. Schlotter, J. J. Turner, G. L. Dakovski, M. P. Minitti, J. Robinson, V. Scagnoli, S. B. Wilkins, S. A. Cavill, M. Gibert, S. Gariglio, P. Zubko, J.-M. Triscone, J. P. Hill, S. S. Dhesi, and A. Cavalleri. Photoinduced melting of magnetic order in the correlated electron insulator ndnio_3. *Physical Review B*, 88:220401, Dec 2013.

[18] F. Cilento, C. Giannetti, G. Ferrini, S. D. Conte, T. Sala, G. Coslovich, M. Rini, A. Cavalleri, and F. Parmigiani. Ultrafast insulator-to-metal phase transition as a switch to measure the spectrogram of a supercontinuum light pulse. *Appl. Phys. Lett.*, 96(2):021102, 2010.

[19] E. Dagotto. Open questions in cmr manganites, relevance of clustered states and analogies with other compounds including the cuprates. *New Journal of Physics*, 7(1):67, 2005.

[20] E. Dagotto, T. Hotta, and A. Moreo. Colossal magnetoresistant materials: the key role of phase separation. *Physics reports*, 344(1-3):1–153, 2001.

[21] J. Demsar, R. D. Averitt, K. H. Ahn, M. J. Graf, S. A. Trugman, V. V. Kabanov, J. L. Sarrao, and A. J. Taylor. Quasiparticle relaxation dynamics in heavy fermion compounds. *Physical Review Letters*, 91:027401, Jul 2003.

[22] J. Demsar, K. Biljaković, and D. Mihailovic. Single particle and collective excitations in the one-dimensional charge density wave solid $\mathrm{k}_{0.3}\mathrm{moo}_3$ probed in real time by femtosecond spectroscopy. *Physical Review Letters*, 83:800–803, Jul 1999.

[23] V. Esposito, M. Fechner, R. Mankowsky, H. Lemke, M. Chollet, J. M. Glownia, M. Nakamura, M. Kawasaki, Y. Tokura, U. Staub, P. Beaud, and M. Först. Nonlinear electron-phonon coupling in doped manganites. *Physical Review Letters*, 118:247601, Jun 2017.

[24] D. Fausti, R. Tobey, N. Dean, S. Kaiser, A. Dienst, M. C. Hoffmann, S. Pyon, T. Takayama, H. Takagi, and A. Cavalleri. Light-induced superconductivity in a stripe-ordered cuprate. *science*, 331(6014):189–191, 2011.

[25] R. H. M. Groeneveld, R. Sprik, and A. Lagendijk. Effect of a nonthermal electron distribution on the electron-phonon energy relaxation process in noble metals. *Physical Review B*, 45:5079–5082, Mar 1992.

[26] R. H. M. Groeneveld, R. Sprik, and A. Lagendijk. Femtosecond spectroscopy of electron-electron and electron-phonon energy relaxation in ag and au. *Physical Review B*, 51:11433–11445, May 1995.

[27] G. Grüner. *Density Waves in Solids.* Addison-Wesley Publishing Company, Los Angeles, 1994.

[28] F. D. M. Haldane. Model for a quantum hall effect without landau levels: Condensed-matter realization of the" parity anomaly". *Physical Review Letters*, 61(18):2015, 1988.

[29] T.-R. T. Han, Z. Tao, S. D. Mahanti, K. Chang, C.-Y. Ruan, C. D. Malliakas, and M. G. Kanatzidis. Structural dynamics of two-dimensional charge-density waves in cete$_3$ investigated by ultrafast electron crystallography. *Physical Review B*, 86:075145, Aug 2012.

[30] T.-R. T. Han, F. Zhou, C. D. Malliakas, P. M. Duxbury, S. D. Mahanti, M. G. Kanatzidis, and C.-Y. Ruan. Exploration of metastability and hidden phases in correlated electron crystals visualized by femtosecond optical doping and electron crystallography. *Sci. Adv.*, 1:e1400173, 2015.

[31] A. J. Heeger, S. Kivelson, J. R. Schrieffer, and W. P. Su. *Rev. Mod. Phys.*, 60:781, 1988.

[32] D. Hilton, R. Prasankumar, S. Fourmaux, A. Cavalleri, D. Brassard, M. El Khakani, J. Kieffer, A. Taylor, and R. Averitt. Enhanced photosusceptibility near t c for the light-induced insulator-to-metal phase transition in vanadium dioxide. *Physical review letters*, 99(22):226401, 2007.

[33] H. Ichikawa, S. Nozawa, T. Sato, A. Tomita, K. Ichiyanagi, M. Chollet, L. Guerin, N. Dean, A. Cavalleri, S.-i. Adachi, et al. Transient photoinduced ?hidden?phase in a manganite. *Nature materials*, 10(2):101, 2011.

[34] G. Jotzu, M. Messer, R. Desbuquois, M. Lebrat, T. Uehlinger, D. Greif, and T. Esslinger. Experimental realization of the topological haldane model with ultracold fermions. *Nature*, 515(7526):237, 2014.

[35] V. V. Kabanov and A. S. Alexandrov. Electron relaxation in metals: Theory and exact analytical solutions. *Physical Review B*, 78:174514, Nov 2008.

[36] D. M. Kennes, E. Y. Wilner, D. R. Reichman, and A. J. Millis. Transient superconductivity from electronic squeezing of optically pumped phonons. *Nat. Phys.*, 13:479–483, May 2017.

[37] H.-T. Kim, Y. W. Lee, B.-J. Kim, B.-G. Chae, S. J. Yun, K.-Y. Kang, K.-J. Han, K.-J. Yee, and Y.-S. Lim. Monoclinic and correlated metal phase in vo 2 as evidence of the mott transition: coherent phonon analysis. *Physical Review Letters*, 97(26):266401, 2006.

[38] C. Kübler, H. Ehrke, R. Huber, R. Lopez, A. Halabica, R. Haglund Jr, and A. Leitenstorfer. Coherent structural dynamics and electronic correlations during an ultrafast insulator-to-metal phase transition in vo 2. *Physical Review Letters*, 99(11):116401, 2007.

[39] L.-J. Lang, X. Cai, and S. Chen. Edge states and topological phases in one-dimensional optical superlattices. *Physical Review Letters*, 108:220401, 2012.

[40] L. Li and M. A. Araújo. Topological insulating phases from two-dimensional nodal loop semimetals. *Physical Review B*, 94(16):165117, 2016.

[41] L. Li, Z. Xu, and S. Chen. Topological phases of generalized su-schrieffer-heeger models. *Physical Review B*, 89:085111, 2014.

[42] D. Lim, V. Thorsmølle, R. Averitt, Q. Jia, K. Ahn, M. Graf, S. Trugman, and A. Taylor. Coherent optical and acoustic phonon generation correlated with the charge-ordering phase transition in la 1- x ca x mno 3. *Physical Review B*, 71(13):134403, 2005.

[43] A. Lindenberg, I. Kang, S. L. Johnson, T. Missalla, P. Heimann, Z. Chang, J. Larsson, P. Bucksbaum, H. Kapteyn, H. Padmore, et al. Time-resolved x-ray diffraction from coherent phonons during a laser-induced phase transition. *Physical Review Letters*, 84(1):111, 2000.

[44] K. Liu, X. Wu, K. Ahn, T. Sulchek, C. Chien, and J. Q. Xiao. Charge ordering and magnetoresistance in nd 1- x ca x mno 3 due to reduced double exchange. *Physical Review B*, 54(5):3007, 1996.

[45] M. Liu, H. Y. Hwang, H. Tao, A. C. Strikwerda, K. Fan, G. R. Keiser, A. J. Sternbach, K. G. West, S. Kittiwatanakul, J. Lu, et al. Terahertz-field-induced insulator-to-metal transition in vanadium dioxide metamaterial. *Nature*, 487(7407):345, 2012.

[46] J. Lu, C. Qiu, L. Ye, X. Fan, M. Ke, F. Zhang, and Z. Liu. Observation of topological valley transport of sound in sonic crystals. *Nat. Phys.*, 13(4):369, 2017.

[47] R. Mankowsky, M. Först, T. Loew, J. Porras, B. Keimer, and A. Cavalleri. Coherent modulation of the $\mathrm{YBa_2Cu_3o_{6+x}}$ atomic structure by displacive stimulated ionic raman scattering. *Physical Review B*, 91:094308, Mar 2015.

[48] M. Matsubara, Y. Okimoto, T. Ogasawara, Y. Tomioka, H. Okamoto, and Y. Tokura. Ultrafast photoinduced ferromagnetism in the perovskite manganite gd0.55sr0.45mno3. *J. Appl. Phys.*, 103(7):07B110, 2008.

[49] E. J. Meier, F. A. An, and B. Gadway. Observation of the topological soliton state in the su–schrieffer–heeger model. *Nat. Commun.*, 7:13986, 2016.

[50] S. Miyasaka, J. Fujioka, M. Iwama, Y. Okimoto, and Y. Tokura. Raman study of spin and orbital order and excitations in perovskite-type r vo 3 (r= la, nd, and y). *Physical Review B*, 73(22):224436, 2006.

[51] S. Miyasaka, Y. Okimoto, M. Iwama, and Y. Tokura. Spin-orbital phase diagram of perovskite-type r vo 3 (r= rare-earth ion or y). *Physical Review B*, 68(10):100406, 2003.

[52] B. Moritz, A. F. Kemper, M. Sentef, T. P. Devereaux, and J. K. Freericks. Electron-mediated relaxation following ultrafast pumping of strongly correlated materials: Model evidence of a correlation-tuned crossover between thermal and nonthermal states. *Physical Review Letters*, 111:077401, Aug 2013.

[53] Y. Okimoto, X. Peng, M. Tamura, T. Morita, K. Onda, T. Ishikawa, S. Koshihara, N. Todoroki, T. Kyomen, and M. Itoh. Ultrasonic propagation of a metallic domain in pr 0.5 ca 0.5 coo 3 undergoing a photoinduced insulator-metal transition. *Physical Review Letters*, 103(2):027402, 2009.

[54] A. M. Oles. Charge and orbital order in transition metal oxides. *arXiv preprint arXiv:1008.2515*, 2010.

[55] R. K. Pal and M. Ruzzene. Edge waves in plates with resonators: an elastic analogue of the quantum valley hall effect. *New J. Phys.*, 19(2):025001, 2017.

[56] A. Pashkin, C. Kübler, H. Ehrke, R. Lopez, A. Halabica, R. Haglund Jr, R. Huber, and A. Leitenstorfer. Ultrafast insulator-metal phase transition in vo 2 studied by multiterahertz spectroscopy. *Physical Review B*, 83(19):195120, 2011.

[57] L. Piazza, C. Ma, H. X. Yang, A. Mann, Y. Zhu, J. Q. Li, and F. Carbone. Ultrafast structural and electronic dynamics of the metallic phase in a layered manganite. *Struct. Dyn.*, 1:014501, 2014.

[58] K. Qian, D. J. Apigo, C. Prodan, Y. Barlas, and E. Prodan. Theory and experimental investigation of the quantum valley hall effect. *arXiv:1803.08781.*

[59] B. Rethfeld, A. Kaiser, M. Vicanek, and G. Simon. Ultrafast dynamics of nonequilibrium electrons in metals under femtosecond laser irradiation. *Physical Review B*, 65:214303, May 2002.

[60] M. Rini, A. Cavalleri, R. W. Schoenlein, R. López, L. C. Feldman, R. F. Haglund, L. A. Boatner, and T. E. Haynes. Photoinduced phase transition in vo 2 nanocrystals: ultrafast control of surface-plasmon resonance. *Optics letters*, 30(5):558–560, 2005.

[61] M. Rini, N. Dean, J. Itatani, Y. Tomioka, Y. Tokura, R. W. Schoenlein, A. Cavalleri, et al. Control of the electronic phase of a manganite by mode-selective vibrational excitation. *Nature*, 449(7158):72, 2007.

[62] T. Rohwer, S. Hellmann, M. Wiesenmayer, C. Sohrt, A. Stange, B. Slomski, A. Carr, Y. Liu, L. M. Avila, M. Kallane, S. Mathias, L. Kipp, K. Rossnagel, and M. Bauer. Collapse of long-range charge order tracked by time-resolved photoemission at high momenta. *Nature (London)*, 471:490–493, Mar 2011.

[63] K. Rossnagel. On the origin of charge-density waves in select layered transition-metal dichalcogenides. *Journal of Physics: Condensed Matter*, 23(21):213001, 2011.

[64] D. F. Shao, R. C. Xiao, W. J. Lu, H. Y. Lv, J. Y. Li, X. B. Zhu, and Y. P. Sun. Manipulating charge density waves in 1t-tsa2 by charge-carrier doping: A first-principles investigation. *Physical Review B*, 94:125126, Sep 2016.

[65] Z. Tao, F. Zhou, T.-R. T. Han, D. Torres, T. Wang, N. Sepulveda, K. Chang, M. Young, R. R. Lunt, and C.-Y. Ruan. The nature of photoinduced phase transition and metastable states in vanadium dioxide. *Sci. Rep.*, 6:38514, Dec 2016.

[66] Y. Tokura. Critical features of colossal magnetoresistive manganites. *Reports on Progress in Physics*, 69(3):797, 2006.

[67] M. van Veenendaal. Ultrafast photoinduced insulator-to-metal transitions in vanadium dioxide. *Physical Review B*, 87:235118, Jun 2013.

[68] E. Verwey. Electronic conduction of magnetite (fe 3 o 4) and its transition point at low temperatures. *Nature*, 144(3642):327, 1939.

[69] J. Vila, R. K. Pal, and M. Ruzzene. Observation of topological valley modes in an elastic hexagonal lattice. *Physical Review B*, 96(13):134307, 2017.

[70] A. Weiße and H. Fehske. Microscopic modelling of doped manganites. *New Journal of Physics*, 6(1):158, 2004.

[71] E. J. Woll and W. Kohn. Images of the fermi surface in phonon spectra of metals. *Phys. Rev.*, 126:1693–1697, Jun 1962.

[72] X. Xue, M. Jiang, G. Li, X. Lin, G. Ma, and P. Jin. Photoinduced insulator-metal phase transition and the metallic phase propagation in vo2 films investigated by time-resolved terahertz spectroscopy. *J. Appl. Phys.*, 114(19):193506, 2013.

[73] C. Zhang, W. Li, B. Gray, B. He, Y. Wang, F. Yang, X. Wang, J. Chakhalian, and M. Xiao. Ultrafast pump-probe spectroscopic signatures of superconducting and pseudogap phases in yba2cu3o7-d films. *J. Appl. Phys.*, 113(8):083901, 2013.

[74] J. Zhang and R. Averitt. Dynamics and control in complex transition metal oxides. *Annu. Rev. Mater. Res.*, 44:19–43, 2014.

[75] J. Zhang and R. Averitt. Dynamics and control in complex transition metal oxides. *Annual Review of Materials Research*, 44:19–43, 2014.

[76] L. Zhu, E. Prodan, and K. H. Ahn. Flat energy bands within antiphase and twin boundaries and at open edges in topological materials. *arXiv preprint arXiv:1807.10778*, 2018.

[77] L. Zhu, T. F. Seman, M. van Veenendaal, and K. H. Ahn. Photoinduced nonequilibrium dynamics in charge ordered materials. *Journal of Applied Physics*, 123(11):115112, 2018.